SÃO PAULO STATE UNIVERSITY – UNESP

Institute of Chemistry - Araraquara Campus

Aminu Habib Adamu

SYNTHESIS AND CHARACTERIZATION OF YTTRIUM IRON GARNET CRYSTALS IN PbO AND BaO BASED GLASS-CERAMICS: EFFECTS OF Y_2O_3 AND Fe_2O_3 DOPING ON MAGNETO-OPTICAL PROPERTIES

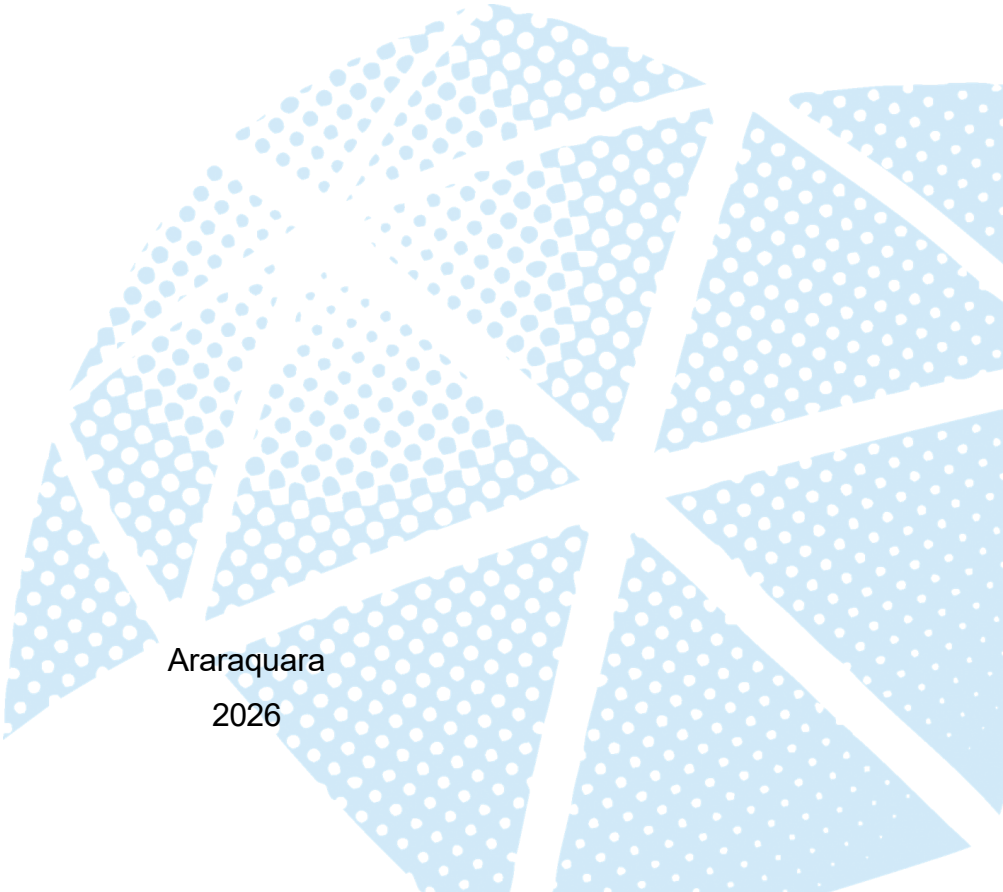

Araraquara

2026

Aminu Habib Adamu

Synthesis and Characterization of Yttrium Iron Garnet Crystals in PbO and BaO Based Glass-Ceramics: Effects of Y_2O_3 and Fe_2O_3 Doping on Magneto-Optical Properties

Thesis presented to the São Paulo State University (UNESP), Institute of Chemistry, Araraquara, to obtain a Master's in Chemistry.

Area of Concentration: Inorganic Chemistry

Supervisor: Prof. Dr. Marcelo Nalin

Co-supervisor: Prof. Dr. Douglas Faza Franco

Araraquara

2026

A221s

Adamu, Aminu Habib

Synthesis and characterization of yttrium iron garnet crystals in pbo and bao based glass-ceramics : effects of Y_2O_3 and Fe_2O_3 doping on magneto-optical properties / Aminu Habib Adamu. -- Araraquara, 2026

146 f. : il., tabs.

Dissertação (mestrado) - Universidade Estadual Paulista (UNESP), Instituto de Química, Araraquara

Orientador: Nalin Marcelo

1. Crystallization. 2. Glass-ceramics. 3. Magnetooptics. I. Título.

Sistema de geração automática de fichas catalográficas da Unesp. Dados fornecidos pelo autor(a).

Impacto Esperado na Sociedade

Este trabalho contribui para o ODS 9 (Indústria, Inovação e Infraestrutura) ao desenvolver novos materiais e rotas de processamento para tecnologias fotônicas avançadas. Também contribui para o ODS 12 (Consumo e Produção Responsáveis) ao explorar sistemas vítreos livres de chumbo (à base de BaO), reduzindo impactos ambientais e riscos à saúde associados ao uso de materiais contendo chumbo.

Expected Impact on Society

This work supports SDG 9 (Industry, Innovation and Infrastructure) by developing new materials and processing routes for advanced photonic technologies. It also contributes to SDG 12 (Responsible Consumption and Production) by exploring Pb-free (BaO-based) glass systems that reduce environmental and health concerns associated with lead-containing materials.

UNIVERSIDADE ESTADUAL PAULISTA

Câmpus de Araraquara

CERTIFICADO DE APROVAÇÃO

TÍTULO DA DISSERTAÇÃO: Synthesis and Characterization of Yttrium Iron Garnet Crystals in PbO- and BaO-Based Glass-Ceramics: Effects of Y_2O_3 and Fe_2O_3 Doping on Magneto-Optical Properties

AUTOR: AMINU HABIB ADAMU
ORIENTADOR: MARCELO NALIN

Aprovado como parte das exigências para obtenção do Título de Mestre em Química, pela Comissão Examinadora:

gov.br Documento assinado digitalmente
MARCELO NALIN
Data: 08/07/2026 16:32:54-0300
Verifique em https://validar.iti.gov.br

Prof. Dr. MARCELO NALIN (Participaçao Virtual)
Departamento de Química Analítica, Físico-Química e Inorgânica / UNESP / Câmpus de Araraquara - IQAr

gov.br Documento assinado digitalmente
RODRIGO FERNANDO COSTA MARQUES
Data: 12/07/2026 07:49:57-0300
Verifique em https://validar.iti.gov.br

Prof. Dr. RODRIGO FERNANDO COSTA MARQUES (Participaçao Virtual)
Assistência Técnica - PROPG / UNESP / Reitoria - RUNESP

gov.br Documento assinado digitalmente
YARA GALVAO GOBATO
Data: 08/07/2026 17:51:43-0300
Verifique em https://validar.iti.gov.br

Profa. Dra. YARA GALVÃO GOBATO (Participaçao Virtual)
Departamento de Física / Universidade Federal de São Carlos - UFSCar

Araraquara, 08 de julho de 2026.

CURRICULAR DATA

IDENTIFICATION	
Name	Aminu Habib Adamu
Date of Birth	05/08/1995
Nationality	NIGERIA
Passport No.	A12972482
Name in bibliographic citations:	A.A. Habib, Adamu A. Habib Aminu Habib
Business address	São Paulo State University (UNESP), Institute of Chemistry, Araraquara Campus Francisco Degni Street, 55 Araraquara – SP ZIP Code 14800-060 Telephone: (16)982147183
Lattes CV	http://lattes.cnpq.br/3577071370569136
ORCID	https://orcid.org/0009-0000-4588-4880
other identifier	https://www.linkedin.com/in/aahabib/
Email	Ah.adamu@unesp.br Aminu.theanalyst@gmail.com

ACADEMIC TRAINING	
	Master's in Chemistry UNESP, Institute of Chemistry, Araraquara Campus
	Português como Língua Estrangeira A1 Unesp, Faculdade de Ciências e Letras Campus de Araraquara

BIBLIOGRAPHICAL PRODUCTION

Nalin, Marcelo, Leonardo V. Albino, Thiago A. Lodi, Juliane R. Orives, Lia M. Marcondes, **Adamu A. Habib**, María Helena R. Acosta, Edgar D. Zanotto, and Douglas F. Franco. "Novel scalable synthesis of luminescent and magnetic single crystal garnets." Materials Horizons (2025). DOI: 10.1039/d5mh00254k

Works prepared and/or submitted to indexed journals:

1. **Systematic Replacement of PbO by BaO for TGG Single-crystal Production Using the Supersaturated Glass-Melt Method –** *under revision J. of Non-Cryst. Sol. 2026.*

2. **Novel Synthesis of $Y_3Fe_5O_{12}$ Single Crystals in Glass-ceramics for Enhanced Magneto-optical Applications**

PARTICIPATION IN BOARDS AND GUIDANCE

Leticia de Sá Cassimiro, Chemical Engineering Student – Undergraduate

Project Area:

Synthesis of monocrystals of grenades containing tb-eu-y for multifunctional sensors

Final workbenches

Not applicable.

Guidelines

ADAMU A. Habib, **SYNTHESIS AND CHARACTERIZATION OF YTTRIUM IRON GARNET CRYSTALS IN PbO AND BaO BASED GLASS-CERAMICS: EFFECTS OF Y_2O_3 AND FE_2O_3 DOPING ON MAGNETO-OPTICAL PROPERTIES**

PROF. DR. MARCELO NALIN. MASTER'S (CHEMISTRY) - SÃO PAULO STATE UNIVERSITY (UNESP), INSTITUTE OF CHEMISTRY, ARARAQUARA, SÃO PAULO, BRAZIL. 2026.

PARTICIPATION IN SCIENTIFIC EVENTS

Oral presentation at scientific events:

A. Adamu Habib, D. Faza Franco, L. Vieira Albino, T. Lodi, M. Nalin "Synthesis and Characterization of Yttrium Iron Garnet Crystals in PbO and BaO Based Glass-Ceramics: Effects of Y_2O_3 and Fe_2O_3 Doping on Magneto-Optical Properties" (B-MRS meeting 2025).

Marcelo Nalin, Eduardo Ghezzi, L. Vieira Albino, T. Lodi, **Adamu Habib**, Douglas Franco, "Microsized Rare-Earth Iron Garnets (REIG) Single Crystals Obtained by Glass Crystallization" International Conference on Glass (Glass Lyon 2026)

Poster presentation at scientific events:

T. Lodi, Eduardo Ghezzi, L. Vieira Albino, **Aminu Habib**, Marcelo Nalin, "Microsized Rare-Earth Iron Garnets (REIG) Single Crystals Obtained by Glass Crystallization" International Conference on Glass (Glass Lyon 2026)

A. Adamu Habib, D. Faza Franco, L. Vieira Albino, T. Lodi, M. Nalin "Systematic Replacement of PbO with BaO for TGG Production Using the Supersaturated Solution Methodology" (B-MRS meeting 2025)

Leticia de Sá Cassimiro, **Aminu Habib Adamu**, Marcelo Nalin "Synthesis and characterization of $Y_3Co_5O_{12}$ and $Y_3Mn_5O_{12}$ in glass ceramics for magneto-optic applications (MO)" 2025. (XXXVII Congresso de Iniciação Científica da UNESP).

Leonardo V. Albino, Thiago A. Lodi, **Aminu H. Adamu**, Juliane R. Orives, Fábio J. Caixeta, Douglas F. Franco, Maja Polańska, Agustín Delendatti, Ukshin Sylmetaj, Marcelo Nalin "Science and Art: Controlled Cooling of Molten Glass in the Synthesis of Luminescent and Magnetic Single Crystals Based on Rare Earth Garnets" (48ª Reunião da Sociedade Brasileira de Química (SBQ)), 2025.

A. Adamu Habib, D. Faza Franco, L. Vieira Albino, T. Lodi, M. Nalin "Synthesis and Characterization of Yttrium Iron Garnet Crystals in PbO and BaO Based Glass-Ceramics: Effects of Y_2O_3 and Fe_2O_3 Doping on Magneto-Optical Properties" (3rd Sao Carlos School of Glass and Glass-ceramic 2025)

Others:

Participated in the Workshop on **Advanced Solid-State NMR** – 2026 (28H Activity) in IQAR– UNESP with partnership IFSC University of São Paulo from March 9 – 13 2026, ARARAQUARA-SP, BRAZIL

Attended the **XXIII B-MRS Meeting**, in Salvador-BA, from September 28th to October 2nd, 2025 - Aminu Habib Adamu

Phase-ID and ***Structural Characterization of Materials*** using X-ray Powder Diffraction techniques short course (6 hours), in Salvador-BA, on September 28th, 2025 (B-MRS Meeting)

Participated in the event Innovation and Inspiration: Women in ***Quantum Physics*** held on 16/04 to 17/04 2025 in IQ-UNESP, Workload of 15 hours.

Attended the 2025 Compute Ontario Summer School course: ***Introduction to Artificial Neural Networks***. Workload of 18 hours.

Participated in the Webinar ***Introduction to the Theory of Colors***, held on July 30, 2025 with a total workload of 2 hours (Escola do Vidro da ABCERAM).

Award:

Bernhard Gross Student Awards 2025 - Symposium F – Oral – **Aminu Habib Adamu**. Synthesis and Characterization of Yttrium Iron Garnet Crystals in PbO and BaO Based Glass-Ceramics: Effects of Y_2O_3 and Fe_2O_3 Doping on Magneto-Optical Properties.

“I dedicate this work to my family. This thesis is a testament to their patience and support.”

ACKNOWLEDGMENTS

I would like to express my sincere gratitude to the Tertiary Education Trust Fund (TETFUND), Nigeria, for the scholarship that made this master's program possible. This support was essential for the successful completion of this work.

I am deeply grateful to my supervisor, Prof. Dr. Marcelo Nalin, for his guidance, patience, and continuous encouragement throughout this research. His scientific insight and critical approach greatly shaped this work and contributed to my academic development. I also sincerely thank my co-supervisor, Prof. Dr. Douglas Faza Franco, for his support, valuable discussions, and contributions to this study.

I would also like to acknowledge the São Paulo Research Foundation (FAPESP) for its support of the research project. In addition, I thank CAPES for supporting my participation in the B-MRS Meeting (SBPMat 2025) in Salvador, Bahia.

My appreciation goes to the postdoctoral researchers Dr. Leonardo Vieira Albino and Dr. Thiago Augusto Lodi, as well as the Ph.D. student Eduardo Oliveira Ghezi, for their technical assistance, helpful discussions, and willingness to share their knowledge. Their support was important at different stages of this work.

I am also grateful to Prof. Javier A. Ellena from the São Carlos Institute of Physics (IFSC), University of São Paulo (USP), São Carlos, SP, Brazil, for performing the single-crystal X-ray diffraction measurements. I also sincerely acknowledge Prof. Jorlândio F. Felix from the Institute of Physics, Applied Physics Center, University of Brasília, Brasília, DF, Brazil, for carrying out the SQUID magnetic measurements at the Laboratory of Nanomaterials Synthesis and Magnetic Characterization (LSNCM).

I would also like to acknowledge the Photonic research group, which provided the broader scientific environment for this work, as well as the LAViE Group, where the research activities related to glass materials and glass-ceramics were mainly developed.

I am also grateful to Sergio Luis Scarpari for his technical support and training on the use of equipment such as Raman spectroscopy, optical microscopy, UV–Vis, and FTIR.

Finally, I would like to thank my family for their constant support, patience, and encouragement. Their understanding and sacrifices gave me the strength to complete this journey.

"To whom much is given,
much is expected."

Abstract

This study presents a glass-ceramic route for synthesizing yttrium iron garnet ($Y_3Fe_5O_{12}$, YIG) single crystals in PbO- and BaO-based systems, with the aim of improving magneto-optical properties for photonic applications. In contrast to conventional crystal growth techniques such as the Czochralski and liquid-phase epitaxy methods, this approach relies on controlled cooling of the melt to promote nucleation and growth of crystals directly within the glass matrix. As a result, YIG single crystals with sizes in the range of 5–50 μm are formed and uniformly distributed in the glass-ceramic. The effect of composition was examined by varying the concentrations of Y_2O_3 and Fe_2O_3 in both glass systems. This allowed evaluation of how chemical composition influences crystallization behavior, microstructure, and magnetic properties. Structural and morphological characterization using X-ray diffraction (XRD), Raman spectroscopy, and scanning electron microscopy with energy-dispersive spectroscopy (SEM-EDS) confirmed the formation of YIG with a well-defined cubic structure. Magnetic measurements showed the expected ferrimagnetic behavior associated with YIG. The results indicate that the BaO-based system provides better phase purity, with fewer secondary phases compared to the PbO-based system. This suggests that BaO offers a more stable chemical environment for YIG crystallization. The method developed in this work provides a simple and scalable way to produce YIG crystals within glass-ceramics, with potential use in magneto-optical devices such as Faraday rotators, optical isolators, and fiber-based photonic components operating near 1.55 μm.

Keywords: Controlled crystallization, Glass-ceramic, Magneto-optical, Photonic devices, $Y_3Fe_5O_{12}$ single-crystals

Resumo

Este trabalho apresenta uma rota vitrocerâmica para a síntese de monocristais de granada de ítrio e ferro ($Y_3Fe_5O_{12}$, YIG) em sistemas à base de PbO e BaO, com o objetivo de otimizar as propriedades magneto-ópticas (MO) para aplicações fotônicas. Em contraste com técnicas convencionais de crescimento fases crsitalinas c, como os métodos Czochralski e de epitaxia em fase líquida, esta abordagem baseia-se no resfriamento controlado do fundido para promover a nucleação e o crescimento de cristais diretamente na matriz vítrea. Como resultado, formam-se monocristais de YIG com tamanhos na faixa de 5–50 μm, distribuídos de forma uniforme na vitrocerâmica. O efeito da composição foi investigado por meio da variação das concentrações de Y_2O_3 e Fe_2O_3 em ambos os sistemas vítreos. Isso permitiu avaliar como a composição química influencia o comportamento do processo de cristalização, e nas propriedades magnéticas. As caracterizações estruturais e morfológicas, realizadas por difração de raios X (DRX), espectroscopia Raman e microscopia eletrônica de varredura acoplada à espectroscopia de energia dispersiva (MEV-EDS) confirmaram a formação de YIG com estrutura cúbica bem definida. As medidas magnéticas evidenciaram o comportamento ferrimagnético já esperado para o YIG. Os resultados indicam que o sistema à base de BaO apresenta maior pureza de fase, com menor formação de fases secundárias em comparação ao sistema à base de PbO. Isso sugere que o BaO fornece um ambiente químico energeticamente mais estável para a cristalização do YIG. O método desenvolvido neste trabalho oferece uma forma simples e escalável de produzir cristais de YIG em matrizes vitrocerâmicas, com potencial aplicação em dispositivos MO, como rotadores de Faraday, isoladores ópticos e componentes fotônicos integrados em fibras operando na faixa de 1,55 μm.

Palavras-chave: Cristalização controlada, Vitrocerâmica, Materiais Magneto-ópticos, Dispositivos fotônicos, Monocristais de $Y_3Fe_5O_{12}$

LIST OF FIGURES

LIST OF FIGURES IN APPENDIX

LIST OF TABLES

List of Equations

LIST OF ABBREVIATIONS AND ACRONYMS

BaO	Barium oxide
Bi:YIG	Bismuth-substituted yttrium iron garnet
Bi_2O_3	Bismuth oxide
CLNGG	Calcium lithium niobium gallium garnet
CVT	Chemical vapor transport
CZ	Czochralski method
DSC	Differential scanning calorimetry
EDS	Energy-dispersive spectroscopy
EXAFS	Extended X-ray absorption fine structure
Fe_2O_3	Iron(III) oxide
FZ	Floating-zone method
Ga_2O_3	Gallium oxide
GeO_2	Germanium dioxide
HMO	Heavy metal oxide
Ia3d	Cubic space group notation
MO	Magneto-optical
PbO	Lead oxide
RE	Rare-earth element
SEM	Scanning electron microscopy
SQUID	Superconducting quantum interference device
TGG	Terbium gallium garnet
UV-Vis	Ultraviolet–visible spectroscopy
XANES	X-ray absorption near edge structure
XRD	X-ray diffraction
Y_2O_3	Yttrium oxide
Yb-YGG	Ytterbium yttrium gallium garnet
$YFeO_3$	Yttrium orthoferrite
YIG	Yttrium iron garnet ($Y_3Fe_5O_{12}$)

Table of Contents

CHAPTER 1 – INTRODUCTION

1.2 STATE OF THE ART

1.2.1 Magneto-Optical Garnet Materials

Magneto-optical (MO) materials have gained increasing recognition because of their crucial role in modern technological applications, particularly in Faraday isolators, mid-infrared lasers, magneto-optical sensors, photonic devices, and biomedical imaging [2-3]. These materials enable the interaction between light and magnetic fields, which forms the basis of many optical technologies. One of the most important magneto-optical effects is the Faraday effect. In this phenomenon, the polarization plane of linearly polarized light rotates when a material is placed in a magnetic field [4]. The magnitude of this rotation is commonly described by the Verdet constant, which serves as a measure of the efficiency of a material for magneto-optical applications. Consequently, materials that exhibit large Verdet constants together with high optical transparency are highly desirable for devices such as optical isolators, modulators, current sensors, and components used in optical communication systems.

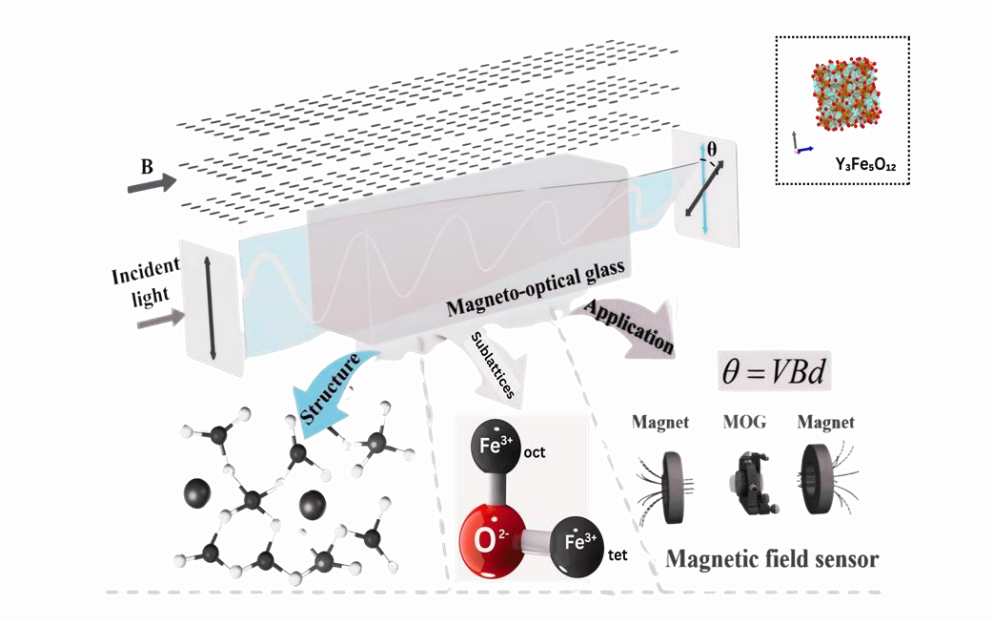

Graphical Abstract 1. *Faraday Effect and the impact of YIG associated with MO application. The diagram is adapted from the article [1]*

Among the different classes of magneto-optical materials, ferrimagnetic garnets are widely recognized for their excellent magnetic and optical properties. Garnets belong to a group of oxide ceramics that generally follow the formula $R_3Fe_5O_{12}$, where R is a rare-earth element such as yttrium, terbium, or gadolinium. These materials crystallize in a cubic structure and contain several distinct cation sites within the crystal lattice. This structural arrangement allows different ions to occupy specific positions in the lattice, making garnets highly adaptable materials whose physical properties can be modified through chemical substitution or doping [5].

Yttrium iron garnet (YIG), with the formula $Y_3Fe_5O_{12}$, is widely studied for its strong magnetic and magneto-optical properties [4]. YIG forms a cubic garnet structure in the Ia3d space group [4]. In this structure, yttrium ions are found in dodecahedral sites, and iron ions are split between octahedral and tetrahedral sites, all coordinated by oxygen ions [4,5], as shown in the figure 2 below.

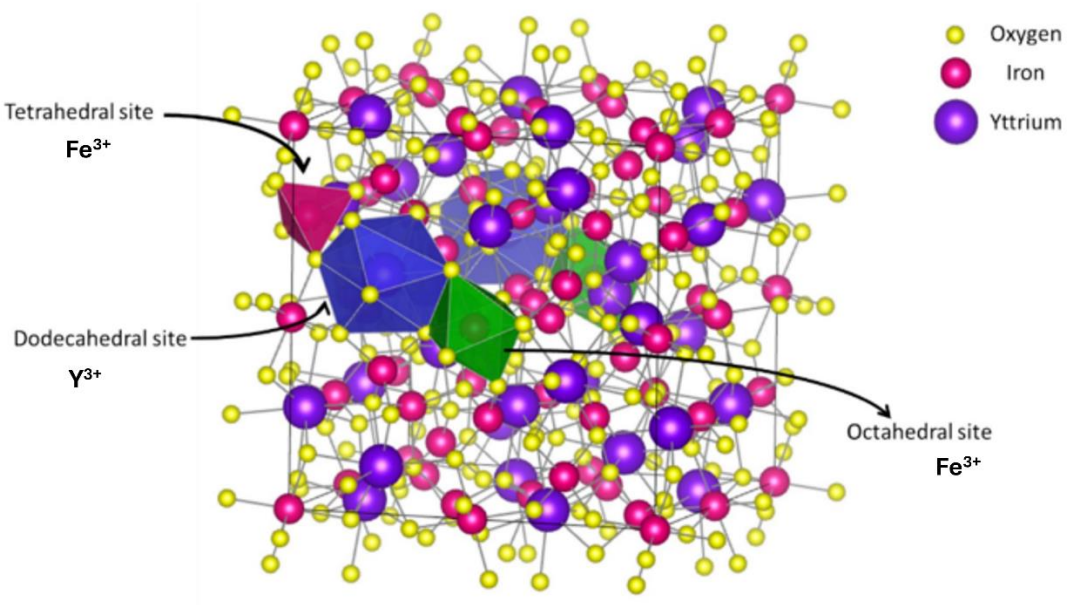

Figure 2. Crystal structure of yttrium iron garnet ($Y_3Fe_5O_{12}$) with cubic space group *Ia3d*. Adapted from [4].

The magnetic properties of YIG result from the antiparallel alignment of magnetic moments between iron ions situated in octahedral and tetrahedral sites, which generates a net ferrimagnetic magnetization within the crystal [6].

The synthesis of high-quality yttrium iron garnet ($Y_3Fe_5O_{12}$) requires strict control of chemical composition and processing conditions to avoid the formation of secondary phases. YIG is thermodynamically stable within a narrow compositional range corresponding approximately to a 3:5 yttrium-to-iron ratio in the Y_2O_3–Fe_2O_3 system, typically at temperatures above about 1200 °C [4]. Deviations from this ideal stoichiometry, such as oxygen deficiencies or non-stoichiometric precursor mixtures, may result in the formation of competing phases including yttrium orthoferrite ($YFeO_3$) or spinel-type compounds such as YFe_2O_4 [4]. These parasitic phases can disturb the long-range magnetic ordering and introduce scattering centers that degrade magnetic and spin-transport properties [4]. The stability region of YIG within the Y–Fe–O system is illustrated in Fig. 3

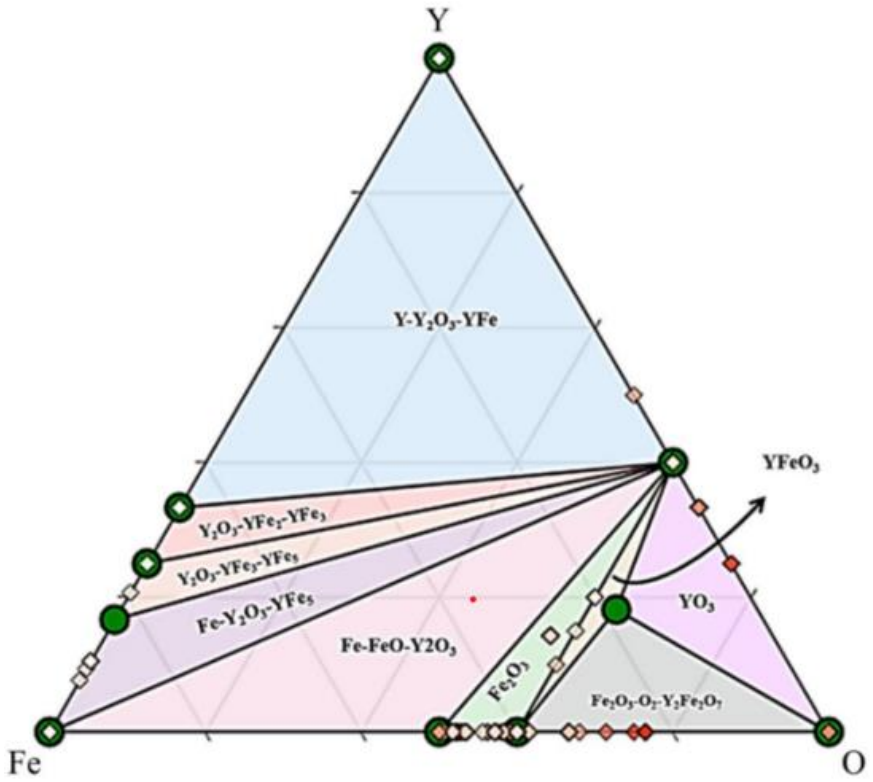

Figure 3. Phase diagram of the Y–Fe–O system illustrating the phase relationships between yttrium and iron oxides relevant to YIG formation. Adapted from [4]

YIG has several key properties that make it useful for magneto-optical and microwave technologies. It features low magnetic damping, high electrical resistivity, low dielectric loss, and strong spin-wave propagation [7]. Thanks to these qualities, YIG is commonly used in microwave filters, oscillators, phase shifters, and magnetic sensors [4,7,8]. The material also

exhibits stable magnetic behavior and a relatively high Curie temperature [9,10], enabling it to maintain magnetic order across a wide range of operating conditions [10].

In optical applications, YIG is particularly attractive because it combines magnetic ordering with high optical transparency in the visible and near-infrared regions [4]. These features allow the material to show strong Faraday rotation, which is needed for magneto-optical devices like optical isolators and magneto-optical modulators [9]. Optical isolators based on garnet crystals are widely used in laser systems and fiber-optic communication networks to prevent reflected light from damaging sensitive optical components [11].

Although pure YIG already possesses useful magneto-optical properties, further improvements can be achieved by introducing substitutional ions into the garnet lattice. Various dopants can replace yttrium or iron ions in the structure, thereby modifying magnetic anisotropy, magnetization, and optical response. For example, rare-earth ions such as terbium or dysprosium can enhance magneto-optical activity [12]. Elements such as gallium or aluminum can alter magnetic interactions within the lattice [13]. Through such substitutions, the magneto-optical behavior of garnets can be tuned to meet specific technological requirements [5].

A well-known example is bismuth-substituted yttrium iron garnet (Bi:YIG), which has attracted significant attention because the incorporation of bismuth ions strongly enhances Faraday rotation. Bi:YIG thin films have been widely studied for magneto-optical imaging and sensing applications because they can provide high Faraday rotation values while maintaining good optical transparency in the near infrared region [2].

In addition to YIG, other garnet crystals such as terbium gallium garnet (TGG) are also widely used in magneto-optical devices. TGG crystals possess a high Verdet constant and good thermal stability, making them suitable for high-power laser systems and optical isolators [11]. Compared with many other garnets, YIG offers a unique balance between magnetic performance, optical transparency, and structural stability, which explains why it remains one of the most widely investigated magneto-optical materials [14].

Magneto-optical garnets, particularly yttrium iron garnet and its substituted variants, continue to play a key role in the development of advanced optical and magnetic technologies. Ongoing research focuses on improving their synthesis, enhancing their magneto-optical response, and integrating them into modern photonic systems such as optical communication devices and magnetically controlled optical components.

1.2.2 Glass-Ceramics as Hosts for Functional Crystals

Glass-ceramics are materials produced by the controlled crystallization of precursor glasses [15–16]. These materials integrate the properties of both glasses and crystalline ceramics, resulting in enhanced mechanical, optical, and thermal performance. The development of glass-ceramics originated from the realization that specific heat-treatment processes can induce nucleation and growth of crystalline phases within a glass matrix while preserving the original shape. This method enables the creation of materials that retain the transparency and processability of glass, as well as the structural order and functional properties of crystals [17], as illustrated in Fig. 4.

Unlike conventional glasses, which are amorphous and lack long-range structural order, glass-ceramics contain finely dispersed crystalline phases within a residual glassy matrix [18]. Their microstructure is typically achieved through a two-step heat-treatment process consisting of nucleation and subsequent crystal growth. Precise control over the parent glass composition and thermal treatment conditions enables tailoring of the size, distribution, and volume fraction of the crystalline phases [17–19]. These factors significantly affect the physical properties of the material, such as optical transparency, magnetic response, and mechanical strength.

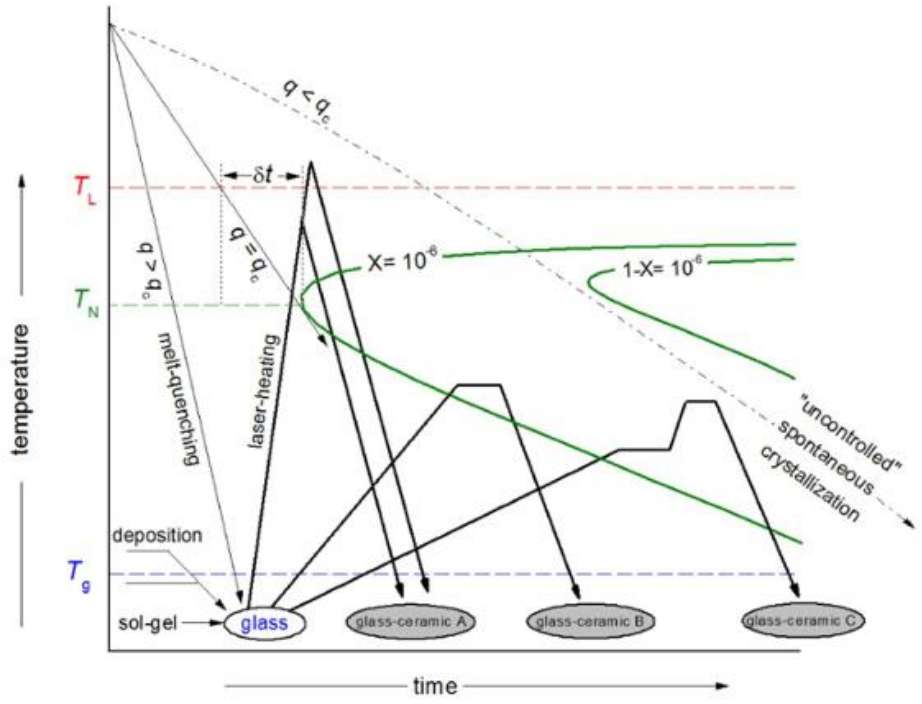

Figure 4. Processes of glass conversion into Glass-ceramic. Adapted from [11]

A key advantage of glass-ceramics is their ability to serve as host matrices for functional crystals. The synthesis of large single crystals of many materials with notable optical or magnetic properties is often hindered by complex growth conditions, extended processing durations, or elevated production costs [20]. In glass-ceramics, however, these functional crystals can be generated directly inside the glass matrix through controlled crystallization. This approach allows the formation of micro- or nanometer-sized crystals with relatively uniform distribution throughout the material. Consequently, glass-ceramics provide a versatile platform for incorporating active phases such as luminescent, magnetic, or magneto-optical crystals [17].

Transparent glass-ceramics are highly desirable for photonic applications. If the crystallites formed during heat treatment are significantly smaller than the wavelength of visible light, the material remains optically transparent even in the presence of crystalline phases. Under such conditions, light scattering is minimized, and the optical behavior of the glass-ceramic may approach that of a single crystal [21]. This property enables the fabrication of optical materials that combine the functional performance of crystals with the manufacturing flexibility of glasses.

Glass-ceramics have therefore become an important class of materials in photonics and optical engineering. Various optical devices, including optical amplifiers, phosphors, and laser host materials, have been developed using glass-ceramic systems [22,23]. Rare-earth ions are frequently incorporated into these materials because they possess well-defined electronic transitions that generate luminescence or magneto-optical effects. When these ions are incorporated into crystalline phases formed within the glass matrix, their spectroscopic properties can be significantly enhanced due to the ordered crystal environment surrounding the active ions.

Another advantage of glass-ceramics is the wide range of compositions that can be explored. Different glass systems, including silicate, borate, germanate, and heavy-metal oxide glasses, can be designed to produce specific crystalline phases after heat treatment. The flexibility in glass composition allows researchers to engineer materials with tailored optical, magnetic, or luminescent properties [17–19]. In particular, heavy-metal oxide glass systems have attracted significant interest because they typically exhibit high refractive indices, good infrared transparency, and relatively low phonon energies, making them suitable hosts for photonic crystals and rare-earth dopants [24].

Glass-ceramics incorporating garnet-type crystals have attracted significant research interest in recent years because of their advantageous optical and magneto-optical

properties. Garnet structures, such as yttrium ytterbium gallium garnet (Yb-YGG), terbium gallium garnet (TGG), and rare-earth gallium garnets, have been synthesized within glass matrices through controlled crystallization [17, 19, 22]. These crystalline phases are known for their chemical stability, mechanical strength, and optical performance. In addition, garnet crystals can incorporate a wide variety of rare-earth ions, enabling tunable optical emission and magneto-optical behavior.

Despite these advantages, preparing glass-ceramics suitable for optical applications requires careful control of the crystallization process. If the crystals grow too large or become unevenly distributed, strong light scattering may occur, reducing transparency. Therefore, understanding the nucleation mechanisms, crystallization kinetics, and phase evolution during heat treatment is important for designing glass-ceramic materials with optimized optical performance [25].

Taken together, glass-ceramics provide a platform for hosting functional crystalline phases and for tailoring optical and magnetic properties through controlled crystallization. Their combination of glass processability and crystalline functionality supports their use in optical and photonic technologies. Further work on composition design, nucleation control, and crystallization behavior remains relevant for improving material performance.

1.2.3 Crystallization of Garnet Phases in Glass-Ceramic Systems

Forming crystalline phases within glass is important for producing glass-ceramic materials with useful optical and magnetic properties. In such systems, crystallization occurs when a parent glass undergoes controlled nucleation and crystal growth during cooling or through subsequent heat treatment [17]. This process allows specific crystalline phases to precipitate within the amorphous matrix while maintaining the glass structure [26]. Understanding the mechanisms of nucleation and growth is therefore essential for designing glass-ceramics with tailored microstructures and functional properties, as illustrated in Fig. 5.

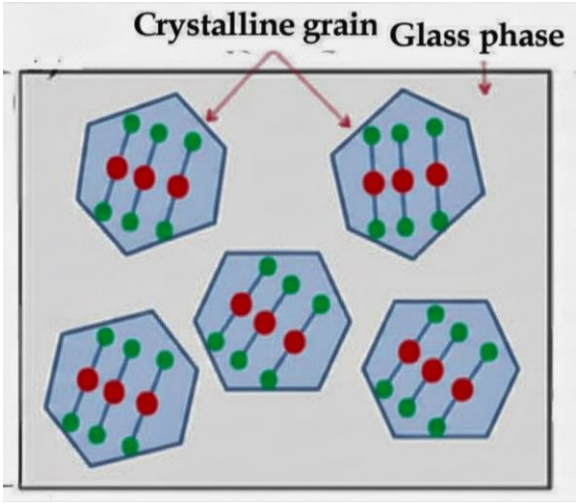

Figure 5. diagram showing the structure of glass-ceramic, which combines crystalline and amorphous phases. Adapted from [27]

One way to produce glass-ceramics is to melt a mixture of oxide precursors, then rapidly cool it to form an amorphous glass. Subsequent thermal treatment above the glass transition temperature promotes nucleation and growth of crystalline phases within the glassy structure. The crystallization process is strongly influenced by factors such as chemical composition, cooling rate, and the presence of nucleating agents [28], in some cases. These parameters control the size, distribution, and morphology of the crystals formed within the glass, thereby determining the optical and magnetic properties of the resulting material [17, 19, 29].

Recent research shows that garnet-type crystals can form inside glass through controlled crystallization processes through the cooling process [18–25]. Garnets with the formula $RE_3B_5O_{12}$, where RE is a rare-earth element and B can be Al, Ga, or Fe, are especially valued for their optical clarity, chemical stability, and magneto-optical properties. These features make them useful in photonics, lasers, scintillators, and magneto-optical devices [26].

Studies have shown that garnet crystals can be grown directly in heavy-metal oxide glass matrices [17, 18, 24, 26]. Here, the liquid glass acts as a medium for crystal nucleation and growth during controlled cooling. For instance, rare-earth gallium garnets have been made by cooling glass mixtures rich in rare-earth oxides. As the glass cools, it moves out of equilibrium, which helps crystals form and grow to micrometer sizes within the glass matrix [24].

Experiments show that crystallization can produce cubic garnet crystals ranging from a few micrometers to several tens of micrometers, depending on the method used. Glass-ceramics can produce evenly distributed crystals while retaining some of the glassy matrix. Thus, chemical treatments can dissolve the glass phase, letting researchers extract single crystals for further study [17].

Many types of garnet have been crystallized in glass-ceramic systems. Still, unwanted secondary phases, uneven crystal sizes, and challenges in controlling the number of crystals formed can affect the material's final properties. So, it is important to carefully manage the glass composition and heat treatment to obtain glass-ceramics with uniform crystal distribution and optimal performance [19].

These studies show that controlling nucleation and crystal growth is key to getting garnet phases with clear cubic structures and the best functional properties.

1.2.4 Heavy Metal Oxide Glasses: PbO vs BaO Based Systems

Glasses are thermodynamically unstable materials that spontaneously evolve toward the metastable equilibrium state of the supercooled liquid (SCL) through structural relaxation [25], as illustrated in Fig. 6.

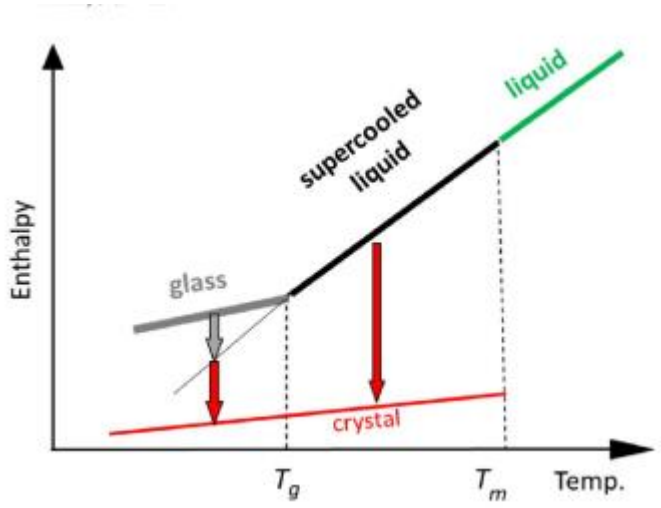

Figure 6. Enthalpy–temperature diagram of a glass-forming system, illustrating four states: liquid (L), supercooled liquid (SCL), glass (G), and crystalline phase (C). Here, $T_m$represents the melting (liquidus) temperature, while $T_g$corresponds to the glass transition temperature. Adapted from [25]

The VT/enthalpy diagram in Fig. 6 shows the thermodynamic and kinetic evolution of a glass-forming system during cooling. Above the melting temperature (Tm), the material exists as a liquid with high atomic mobility. Upon cooling, if crystallization is suppressed, the melt enters the supercooled liquid region, where atomic disorder persists but viscosity increases. As structural relaxation slows and atomic rearrangement becomes insufficient, the system passes through the glass transition temperature (Tg) and forms a glassy state [25]. Glass formation is primarily governed by kinetic factors, notably the cooling rate and the inhibition of crystal nucleation and growth [25]. In glass-ceramic processing, controlled heat treatment above Tg can induce nucleation and crystal growth within the glass matrix, enabling the development of crystalline phases such as TGG [19]. This interplay between vitrification and crystallization is essential for understanding the synthesis route employed in this study.

Heavy metal oxide (HMO) glasses are widely studied for photonic, magneto-optical, and radiation-shielding applications because they are dense, have high refractive indices, and exhibit strong optical polarizability [31]. These glasses typically contain significant amounts of oxides such as PbO, Bi_2O_3, BaO, TeO_2, or GeO_2 [21], which enhance their optical and electronic properties compared to conventional silicate or borate glasses [31]. HMO glasses generally exhibit weaker metal–oxygen bonds, higher atomic masses, and nonlinear optical responses [29–31].

Lead oxide (PbO)-based glass is one of the most extensively studied HMO systems. PbO can play different roles in glass networks depending on the composition [32, 33]. Its addition typically increases density and refractive index while reducing glass transition temperature and viscosity, which facilitates processing [18]. Due to the high atomic number of lead, PbO-containing glasses interact strongly with electromagnetic radiation and show enhanced optical properties, including higher polarizability and improved infrared transparency [24]. These characteristics make PbO-based glasses suitable for optical lenses, shielding windows, and photonic devices [34].

Another advantage of PbO-containing glasses is their ability to accommodate high concentrations of heavy-metal oxides or rare-earth ions without significantly affecting the glass formation process [24]. [18–21]. This makes them suitable hosts for functional crystals and dopants used in photonic and magneto-optical materials. Increasing PbO content also enhances density and photon attenuation through photoelectric absorption and scattering [35].

However, PbO-containing glasses present some limitations. Lead compounds are toxic and raise environmental and health concerns during processing and disposal [36]. In addition, high lead content can reduce mechanical durability in some systems. These limitations have motivated the search for alternative glass systems with comparable optical properties and improved environmental compatibility [37].

Barium oxide (BaO)-containing glasses are considered a promising alternative. BaO mainly acts as a network modifier, contributing to improved chemical durability and structural stability. The addition of BaO generally enhances mechanical strength, hardness, and resistance to thermal and chemical degradation. BaO-containing glasses also exhibit good optical transparency and thermal stability, making them suitable for photonic applications [37].

BaO can partially replace PbO while retaining key properties such as optical transparency and relatively high density. Studies indicate that BaO-containing glasses, particularly when combined with other heavy oxides such as Bi_2O_3 or GeO_2, can exhibit optical and radiation-shielding performance comparable to PbO-based systems [26]. Substituting PbO with BaO therefore provides a route toward reducing environmental impact while maintaining functional performance.

Heavy metal oxide glass systems often involve multiple oxides to tailor structural and functional properties. Combinations of PbO, BaO, Bi_2O_3, and GeO_2 allow adjustment of density, refractive index, and crystallization behavior. This compositional flexibility is especially relevant for glass-ceramic systems, where controlled crystallization enables the formation of functional crystalline phases within the glass matrix. In photonic applications, such systems can support the formation of rare-earth-containing crystals or garnet phases.
To sum up, PbO-based glasses exhibit high density, strong optical polarizability, and good glass-forming ability [38], whereas BaO-based glasses offer improved chemical stability and reduced environmental concerns. Understanding the differences between these systems is important for designing glass-ceramics with tailored optical and magneto-optical properties.

1.3 Research Gap and Motivation

Although significant progress has been made in the development of magneto-optical garnet materials and glass-ceramic systems, several scientific and technological challenges remain. Conventional synthesis methods for yttrium iron garnet (YIG), such as solid-state reactions, Czochralski crystal growth, and liquid-phase epitaxy, typically require high processing temperatures, long growth durations, and strict control of crystallization conditions. These techniques often involve complex equipment and are not easily scalable for large-scale production of functional magneto-optical materials [6, 10, 39].

Glass-ceramic processing has emerged as a promising alternative route for producing functional crystalline phases within glass matrices through controlled nucleation and crystallization. This approach offers several advantages, including lower processing temperatures, compositional flexibility, and the ability to control crystal size and distribution within the glass matrix. Previous studies have demonstrated the successful crystallization of various garnet phases, such as yttrium ytterbium gallium garnet (Yb-YGG), Terbium gallium garnet (TGG) and rare-earth gallium garnets, in glass-ceramic systems [17,19,24]. However, the controlled formation of yttrium iron garnet (YIG) crystals directly within heavy metal oxide glass matrices remains relatively unexplored, particularly in compositions containing PbO or BaO as major network modifiers.

Heavy-metal oxide glasses containing PbO, BaO, Bi_2O_3, and GeO_2 exhibit high refractive indices, good infrared transparency, and strong solubility for rare-earth ions, making them attractive hosts for photonic and magneto-optical materials [19]. Nevertheless, the influence of glass composition on the crystallization behavior, microstructure, and magneto-optical properties of YIG-containing glass-ceramics is still not well understood. In particular, comparative investigations between PbO-based and BaO-based glass systems remain limited, despite their potential to significantly affect nucleation kinetics, crystal growth, and optical performance.

Therefore, this research investigates the synthesis of YIG crystals within heavy metal oxide glass-ceramics based on $PbO–Bi_2O_3–GeO_2$ and $BaO–Bi_2O_3–GeO_2$ systems. By controlling the composition and thermal processing conditions, this study aims to understand the crystallization mechanisms and microstructural evolution of YIG phases, as well as their resulting magneto-optical properties. Ultimately, this work contributes to the development of

new glass-ceramic materials with potential applications in magneto-optical devices and optical communication technologies operating at 1.55 μm telecom wavelength.

1.4 Strategy and Development of the Research Work

The research strategy adopted in this work was designed to enable the synthesis of yttrium iron garnet ($Y_3Fe_5O_{12}$, YIG) single crystals at the micrometer scale within glass-ceramic matrices. A survey of the available literature indicates that the controlled formation of micrometer-scale YIG single crystals embedded in glass-ceramics has not yet been reported, which positions the present study as an original contribution.

As an initial step, Pb-free terbium gallium garnet ($Tb_3Ga_5O_{12}$, TGG) was selected as a model system. This choice was motivated by previous successful synthesis of TGG in our research group using a $PbO–Bi_2O_3–GeO_2–Ga_2O_3–Tb_4O_7$ glass system [19], as well as the availability of commercial TGG single crystals used as reference materials. In parallel, environmental and regulatory considerations were taken into account, since the use of lead is restricted under the European RoHS directive except in cases where no viable alternatives exist. Consequently, a new Pb-free glass composition was developed by completely replacing PbO with BaO, resulting in the $BaO–Bi_2O_3–GeO_2–Ga_2O_3–Tb_4O_7$ system.

Building on this result, two additional glass systems were designed for YIG crystallization: a fully Pb-free composition ($BaO–Bi_2O_3–GeO_2–Fe_2O_3–Y_2O_3$) and a mixed Pb/Ba system ($PbO–BaO–Bi_2O_3–GeO_2–Fe_2O_3–Y_2O_3$). These compositions were successfully used to obtain phase-pure YIG single crystals. To the best of our knowledge, none of these three glass systems has been previously cited in the literature. Following the establishment of the chemical architectures, appropriate structural, magnetic, and magneto-optical characterization techniques were selected and applied.

Among the investigated systems, the $BaO–Bi_2O_3–GeO_2–Ga_2O_3–Tb_4O_7$ and $BaO–Bi_2O_3–GeO_2–Fe_2O_3–Y_2O_3$ compositions stand out as particularly promising.

1.5 Aim and Objectives of the Study

1.4.1 Aim

To synthesize yttrium iron garnet ($Y_3Fe_5O_{12}$, YIG) single crystals within PbO-, BaO-, and mixed Pb/Ba-based heavy metal oxide glass-ceramics, and to investigate the influence of Y_2O_3 and Fe_2O_3 concentrations on crystallization behavior, phase formation, microstructure, and magnetic properties, with implications for magneto-optical applications.

1.4.2 Objectives

1. To design and synthesize multicomponent PbO-, BaO-, and Pb/Ba-based heavy metal oxide glass-ceramics doped with Y_2O_3 and Fe_2O_3 for the formation of YIG single crystals.

2. To investigate phase formation, crystal structure, and microstructural evolution of the glass-ceramics, with emphasis on controlling nucleation, growth, and distribution of YIG crystals.

3. To evaluate the influence of glass composition (PbO vs BaO) on crystallization behavior, phase purity, and the formation of secondary phases.

4. To perform comprehensive structural, thermal, optical, and magnetic characterization using DSC, XRD (powder and single-crystal), Raman spectroscopy, SEM-EDS, UV–Vis–NIR spectroscopy, and SQUID magnetometry.

5. To assess the suitability of the synthesized materials for magneto-optical and photonic applications, including their potential integration into optical fiber systems.

1.6.1 Single-Crystal Synthesis Techniques

Single-crystal growth is a cornerstone of fundamental and applied research on garnet-type materials, as many of their key magnetic, optical, and magneto-optical properties are strongly anisotropic and highly sensitive to crystallographic defects. Over the past decades, a wide range of crystal growth techniques has been developed to produce top-quality single crystals of garnets with compositions of the general formula $A_3B_5O_{12}$, where $\boldsymbol{A}$ and $\boldsymbol{B}$ are typically rare-earth and transition-metal ions, respectively. The choice of a suitable growth method is primarily dictated by the thermodynamic and kinetic characteristics of the target garnet, including its melting behavior (congruent or incongruent), phase stability, volatility of constituents, and reactivity with crucible materials, as well as practical considerations such as achievable crystal size and defect control [40-41]

Garnet crystals are usually grown from the melt, from high-temperature solutions using flux growth, or less often from the vapor phase. Melt-based methods like the Czochralski, Bridgman–Stockbarger, and floating-zone techniques work especially well for garnets that melt evenly or can be kept stable near their melting points. This includes many garnets with aluminum, gallium, or iron. These techniques enable the synthesis of large-volume crystals with good structural morphology, which is essential for device-oriented applications such as solid-state lasers, microwave components, and magneto-optical isolators [40, 42]. However, they typically require high processing temperatures, controlled atmospheres, and sophisticated instrumentation.

The methods used to synthesize garnet single crystals are described below:

1.6.1.1 Flux Method (Solution growth)

The flux method, or solution growth, involves crystallizing a solid phase from a high-temperature supersaturated solution during controlled cooling, as shown in fig 7. In this technique, the garnet-forming oxides are dissolved in an appropriate solvent (flux) with a relatively low melting point, allowing crystal growth at temperatures well below the melting point of the target compound. As the temperature is gradually reduced, the solution becomes supersaturated, leading to nucleation and growth of single crystals [43].

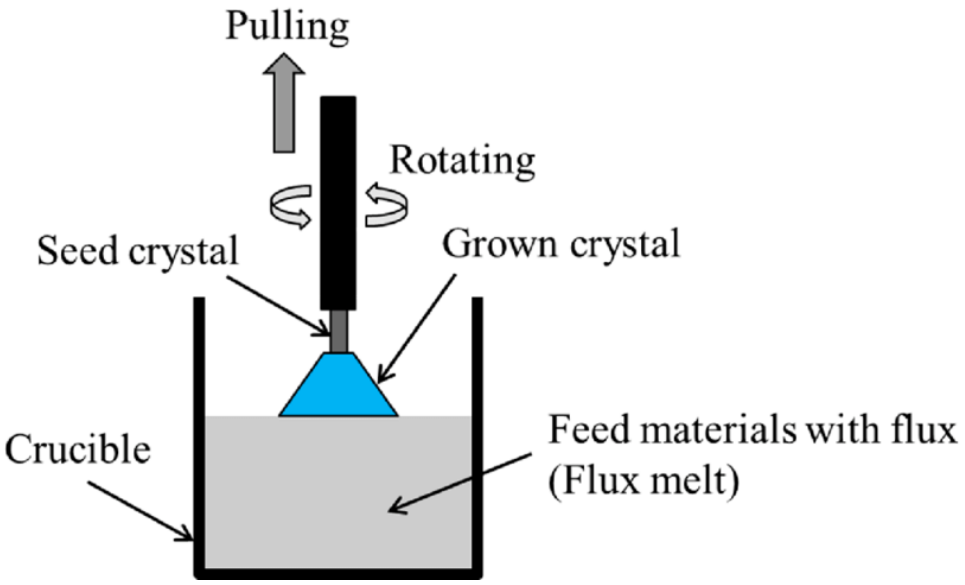

Figure 7. Schematic illustration of the top-seeded flux solution growth method. Adapted from [44].

The possibility of flux is governed by phase diagram considerations, solubility behavior, chemical compatibility, and volatility. For garnet-type materials, PbO-based fluxes, often modified with PbF_2 or B_2O_3, have historically been the most effective solvents, particularly for incongruently melting iron garnets such as $Y_3Fe_5O_{12}$ and rare-earth substituted variants. The flux expands the crystallization window, suppresses premature nucleation, and promotes the formation of well-faceted, high-quality crystals [45].

Growth is typically performed in platinum crucibles, followed by slow cooling according to a predefined thermal profile derived from partial phase equilibria. After growth, residual flux is removed by centrifugation or chemical etching [46].

A critical limitation of the flux method is the incomplete knowledge of phase diagrams for complex multicomponent garnet systems, which necessitates empirical optimization of composition and cooling schedules. Additionally, flux inclusions, solvent incorporation, and

limited crystal size are persistent challenges. Nevertheless, compared to melt-growth techniques, flux growth offers major advantages, including low thermal stress, high structural perfection, and the unique capability to grow incongruently melting garnets. As a result, flux growth remains one of the most important methods for producing high-quality garnet single crystals for fundamental studies and magneto-optical applications [43, 47].

1.6.1.2 Bridgman method

The Bridgman method, originally developed by Percy W. Bridgman, is a classical melt-growth technique widely used for the synthesis of oxide single crystals, including numerous garnet family members. It is based on the controlled solidification of a molten charge through a well-defined temperature gradient, typically established within a multi-zone furnace, illustrated in fig 8. In this method, crystallization is initiated at the cold end of the crucible and proceeds unidirectionally as the melt is slowly translated from the high-temperature zone to the lower-temperature part of the furnace [48].

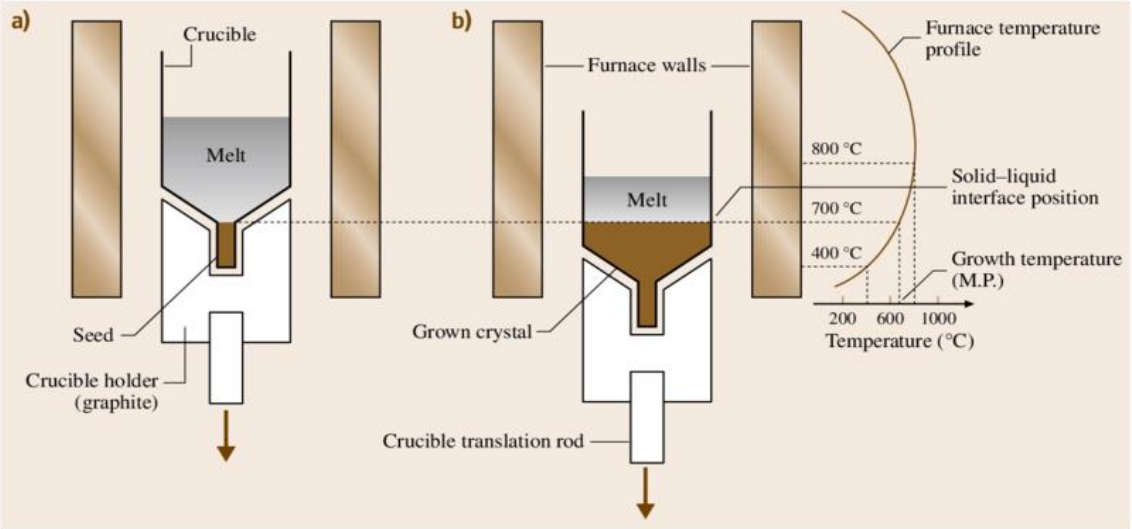

Figure 8. Schematic of vertical Bridgman directional solidification showing crucible, melt, and growing crystal under a furnace temperature gradient. Adapted from [48].

For garnet crystal growth, the Bridgman method commonly employs crucibles with a conically shaped bottom or a narrow capillary tail. This geometric feature plays a critical role in promoting single-grain selection during the initial stages of solidification. Nucleation preferentially occurs within the confined conical region, where competitive growth

suppresses secondary grains, allowing a single crystallographic domain to propagate through the entire melt volume [48].

Depending on the furnace configuration, the process may be implemented in either vertical or horizontal arrangements, with the vertical Bridgman configuration being more widely adopted for oxide garnets due to improved control over thermal gradients and melt convection.

The experimental setup of the Bridgman technique typically consists of a high-purity crucible (often platinum or iridium for oxide garnets), a precisely controlled furnace capable of generating stable axial temperature gradients, and a mechanical translation system that governs the lowering or raising rate of the crucible. Crystal quality is strongly influenced by growth parameters such as temperature gradient, translation speed, and atmosphere composition, which must be carefully optimized to minimize thermal stress, constitutional supercooling, and defect formation [48].

In the context of garnet materials, the Bridgman method has been successfully employed for both congruently melting and flux-assisted growth systems. Congruent garnets such as calcium lithium niobium gallium garnet (CLNGG) and related multicomponent garnets have been grown directly from the melt, yielding transparent crystals with good structural uniformity and optical quality [48].

For incongruently melting garnets, particularly rare-earth iron garnets ($R_3Fe_5O_{12}$), modified approaches such as the flux-Bridgman method have been developed. In this hybrid technique, a suitable flux lowers the effective crystallization temperature while retaining the directional solidification advantages of the Bridgman process, enabling the synthesis of large-volume, pure magneto-optical garnet crystals [49].

Compared to other melt-growth techniques, the Bridgman method offers several advantages for garnet synthesis, including relatively simple instrumentation, good scalability, and effective grain selection. However, challenges such as compositional segregation, thermal cracking, and crucible–melt interactions remain critical issues, particularly for complex, multicomponent garnets. Despite these limitations, the Bridgman and flux-Bridgman techniques continue to play a significant function in the growth of garnet single crystals for optical, laser, scintillation, and magneto-optical applications [49].

1.6.1.3 Czochralski method

The Czochralski (CZ) method, developed by Polish chemist Jan Czochralski in 1915, is a well-known technique for growing large, good-quality single crystals, as shown in fig 9. In this process, a solid crystal is pulled vertically from its melt, which is kept just above its melting point. Growth starts when a narrow seed rod is dipped into the molten material, and surface tension at the solid–liquid interface causes the material to stick to the seed [50].

As the crystal grows, the seed is slowly pulled up and rotated, usually in the opposite direction to the crucible rotation. The speed of pulling and rotation are important and depend on the material's properties, like viscosity, melting point, and thermal conductivity. Using a single-crystal seed with a predetermined orientation ensures that the new crystal maintains the same structure, which is important for garnet materials used in optical and magneto-optical devices [39].

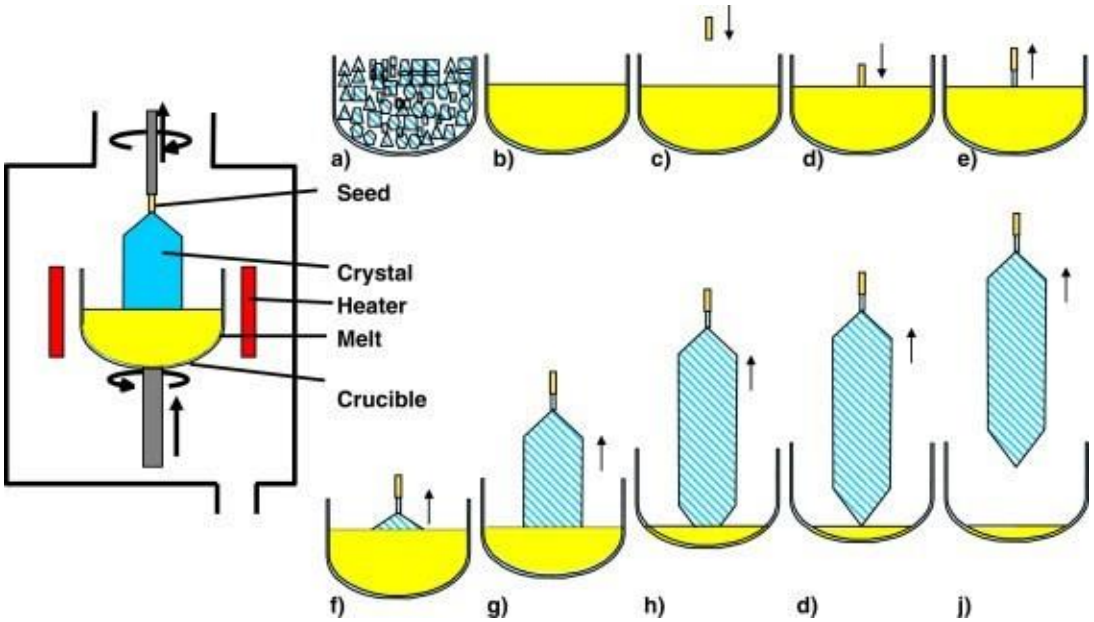

Figure 9. Illustration of the Czochralski method, depicting the instrument set-up. The process includes a) elements in the crucible, b) melted elements, c) and d) connecting the precursor to the melt, and e) to j) pulling the crystal out. Adapted from [51].

Unlike the Bridgman method, the Czochralski technique does not confine the solid–liquid interface with crucible walls. This leads to less mechanical disturbance while the crystal forms. This feature contributes to improved structural perfection and makes the CZ method particularly suitable for growing large-diameter garnet single crystals, such as yttrium aluminum garnet, gadolinium gallium garnet, and terbium gallium garnet. Growth is typically

carried out in iridium crucibles under controlled atmospheres to suppress oxide evaporation and crucible degradation [14].

Compared to other melt-growth techniques, the Czochralski method offers significant advantages, including precise control of crystal diameter, excellent scalability, and industrial maturity. However, challenges remain, particularly for gallium-containing garnets, where Ga_2O_3 volatilization can lead to compositional fluctuations, growth striations, and defect formation. Despite these limitations, the CZ method remains the dominant technique for producing large garnet single crystals for laser, microwave, and magneto-optical devices [50].

1.6.1.4 Floating-Zone method

The floating-zone (FZ) method is a crucible-free melt-growth technique originally developed for high-purity crystal synthesis and later adapted for complex oxide materials, including garnet-type compounds. In this method, as illustrated in fig 10, a localized molten zone is created between an upper polycrystalline feed rod and a lower seed crystal. The molten zone is maintained by focused thermal radiation and is held in place by surface tension, eliminating the need for a container. Crystal growth occurs as the molten zone is translated along the feed rod, while the solidified material crystallizes epitaxially onto the seed [52].

For garnet crystals, the floating-zone process is typically performed in an optical-mirror furnace equipped with high-power halogen, xenon, or laser heat sources. Radiation from these sources is focused onto a narrow region, enabling the formation of a stable molten zone at temperatures exceeding 1500 °C. Counter-rotating the feed and seed rods is often used to improve melt uniformity and reduce thermal and compositional changes at the solid–liquid interface, thereby lowering defects [53].

Recent advances include laser-heated and hybrid laser floating-zone systems, which provide sharper thermal gradients, higher attainable temperatures, and improved energy efficiency compared to conventional lamp-based furnaces. These developments have enabled the growth of incongruently melting garnets, such as terbium aluminum garnet and rare-earth iron garnets, which are difficult to obtain using conventional melt-growth techniques [54].

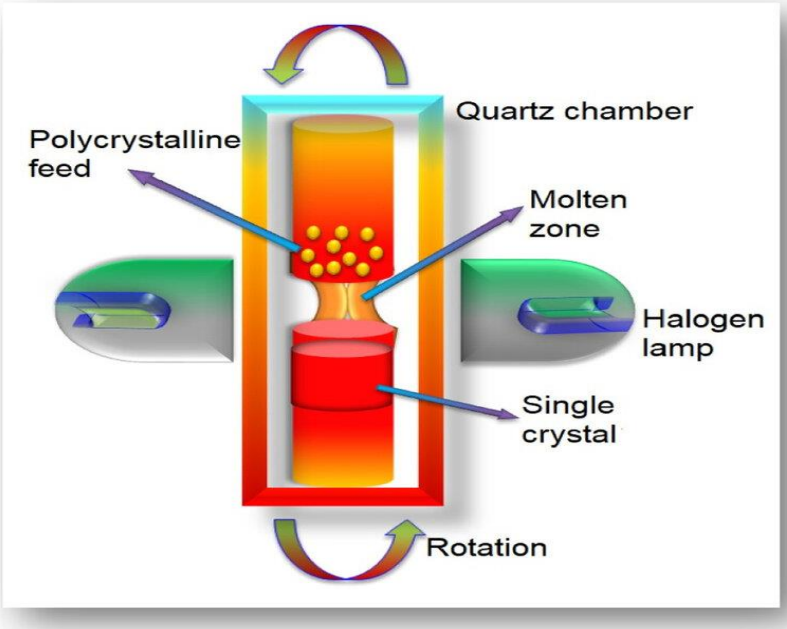

Figure 10. Illustration of the floating-zone single crystal growth process with hot zone, molten region, and solidification front. Adapted from [55].

Compared to crucible-based methods such as Czochralski and Bridgman growth, the floating-zone technique offers significant advantages, including the absence of crucible contamination, improved chemical purity, and precise control of growth atmosphere. However, limitations remain, particularly the difficulty of stabilizing the molten zone for multicomponent or volatile systems, restrictions on achievable crystal diameter, and sensitivity to compositional segregation. Despite these challenges, the floating-zone method remains a powerful approach for growing high-quality garnet single crystals for optical, laser, and magneto-optical applications [52, 53, 54, 56].

1.6.1.5 Chemical vapor transport method

The chemical vapor transport (CVT) method is a way to grow crystals using gases. It works by moving solid materials as volatile chemicals under a set temperature difference. To do this, the source material and a small amount of transport agent are sealed in a vacuumed quartz tube, which is placed in a two-zone furnace. The temperature difference between the hot source zone and the cooler growth zone causes the process to happen. At the hot end, the solid reacts with the transport agent to make volatile compounds, as shown in fig 11. These compounds travel through the gas and break down at the cooler end, where the solid

crystals form [57].

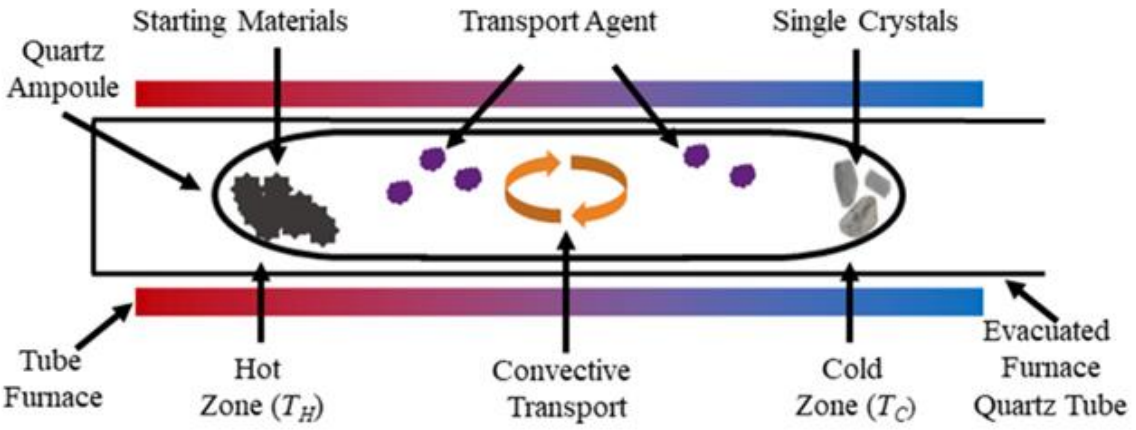

Figure 11. Schematic diagram of the chemical vapor transport (CVT) method, showing source zone, transport agent gas phase, and crystal deposition zone. Adapted from [58].

In complex oxide garnets, halogens and halogen-containing compounds such as Cl_2, $FeCl_3$, YCl_3, and CCl_4 are commonly used as transport agents because they can form volatile metal halides at elevated temperatures. The efficiency and direction of transport are governed by thermodynamic parameters, particularly the Gibbs free energy and enthalpy of the transport reaction, as well as the magnitude of the imposed temperature gradient [57].

Careful selection of the transport agent is essential to achieve congruent transport and suppress parasitic phase formation. For example, $Y_3Fe_5O_{12}$ single crystals have been successfully grown using CCl_4 and $FeCl_3$, yielding well-faceted garnet crystals without secondary iron oxide phases under optimized conditions.

Compared to melt-growth techniques, the CVT method offers several advantages, including relatively low growth temperatures, high chemical purity, and excellent crystal morphology. It is particularly valuable for garnets that decompose incongruently or suffer from volatilization during melt processing. However, crystal sizes obtained by CVT are typically limited to a few millimeters, and growth rates are slow. In addition, precise thermodynamic control is required to avoid incongruent transport and compositional deviations. Despite these limitations, CVT remains an important complementary technique for fundamental studies and high-quality garnet single crystals where melt growth is impractical.

1.6.2 Supersaturated Glass-Melt Method

The supersaturated glass-melt method has recently emerged as an alternative approach for producing single-crystal garnets directly from glass compositions, as illustrated by the diagram in fig 12. Unlike conventional crystal growth techniques, which typically rely on directional solidification or seed-assisted growth, this method uses a glass-forming composition as a reaction medium in which crystal nucleation and growth occur during the cooling of the melt. In this approach, a multicomponent heavy-metal oxide glass containing the desired cations is melted at high temperature and subsequently cooled under controlled conditions, leading to the precipitation of crystalline garnet phases within the glass matrix [26].

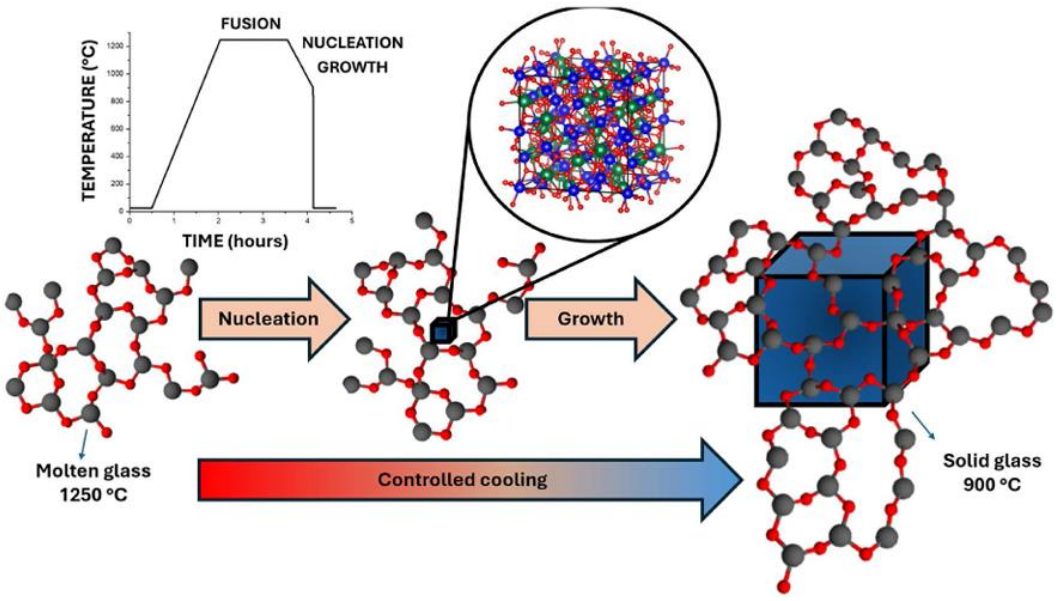

Figure 12. Diagram highlighting the procedure for growing garnet single-crystals by the Supersaturated Glass-Melt Method (also called controlled cooling). Adapted from [17]

In general, the process begins with the preparation of a parent glass composed of heavy metal oxides such as PbO, Bi_2O_3, GeO_2, and Ga_2O_3 together with rare-earth oxides. The melt is typically heated above 1200 °C to achieve complete homogenization. During controlled cooling, the supersaturated melt enters a non-equilibrium state that favors the nucleation of crystalline phases. As the viscosity of the supercooled liquid increases, nuclei form and grow into micrometer-sized single crystals embedded within the residual glass

matrix. The remaining glass phase can subsequently be removed by chemical etching, allowing the isolated crystals to be collected and characterized.

Recent studies by different researchers have demonstrated the feasibility of this approach for synthesizing several garnet compositions. For example, Souza *et al.* produced heavy-metal-oxide glass-ceramics containing rare-earth gallium garnet crystals ($Yb_3Ga_5O_{12}$) through controlled cooling of supersaturated glass melts, obtaining cubic crystals with sizes ranging from a few micrometers to over 100 μm [24].

Similarly, Albino *et al.* synthesized Er^{3+}/Tm^{3+}-doped ytterbium yttrium gallium garnet (Yb-YGG) single crystals using a gradual cooling process from molten PbO–GeO_2–Bi_2O_3–Ga_2O_3-based glasses, demonstrating that controlled nucleation and growth within the glass matrix can produce micrometric single crystals suitable for photonic applications [17].

More recently, Nalin *et al.* reported that this strategy can be extended to different garnet families, including $RE_3Ga_5O_{12}$, $RE_3Al_5O_{12}$, and $RE_3Fe_5O_{12}$, by adjusting the rare-earth composition and cooling parameters of the melt. Their work demonstrated that cubic single crystals can precipitate reproducibly from supersaturated heavy-metal oxide glass melts, forming almost monodispersed crystals distributed within the glass matrix [26].

Despite these promising results, several challenges remain associated with this technique. Controlling the nucleation density and crystal growth is essential to avoid the formation of unwanted secondary phases or polycrystalline aggregates. Additionally, the multicomponent nature of heavy-metal oxide glasses may lead to the precipitation of competing crystalline phases, which can affect the purity and uniformity of the desired garnet crystals. Careful control of glass composition, cooling rate, and rare-earth concentration is therefore required to obtain homogeneous crystals with well-defined morphology and functional properties.

Overall, the supersaturated glass-melt method provides a scalable and versatile route for synthesizing micrometric garnet single crystals within glass matrices. While this approach has been successfully applied to several gallium- and aluminum-based garnets, its application to the synthesis of yttrium iron garnet (YIG) from heavy-metal oxide glass systems remains largely unexplored, motivating further investigation.

1.7 Fundamentals of Magnetism

Magnetism in solids arises from the magnetic moments generated by the motion and spin of electrons, as well as their interactions within a crystal structure. The type of magnetism a material shows, like diamagnetism, paramagnetism, ferromagnetism, antiferromagnetism, or ferrimagnetism, depends on its electronic structure and how its atoms or ions interact. In oxide garnets, magnetism arises mainly from the localized magnetic moments of transition-metal and rare-earth ions, which interact via exchange mechanisms involving oxygen ions. Knowing these basic ideas about magnetism helps us understand the magnetic and magneto-optical properties of garnet materials.

1.7.1 Magnetic Moments and Magnetic Susceptibility

The magnetic moment **μ** of an atom or ion comes from both the orbital angular momentum **L** and the spin angular momentum **S** of its electrons. In quantum mechanics, the magnetic moment linked to the total angular momentum is given by

$$\mu = -g\mu_B J \quad [62] \qquad \text{(Eq. 1)}$$

here $\boldsymbol{\mu_B}$ is the **Bohr magneton**, $\boldsymbol{g}$ represent the **Landé g-factor**, and ***J*** is the total angular momentum quantum number, which is given by

$$\mathbf{J} = \mathbf{L} + \mathbf{S} \qquad \text{(Eq. 2)}$$

In solids, the overall magnetic response is called magnetization. It is defined as the magnetic moment per unit volume [59].

$$M = \mu \frac{N}{V} \qquad \text{(Eq. 3)}$$

where $\boldsymbol{V}$ is the volume of the material and $\boldsymbol{\mu}$ represents the magnetic moment of the atom or ion.

When an external magnetic field $\mathbf{H}$ is applied, the resulting magnetization depends on the magnetic nature of the material. In **linear magnetic materials**, the magnetization is directly proportional to the applied magnetic field and can be written as:

$$M = \chi H \qquad \text{(Eq. 4)}$$

where χ is the **magnetic susceptibility**, a dimensionless parameter that characterizes how strongly a material becomes magnetized in response to an external magnetic field.

The magnetic induction $\boldsymbol{B}$ is related to the magnetic field $\boldsymbol{H}$ and the magnetization $\boldsymbol{M}$ through;

$$B = \mu_0(H + M) \qquad \text{(Eq. 5)}$$

Substituting the relation $M = \chi H$ gives;

$$B = \mu_0(1 + \chi)H \qquad \text{(Eq. 6)}$$

Or

$$B = \mu_0\mu_r H \qquad \text{(Eq. 7)}$$

with $\boldsymbol{\mu_0}$ is the **permeability of free space** and $\mu_r = 1 + \chi$ the relative magnetic permeability of the material [60].

The sign and magnitude of χ determine the magnetic classification of a material and provide the basis for understanding the diverse magnetic behaviors observed in garnet systems, which are discussed in the following subsections:

1.7.2 Diamagnetism

Diamagnetism is a basic magnetic property found in all materials and comes from the way electrons move in their orbits. In diamagnetic substances, all the electron shells are filled or paired, so there is no permanent magnetic moment when there is no external magnetic field. When a magnetic field is applied, electron currents are set up in the material, following Lenz's law, and these currents create a magnetic moment that goes against the direction of the applied field, as shown in Fig. 13. As a result, diamagnetic materials have a small negative magnetic susceptibility ($\chi < 0$) and a relative permeability just below 1.

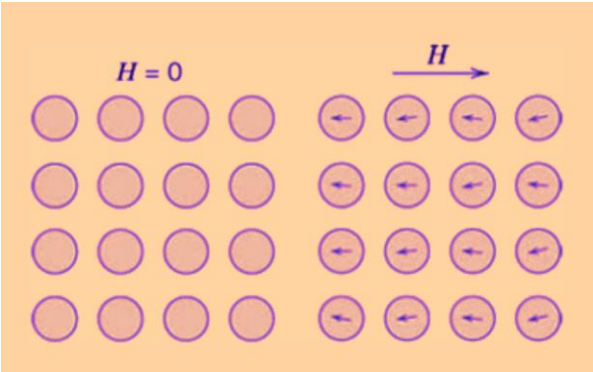

Figure 13. Magnetization behavior of diamagnetic materials showing negative magnetic susceptibility (Adapted from [61]).

The diamagnetic response is weak and generally temperature independent, as it does not involve spin alignment or cooperative interactions between magnetic moments. Although present in all materials, diamagnetism is usually masked by stronger magnetic effects such as paramagnetism or ferro- and ferrimagnetism. Typical diamagnetic materials include noble gases, closed-shell ions, and many oxides with fully paired electronic configurations.

1.7.3 Paramagnetism

As shown in fig. 14, paramagnetism occurs in materials containing atoms or ions with unpaired electrons, giving rise to permanent magnetic moments at the atomic scale. In the absence of an external magnetic field, these moments are randomly oriented due to thermal agitation, resulting in zero net magnetization. Upon application of a magnetic field, partial alignment of the moments occurs in the field direction, producing a weak positive magnetization and a small positive magnetic susceptibility ($\chi > 0$).

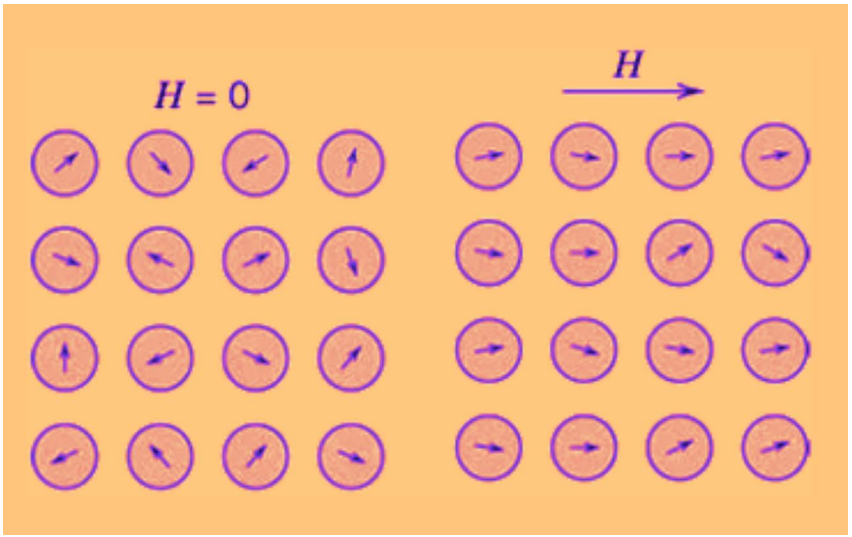

Figure 14. Magnetization response of paramagnetic materials with low magnetic

susceptibility (Adapted from [61]).

The magnetic response of paramagnetic materials is highly temperature-dependent. As temperature increases, thermal agitation disrupts moment alignment, reducing susceptibility. This behavior is described by Curie's law,

$$\chi = C/T \qquad \text{(Eq. 8)}$$

or more generally by the Curie–Weiss law when weak magnetic interactions are present. Paramagnetism is often observed in transition-metal and rare-earth ions with partially filled d or f orbitals. These ions play an important role in magneto-optical materials.

1.7.4 Antiferromagnetism

In antiferromagnetic materials, neighboring magnetic moments align antiparallel due to exchange interactions, resulting in the complete cancellation of magnetization in the ideal ordered state. This is illustrated in Fig. 15, below. Unlike ferromagnets, antiferromagnets exhibit no net spontaneous magnetization despite strong magnetic ordering at the atomic level.

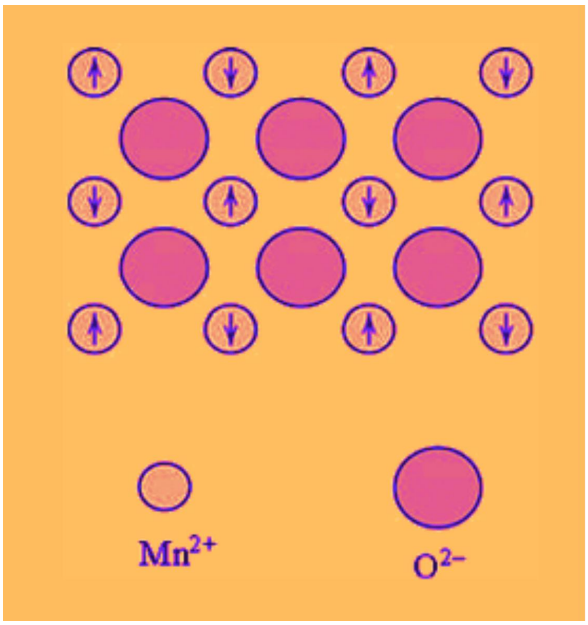

Figure 15. Antiferromagnetic ordering in MnO, where spins align in opposite directions, and there is no net magnetization when no magnetic field is applied. (Adapted from [61]).

This type of magnetic order is present when the temperature is below the Néel temperature (T_N). When the temperature rises above T_N, thermal energy becomes strong enough to overcome the exchange interaction, rendering the material paramagnetic.

Antiferromagnetism is commonly observed in transition-metal oxides, where superexchange interactions mediated by oxygen ions favor antiparallel spin alignment, as in MnO and related compounds.

1.7.5 Ferromagnetism

Ferromagnetism occurs when atomic magnetic moments align spontaneously, but only below a temperature called the Curie temperature (T_C). This collective ordering is driven by strong quantum-mechanical exchange interactions, which favor parallel spin alignment between neighboring atoms, as demonstrated in fig. 16. As a result, ferromagnetic materials exhibit large magnetization, high susceptibility, and the ability to retain magnetization even after the external field is removed.

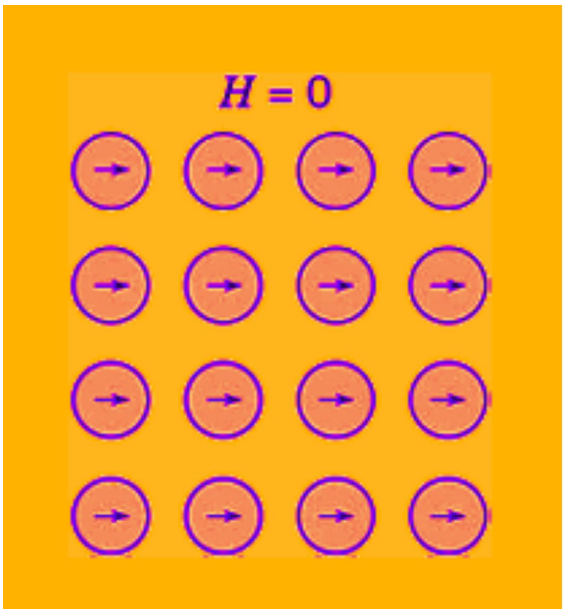

Figure 16. Magnetization behavior of ferromagnetic materials characterized by high susceptibility (Adapted from [61]).

Ferromagnetic materials consist of magnetic domains, regions of uniform magnetization separated by domain walls. Magnetization occurs through the movement of these domain walls and the rotation of magnetic moments. The response to an applied field is nonlinear and exhibits magnetic hysteresis, a hallmark of ferromagnetism. Classic examples include metallic iron, cobalt, and nickel.

The Curie temperatures of selected ferromagnetic and ferrimagnetic materials, as well as Néel temperatures of antiferromagnetic materials, are summarized in Table 1. For example, iron (Fe) has a Curie temperature of approximately 1043 K, indicating that it retains

ferromagnetic ordering well above room temperature, whereas materials with lower transition temperatures lose their magnetic ordering more easily.

Table 1. Summary of Curie temperatures (Tc) associated with ferro- and ferrimagnetic materials, along with Néel temperatures (TN) for antiferromagnetic systems. Adapted from [59].

Material	T_C $[K]$	T_N $[K]$
Fe	1043	
Co	1388	
Ni	627	
Gd	293	
Dy	88	
EuO	69	
Fe_3O_4	853	
CrO_2	387	
Cr		311
CoO		293
NiO		525

1.7.6 Ferrimagnetism

As shown in fig 17, ferrimagnetism occurs in compounds with multiple magnetic sublattices that are coupled antiparallel but possess unequal magnetic moments. As a result, the opposing sublattice magnetizations do not cancel completely, giving rise to a net spontaneous magnetization. This magnetic behavior is intermediate between ferromagnetism and antiferromagnetism and is typical of complex oxide materials such as ferrites and garnets.

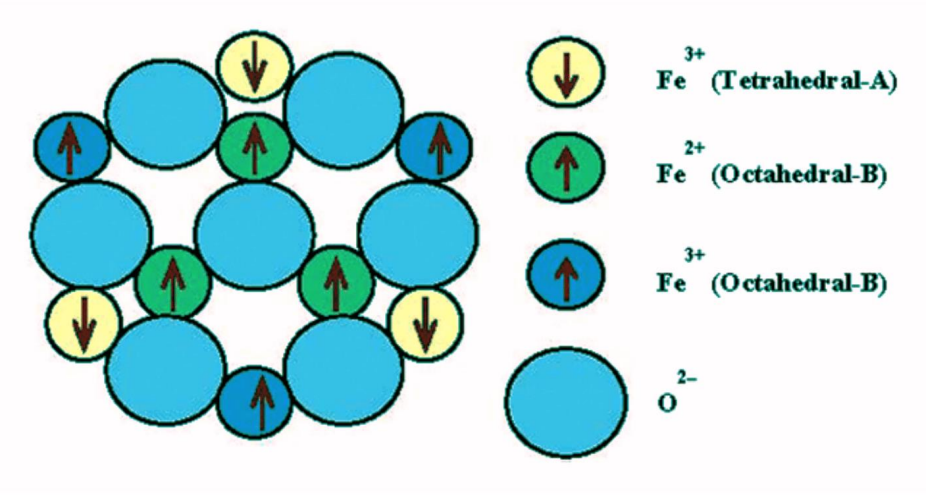

Figure 17. Ferrimagnetic ordering in Fe_3O_4 resulting in nonzero net magnetization (Adapted

from [61]).

In ferrimagnetic oxides, magnetic ions occupy crystallographically distinct sites with different coordination environments, leading to unequal magnetic contributions. Exchange interactions, often governed by superexchange, govern the antiparallel coupling between sublattices. Like ferromagnets, ferrimagnets exhibit magnetic domains, hysteresis, and a Curie temperature. Some ferrimagnetic systems exhibit a compensation temperature at which the net magnetization drops to zero, as the sublattice magnetizations change with temperature. This behavior is particularly relevant in rare-earth iron garnets used in magneto-optical applications.

1.7.7 Magnetic Hysteresis and Domain Theory

Magnetic hysteresis occurs when a magnetic material responds irreversibly to an applied magnetic field, as evidenced by a lag between magnetization and the field during repeated magnetization cycles. In ordered magnetic systems, this effect arises from the energy required to form magnetic domains and the resistance encountered by domain walls during motion due to microstructural defects, magneto-crystalline anisotropy, and exchange interactions. The resulting hysteresis loop, shown in Fig. 18, provides important magnetic parameters such as saturation magnetization, remanent magnetization, coercive field, and hysteresis loss. These values are important for understanding how ferrimagnetic garnets perform in microwave and magneto-optical applications [63].

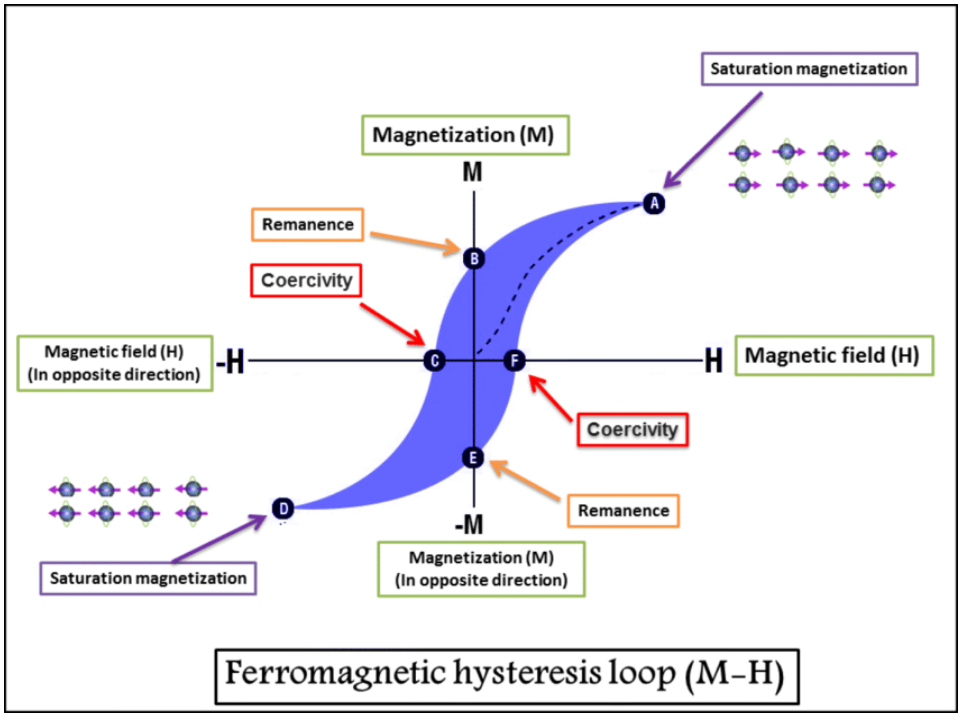

Figure 18. Typical magnetic hysteresis loop showing saturation magnetization M_s, remanent magnetization M_r, and coercive field H_c. Adapted from [7]

According to domain theory, a ferromagnetic or ferrimagnetic crystal minimizes its magnetostatic energy by subdividing into magnetic domains separated by domain walls, as illustrated in Fig. 19. Magnetization processes occur initially through reversible domain wall bulging at low fields, followed by irreversible domain wall displacement and rotation of magnetic moments at higher fields.

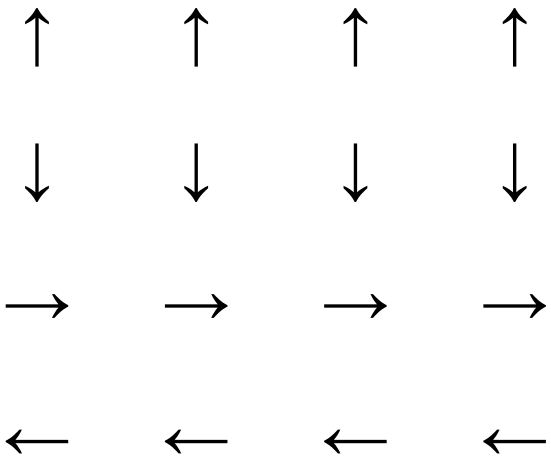

Figure 19. Schematic illustration depicting magnetic domains and domain walls within a ferromagnetic material. (Author ownership).

Hysteresis arises primarily from the pinning of domain walls at defects such as grain boundaries, pores, dislocations, and compositional inhomogeneities. The Jiles–Atherton model describes this behavior phenomenologically by introducing an anhysteretic magnetization curve and a pinning parameter that quantifies energy dissipation during irreversible wall motion [64–65].

In ferrimagnetic garnets such as yttrium iron garnet ($Y_3Fe_5O_{12}$) and terbium iron garnet ($Tb_3Fe_5O_{12}$), hysteresis behavior reflects the interaction between multiple antiparallel magnetic sublattices [66]. In YIG, magnetization arises from the incomplete cancellation of Fe^{3+} moments occupying octahedral and tetrahedral sites, resulting in soft ferrimagnetic behavior characterized by low coercivity and narrow hysteresis loops [64]. This makes YIG particularly suitable for low-loss microwave and magneto-optical devices [63].

The hysteresis properties of garnets are highly sensitive to microstructure. Studies on polycrystalline YIG show that increasing grain size reduces coercivity due to enhanced domain wall mobility, while improved crystallinity leads to higher saturation magnetization. Conversely, fine grains and secondary phases increase domain wall pinning, broaden hysteresis loops, and increase losses [63].

In magneto-optical garnets, hysteresis behavior is not only a magnetic signature but also influences Faraday rotation, optical loss, and device stability. Understanding magnetic hysteresis through domain theory therefore links crystal chemistry, microstructure, and functional performance in garnet-based glass-ceramic and single-crystal systems [67].

1.8 Magneto-Optical Phenomena

Magneto-optical phenomena refer to changes in the polarization state of light as it propagates through or interacts with a material exposed to a magnetic field. These effects arise from the coupling between the electromagnetic field of light and the magnetic order of matter, leading to magnetically induced optical anisotropy. In transparent magnetic materials, this interaction results primarily from differences in the refractive indices experienced by left- and right-circularly polarized eigenmodes, a consequence of magnetic-field-induced symmetry breaking [68]

From a macroscopic perspective, magneto-optical effects can be described by the

dielectric permittivity tensor $\boldsymbol{\varepsilon}$, whose off-diagonal components become nonzero in the presence of magnetization. For isotropic magneto-optical media such as cubic garnets, the permittivity tensor may be expressed as

$$\varepsilon = \begin{bmatrix} \varepsilon & ig & 0 \\ -ig & \varepsilon & 0 \\ 0 & 0 & \varepsilon \end{bmatrix} \qquad \text{(Eq. 9)}$$

here $\boldsymbol{\varepsilon}$ is the diagonal dielectric constant and $\boldsymbol{g}$ is the magneto-optical gyration parameter, which is proportional to the magnetization of the material [69]

The presence of the gyration term leads to circular birefringence and circular dichroism, which are responsible for magneto-optical rotation effects.

In ferrimagnetic garnets such as yttrium iron garnet (YIG) and terbium gallium garnet (TGG), magneto-optical phenomena are particularly pronounced due to strong exchange interactions, high magnetic ordering temperatures, and favorable electronic configurations of Fe^{3+} and rare-earth ions [69]. These materials combine high optical transparency with significant magnetic susceptibility, making them especially suitable for photonic applications such as Faraday rotators, optical isolators, and magnetic field sensors [70].

The magnitude of magneto-optical effects depends on intrinsic material parameters including magnetic ordering, electronic transitions, and spin–orbit coupling as well as extrinsic factors such as wavelength, temperature, applied magnetic field strength, and interaction length [71]. Consequently, understanding magneto-optical phenomena provides a critical foundation for analyzing Faraday rotation, Verdet constants, and material optimization strategies discussed in the following subsections.

1.8.1 Faraday Effect

The Faraday effect is a magneto-optical phenomenon in which the plane of polarization of linearly polarized light rotates as it passes through a transparent material in a magnetic field aligned with the light [72-73], as shown in fig 20. This happens because the magnetic field causes the left- and right-circularly polarized components of light to travel at different speeds through the material.

The rotation angle θ of the polarization plane is given by

$$\boldsymbol{\theta = VBL} \qquad \text{(Eq. 10)}$$

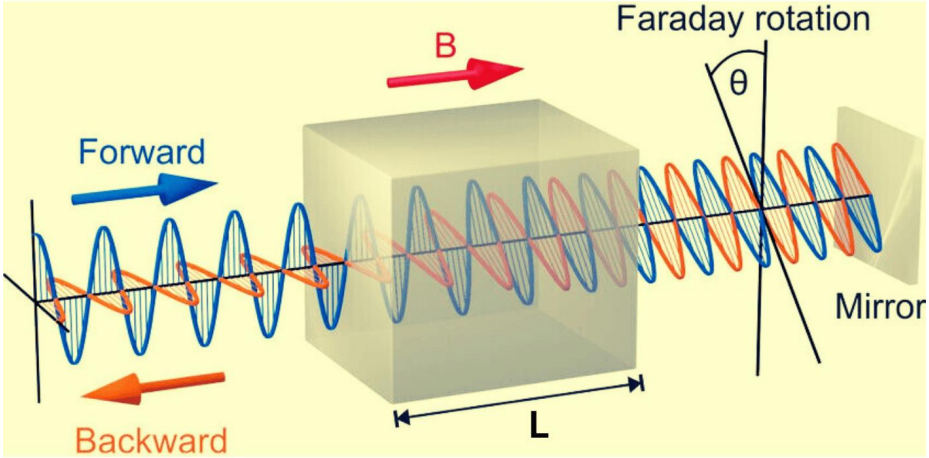

Figure 20. Schematic illustration of the Faraday effect showing polarization rotation of linearly polarized light propagating through a magnetized medium. [**72**]

where $\boldsymbol{V}$ denotes Verdet constant of the material, $\boldsymbol{B}$ represent magnetic flux density along the optical path, and $\boldsymbol{L}$ is the length of the medium.

A key characteristic of the Faraday effect is its **nonreciprocal nature**: the direction of rotation is independent of the direction of light propagation and depends solely on the direction of the applied magnetic field. As a result, the rotation accumulates upon double passage through the material rather than being canceled, which is essential for optical isolation applications [73].

From a microscopic perspective, the Faraday effect arises from magnetically induced splitting of electronic energy levels and the associated spin–orbit coupling, leading to different transition probabilities for circularly polarized light components. In ferrimagnetic garnets, this effect is strongly enhanced by exchange interactions between Fe^{3+} ions and, when present, rare-earth ions occupying the dodecahedral sites of the garnet lattice. In yttrium iron garnet ($Y_3Fe_5O_{12}$), the Faraday rotation is primarily governed by Fe^{3+} sublattices, whereas in terbium gallium garnet ($Tb_3Ga_5O_{12}$), the large paramagnetic moment of Tb^{3+} ions significantly increase the rotation magnitude, particularly in the visible and near-infrared spectral regions.

In practical photonic devices, the Faraday effect forms the operating principle of

Faraday rotators and optical isolators, where high transparency, low optical loss, thermal stability, and large Verdet constants are required. Garnet-based single crystals and glass-ceramics remain among the most effective materials for exploiting the Faraday effect due to their favorable combination of magnetic ordering and optical quality.

1.8.2 Verdet Constant

The Verdet constant V is a material-specific parameter that quantifies the strength of the Faraday effect and describes the rotation of the polarization plane per unit magnetic field and optical path length [74-75]. It is defined through the relation

$$\boldsymbol{V = \frac{\theta}{BL}} \qquad \text{(Eq. 11)}$$

where $\boldsymbol{\theta}$ is the Faraday rotation angle, $\boldsymbol{B}$ represent the magnetic flux density, and $\boldsymbol{L}$ is the optical path length.

The Verdet constant depends strongly on wavelength, temperature, and the electronic structure of the magneto-optical material. In general, V increases at shorter wavelengths and at lower temperatures, particularly in materials containing rare-earth ions with strong spin–orbit coupling [74-75].

In ferrimagnetic garnets like yttrium iron garnet (YIG), the Verdet constant is primarily governed by Fe^{3+} electronic transitions and exchange interactions between the octahedral and tetrahedral sublattices. YIG exhibits moderate Verdet constants combined with very low optical absorption, making it suitable for microwave and near-infrared magneto-optical devices. In contrast, terbium gallium garnet (TGG) is a paramagnetic garnet in which the large magnetic moment of Tb^{3+} ions produce significantly higher Verdet constants, particularly in the visible spectral range. This property, together with high optical transparency, makes TGG the material of choice for high-performance Faraday rotators and optical isolators in photonics [76-77].

Table 2 summarizes representative Verdet constant values for YIG and TGG reported in the literature at commonly used wavelengths.

Table 2. Reported Verdet Constants of YIG and TGG			
Material	**Wavelength (nm)**	**Verdet Constant (rad·T^{-1}·m^{-1})**	**Reference**
YIG	633	-131	[74]
YIG	1150	-40	[74]
YIG (film)	633	-120	[75]
TGG	633	-139.6	[77]
TGG	1064	-36.4	[88]
TGG	633	-135	[76]
TGG	1064	-36	[79]

1.8.3 Magneto-Optical Materials for Photonics

Magneto-optical (MO) materials used in photonics must combine strong magneto-optical activity with high optical transparency, low absorption losses, thermal stability, and chemical robustness. These requirements are essential for devices such as Faraday rotators, optical isolators, circulators, and magnetic field sensors operating across the visible and near-infrared spectral regions. Among the broad class of MO materials, iron garnets and rare-earth-based garnets remain the most technologically relevant due to their favorable balance between magnetic ordering and optical quality.

Ferrimagnetic iron garnets, particularly yttrium iron garnet ($Y_3Fe_5O_{12}$), are widely employed in integrated and microwave photonics because of their low coercivity, narrow hysteresis loops, and very low optical absorption at telecommunication wavelengths. Their magneto-optical response originates mainly from Fe^{3+} electronic transitions and exchange interactions between octahedral and tetrahedral sublattices. Substitution on the rare-earth or iron sites allows fine tuning of magnetic anisotropy, Faraday rotation, and optical loss, enabling material optimization for specific device requirements.

Paramagnetic garnets such as terbium gallium garnet ($Tb_3Ga_5O_{12}$) exhibit exceptionally high Verdet constants due to the strong spin–orbit coupling of Tb^{3+} ions. Although they lack spontaneous magnetization, their linear magnetic response and high transparency make them the preferred materials for bulk Faraday rotators and optical isolators in high-power laser systems. Compared to ferrimagnetic garnets, paramagnetic

garnets offer superior thermal stability and reduced magnetic hysteresis, which is advantageous for precision photonic applications.

Recent advances in magneto-optical photonics also include garnet thin films, glass-ceramics, and nanostructured composites, which enable integration with planar photonic platforms. In these systems, controlling composition, microstructure, and crystallographic orientation is critical for maximizing the magneto-optical figure of merit while maintaining low optical losses. Consequently, garnet-based materials continue to represent a cornerstone of magneto-optical photonics, bridging fundamental magnetic properties with advanced optical device functionality.

References

[1] X. Zhao *et al.*, “High Verdet Constant Glass for Magnetic Field Sensors High Verdet Constant Glass for Magnetic Field Sensor,” *ACS Appl. Mater. Interfaces*, vol. 2022, no. 51, doi: 10.1021/ac.

[2] T. Ishibashi, T. Kosaka, M. Naganuma, and T. Nomura, “Magneto-optical properties of Bi-substituted yttrium iron garnet films by metal-organic decomposition method,” in *Journal of Physics: Conference Series*, Institute of Physics Publishing, 2010. doi: 10.1088/1742-6596/200/11/112002.

[3] L. Zhang, D. Hu, I. L. Snetkov, S. Balabanov, O. Palashov, and J. Li, “A review on magneto-optical ceramics for Faraday isolators,” May 01, 2023, *Tsinghua University Press*. doi: 10.26599/JAC.2023.9220742.

[4] N. Askarzadeh and H. Shokrollahi, “Spintronic Innovations with Yttrium Iron Garnet,” Dec. 01, 2025, *Springer*. doi: 10.1007/s11664-025-12411-7.

[5] N. Askarzadeh, H. Shokrollahi, and L. Karimi, “Yttrium iron garnet: Dodecahedral substitutions,” Mar. 01, 2025, *Elsevier B.V.* doi: 10.1016/j.rechem.2025.102061.

[6] N. Askarzadeh and H. Shokrollahi, “Advances in YIG thin films: Deposition strategies and substrate effects,” Jul. 01, 2025, *Elsevier B.V.* doi: 10.1016/j.rechem.2025.102390.

[7] S. M. Yakout, “Spintronics: Future Technology for New Data Storage and Communication Devices”, doi: 10.1007/s10948-020-05545-8/Published.

[8] J. Zhan *et al.*, “Low Gilbert damping in Bi/In-doped YIG thin films with giant Faraday effect,” *Chinese Physics B*, vol. 33, no. 10, Sep. 2024, doi: 10.1088/1674-1056/ad6b84.

[9] R. Fu, Y. Li, R. Peng, Y. Lu, and Q. Wen, “High Dielectric Constant YIG Ferrites with Low Sintering Temperature,” *Journal of Materials Science: Materials in Electronics*, vol. 33, no. 8, pp. 4914–4923, Mar. 2022, doi: 10.1007/s10854-021-07681-w.

[10] J. Y. Kim, D. G. Lee, D. S. Um, J. W. A. Robinson, and M. J. Jin, “Impact of interface paramagnetism and local defects on low-temperature magnetic properties of YIG thin films on GGG,” *Phys. Rev. Mater.*, vol. 9, no. 8, Aug. 2025, doi: 10.1103/6sy6-tgs6.

[11] R. Jiang *et al.*, “Characteristics of Y3Fe5O12 ceramic at mid-infrared wavelengths and its Faraday isolator application,” *Opt. Laser Technol.*, vol. 181, Feb. 2025, doi: 10.1016/j.optlastec.2024.111829.

[12] U. V. Valiev, M. E. Malysheva, V. O. Pelenovich, A. X. Ramazanov, F. K. Turotov, and D. N. Karimov, “Magneto-Optics of Dy3+ Ion in Low-Symmetric Orthoaluminate Structure,” *Crystallography Reports*, vol. 68, no. 7, pp. 1180–1189, Dec. 2023, doi: 10.1134/S1063774523600710.

[13] D. Scheffler, O. Steuer, S. Zhou, L. Siegl, S. T. B. Goennenwein, and M. Lammel, “Aluminium substituted yttrium iron garnet thin films with reduced Curie temperature,” *Phys. Rev. Mater.*, vol. 7, no. 9, Sep. 2023, doi: 10.1103/PhysRevMaterials.7.094405.

[14] M. Watanabe, Y. Anzai, and I. Tanaka, “Characterization of defects in Tb3Ga5O12 single crystals grown by the Czochralski method,” *J. Cryst. Growth*, vol. 634, May 2024, doi: 10.1016/j.jcrysgro.2024.127687.

[15] A. Sakamoto and S. Yamamoto, “Glass-Ceramics: Engineering Principles and Applications,” *Int. J. Appl. Glass Sci.*, vol. 1, no. 3, pp. 237–247, Sep. 2010, doi: 10.1111/j.2041-1294.2010.00027.x.

[16] T. Honma, K. Maeda, S. Nakane, and K. Shinozaki, “Unique properties and potential of glass-ceramics”, doi: 10.2109/jcersj2.

[17] L. V. Albino *et al.*, “Innovative synthesis of Tm^{3+}/Er^{3+}-doped Yb-YGG single crystals for upconversion-based white light emission,” *Ceram. Int.*, vol. 51, no. 12, pp. 16700–16709, May 2025, doi: 10.1016/j.ceramint.2024.11.480.

[18] J. F. Stebbins, “Short-range Structure and Order in Oxide Glasses,” 2021.

[19] J. R. Orives *et al.*, “A supersaturated glass-melt approach for growing micrometer-sized TGG single crystals,” *Ceram. Int.*, 2025, doi: 10.1016/j.ceramint.2025.08.137.
[20] X. Tu, S. Wang, K. Xiong, Y. Zheng, and E. Shi, “Growth and properties of large aperture YCOB crystal for NLO application,” *J. Cryst. Growth*, vol. 535, Apr. 2020, doi: 10.1016/j.jcrysgro.2020.125527.
[21] Q. Zheng, L. Deng, F. Wang, A. Qiao, H. Tao, and Y. Yue, “Transparent glass-ceramics achieved by inward orientational growth of single crystals,” *J. Non. Cryst. Solids*, vol. 657, Jun. 2025, doi: 10.1016/j.jnoncrysol.2025.123505.
[22] K. M. S. Dawngliana and S. Rai, “Spectroscopic properties and Judd–Ofelt study of Ho3+ doped alumino-silicate glasses for green laser applications,” *Appl. Phys. A Mater. Sci. Process.*, vol. 131, no. 6, Jun. 2025, doi: 10.1007/s00339-025-08579-8.
[23] L. Zur *et al.*, “Glass and glass-ceramic photonic systems,” in *Integrated Optics: Devices, Materials, and Technologies XXI*, SPIE, Feb. 2017, p. 1010603. doi: 10.1117/12.2254965.
[24] A. E. Souza *et al.*, “Heavy metal oxide glass-ceramics containing luminescent gallium-garnets single crystals for photonic applications,” *J. Alloys Compd.*, vol. 864, May 2021, doi: 10.1016/j.jallcom.2021.158804.
[25] E. D. Zanotto and J. C. Mauro, “The glassy state of matter: Its definition and ultimate fate,” *J. Non. Cryst. Solids*, vol. 471, pp. 490–495, Sep. 2017, doi: 10.1016/j.jnoncrysol.2017.05.019.
[26] M. Nalin *et al.*, “Novel scalable synthesis of luminescent and magnetic single crystal garnets,” *Mater. Horiz.*, Apr. 2025, doi: 10.1039/d5mh00254k.
[27] J. Deubener *et al.*, “Updated definition of glass-ceramics,” *J. Non. Cryst. Solids*, vol. 501, pp. 3–10, Dec. 2018, doi: 10.1016/j.jnoncrysol.2018.01.033.
[28] T. Catunda, A. R. Zanatta, T. A. Lodi, L. V. Albino, and M. Nalin, “Structural and Spectroscopic Properties of ND Doped YAG Microsize Single Crystals,” in *2025 SBFoton International Optics and Photonics Conference, SBFoton IOPC 2025*, Institute of Electrical and Electronics Engineers Inc., 2025. doi: 10.1109/SBFotonIOPC66433.2025.11218524.
[29] H. O. Tekin *et al.*, “Synthesis and nuclear radiation shielding characterization of newly developed germanium oxide and bismuth oxide glasses,” *Ceram. Int.*, vol. 45, no. 18, pp. 24664–24674, Dec. 2019, doi: 10.1016/j.ceramint.2019.08.204.
[30] W. H. Dumbaugh and J. C. Lapp, “Heavy-Metal Oxide Glasses,” *Journal of the American Ceramic Society*, vol. 75, no. 9, pp. 2315–2326, 1992, doi: 10.1111/j.1151-2916.1992.tb05581.x.
[31] M. A. Marzouk, S. M. Abo-Naf, H. A. Zayed, and N. S. Hassan, “Integration Between Optical and Structural Behavior of Heavy Metal Oxide Glasses Doped with Multiple Glass Formers,” *Silicon*, vol. 10, no. 1, pp. 21–28, Jan. 2018, doi: 10.1007/s12633-015-9342-3.
[32] J. Bhemarajam, P. S. Prasad, M. M. Babu, M. Özcan, and M. Prasad, “Investigations on structural and optical properties of various modifier oxides (Mo = zno, cdo, bao, and pbo) containing bismuth borate lithium glasses,” *Journal of Composites Science*, vol. 5, no. 12, Dec. 2021, doi: 10.3390/jcs5120308.
[33] M. A. Sayed, B. Basha, N. Al-Harbi, A. M. Al-Baradi, and K. S. Shaaban, “PbO effect on physical, mechanical, optical, structural, and radiation characteristics of P2O5-BaO-PbO glass system,” *Eur. Phys. J. Plus*, vol. 138, no. 5, May 2023, doi: 10.1140/epjp/s13360-023-04079-x.
[34] M. I. Sayyed, C. V. More, S. Biradar, and K. A. Mahmoud, “Physical, mechanical, optical properties and gamma-ray protection performance of high-density BaO–PbO2–B2O3–Ho2O3 glasses: Effect of B2O3 / PbO2+Ho2O3 substitution,” *Radiation Physics and Chemistry*, vol. 235, Oct. 2025, doi: 10.1016/j.radphyschem.2025.112878.
[35] M. S. Al-Buriahi *et al.*, “Effects of reducing PbO content on the elastic and radiation attenuation properties of germanate glasses: a new non-toxic candidate for shielding applications,” *Journal of Materials Science: Materials in Electronics*, vol. 32, no. 11, pp.

15080–15094, Jun. 2021, doi: 10.1007/s10854-021-06060-9.
[36] R. Mishra *et al.*, “Structural, thermo-mechanical, optical and gamma-ray shielding properties of lead-free BaO–ZnO–B2O3–SiO2 and lead-based PbO–Bi2O3–K2O–SiO2 glasses,” *Ceram. Int.*, vol. 50, no. 20, pp. 38495–38506, Oct. 2024, doi: 10.1016/j.ceramint.2024.07.214.
[37] M. A. Marzouk and A. M. Fayad, “Heavy metal oxide glass responses for white light emission,” *Journal of Materials Science: Materials in Electronics*, vol. 31, no. 17, pp. 14502–14511, Sep. 2020, doi: 10.1007/s10854-020-04010-5.
[38] C. Guguschev *et al.*, “Novel diamagnetic garnet-type substrate single crystals for ultralow-damping yttrium iron garnet Y3Fe5O12 films at cryogenic temperatures.”
[39] B. Cockayne, W. R. Macewan, and G. T. Brown, “Impurities in single crystal indium phosphide,” 1980.
[40] T. Berry, N. Ng, and T. M. McQueen, “Tools and Tricks for Single Crystal Growth,” May 28, 2024, *American Chemical Society*. doi: 10.1021/acs.chemmater.3c03077.
[41] C. T. Sun and D. F. Xue, “Pulling growth technique towards rare earth single crystals,” Sep. 01, 2018, *Springer Verlag*. doi: 10.1007/s11431-018-9257-6.
[42] J. W. Nielsen and E. F. Dearborn, “P&?r. C’hem. Solids Pergamon Press,” 1958.
[43] M. Nagao, “Crystal Growth Techniques for Layered Superconductors,” Sep. 26, 2017. doi: 10.20944/preprints201709.0129.v1.
[44] J. W. Nielsen, “Improved method for the growth of yttrium-iron and yttrium-gallium garnets,” *J. Appl. Phys.*, no. 5, 1960, doi: 10.1063/1.1984601.
[45] C. Prog and C. Growth, “KINETICS AND MECHANISMS OF FLUX CRYSTAL GROWTH,” 1990.
[46] H. Shen *et al.*, “Recent advances of rare earth iron garnet magneto-optical single crystals,” *J. Cryst. Growth*, vol. 631, Apr. 2024, doi: 10.1016/j.jcrysgro.2024.127626.
[47] B. Cockayne, “ofC~yst~ 6to~t~ ~l (1~7?) ~13-~26 ~No~t~•l~ollü.n~ ?~lis~~ C~i~’ THE MELT GROWTH OF OXIDE AND RELATED SINGLE CRYSTALS.”
[48] Y. Jiang, H. Shen, J. Xu, J. Ma, H. Wang, and B. Lu, “Large size rare earth iron garnet single crystals grown by the flux–Bridgman method,” *Journal of Rare Earths*, vol. 39, no. 12, pp. 1547–1553, Dec. 2021, doi: 10.1016/j.jre.2021.03.020.
[49] M. Watanabe *et al.*, “Czochralski growth and composition control of Tb3Ga5O12 single crystals,” *J. Cryst. Growth*, vol. 665, Sep. 2025, doi: 10.1016/j.jcrysgro.2025.128205.
[50] J. Friedrich, “Methods for Bulk Growth of Inorganic Crystals: Crystal Growth,” in *Reference Module in Materials Science and Materials Engineering*, Elsevier, 2016. doi: 10.1016/b978-0-12-803581-8.01010-9.
[51] S. Kimura and I. Shindo, “SINGLE CRYSTAL GROWTH OF YIG BY THE FLOATING ZONE METHOD,” 1977.
[52] S. Kimura, K. Kitamura, and I. Shindo, “Growth of rare earth garnet crystals by the floating zone method,” *J. Cryst. Growth*, vol. 65, no. 1–3, pp. 543–548, Dec. 1983, doi: 10.1016/0022-0248(83)90100-8.
[53] M. Geho, T. Sekijima, and T. Fujii, “Growth of terbium aluminum garnet (Tb3Al5O 12; TAG) single crystals by the hybrid laser floating zone machine,” *J. Cryst. Growth*, vol. 267, no. 1–2, pp. 188–193, Jun. 2004, doi: 10.1016/j.jcrysgro.2004.03.068.
[54] Y. Cho, Y. W. Nahm, C. Decorse, and S. Cho, “Two-Step Floating Zone Method for Single-Crystal Growth of Er-Doped Y3Fe5O12,” *ACS Omega*, vol. 10, no. 27, pp. 29421–29427, Jul. 2025, doi: 10.1021/acsomega.5c02558.
[55] Z. Chen, L. Yang, Y. Hang, and X. Wang, “Growth and magneto-optical characteristics of cerium-doped terbium gallium garnet by the floating zone method,” *Crystal Research and Technology*, vol. 50, no. 7, pp. 528–531, Jul. 2015, doi: 10.1002/crat.201500007.
[56] W. Piekarczyk, “THERMODYNAMIC ANALYSIS OF THE Y 3Fe5O12-CCI4 SYSTEM AND

GROWTH OF YIG SINGLE CRYSTALS BY CHEMICAL VAPOUR TRANSPORT WITH CC!4 AS A TRANSPORTING AGENT," 1981.
[57] C. A. Sonego, H. Li, P. Einarsson Nielsen, J. C. Lashley, M. A. Avila, and S. E. Rowley, "The Growth of V5S8 Single Crystals by Chemical Vapour Transport," *Brazilian Journal of Physics*, vol. 54, no. 5, Oct. 2024, doi: 10.1007/s13538-024-01554-3.
[58] J. Zeng, "Critique of the Landé g-factor and Spin Quantum Number, and Reconstruction of Classical Atomic Structure Theory," Dec. 18, 2025. doi: 10.20944/preprints202512.1673.v1.
[59] "Fundamentals of Magnetism. " Getzlaff, M. (2007). Fundamentals of magnetism. Springer Science & Business Media. No. pp. 6
[60] L. B. Kong, L. Liu, Z. Yang, S. Li, T. Zhang, and C. Wang, "Theory of ferrimagnetism and ferrimagnetic metal oxides," in *Magnetic, Ferroelectric, and Multiferroic Metal Oxides*, Elsevier, 2018, pp. 287–311. doi: 10.1016/B978-0-12-811180-2.00015-3.
[61] W. H. Zachariasbn, "THE ATOMIC ARRANGEMENT IN GLASS," 1932. [Online]. Available: https://pubs.acs.org/sharingguidelines
[62] N. Rodziah, M. Hashim, I. R. Idza, I. Ismayadi, A. N. Hapishah, and M. A. Khamirul, "Dependence of developing magnetic hysteresis characteristics on stages of evolving microstructure in polycrystalline yttrium iron garnet," *Appl. Surf. Sci.*, vol. 258, no. 7, pp. 2679–2685, Jan. 2012, doi: 10.1016/j.apsusc.2011.10.117.
[63] S. da S. Marins, T. Ogasawara, and A. S. Ogasawara, "Terbium-yttrium-iron garnet revisited," *J. Alloys Compd.*, vol. 436, no. 1–2, pp. 415–420, Jun. 2007, doi: 10.1016/j.jallcom.2006.11.114.
[64] D. C. Jiles and D. L. Atherton, "THEORY OF FERROMAGNETIC HYSTERESIS t," 1986.
[65] E. Rosenberg *et al.*, "Revealing Site Occupancy in a Complex Oxide: Terbium Iron Garnet."
[66] D. L. Atherton, "FERROMAGNETIC HYSTERESIS," 1983.
[67] C. Rizal, H. Shimizu, and J. R. Mejía-Salazar, "Magneto-Optics Effects: New Trends and Future Prospects for Technological Developments," Sep. 01, 2022, *MDPI*. doi: 10.3390/magnetochemistry8090094.
[68] D. Yan and H. Wang, "Magneto-optical properties and gyration vectors of iron garnet films containing different bismuth ions," *Appl. Phys. A Mater. Sci. Process.*, vol. 129, no. 7, Jul. 2023, doi: 10.1007/s00339-023-06773-0.
[69] L. V. Albino *et al.*, "Paramagnetic borotungstate glasses with high terbium concentration for magneto-optical applications," *J. Non. Cryst. Solids*, vol. 627, Mar. 2024, doi: 10.1016/j.jnoncrysol.2023.122811.
[70] S. Kumari, "A comprehensive study of magneto-optic materials and its applications," *Mater. Today Proc.*, vol. 56, pp. 100–106, Jan. 2022, doi: 10.1016/j.matpr.2021.12.325.
[71] D. Floess and H. Giessen, "Nonreciprocal hybrid magnetoplasmonics," Oct. 01, 2018, *Institute of Physics Publishing*. doi: 10.1088/1361-6633/aad6a8.
[72] I. Snetkov and J. Li, "Selection of Magneto-Optical Material for a Faraday Isolator Operating in High-Power Laser Radiation," Dec. 01, 2022, *MDPI*. doi: 10.3390/magnetochemistry8120168.
[73] N. B. Er, W. A. CROSSLEYi, R. W. COOPERi AÃD J L PAGE, and R. P. vAN STAPErz, "P H YS I CAL REVIEW Faraday Rotation in Rare-Earth Iron Garnets," 1969.
[74] P. Hansen, K. Witter, and W. Tolksdorf, "Magnetic and magneto-optic properties of lead-and bismuth-substituted yttrium iron garnet films," 1983.
[75] D. J. Dentz, R. C. Puttbach, and R. F. Belt, "TERBIUM GALLIUM GARNET FOR FARADAY EFFECT DEVICES.," AIP (Conf Proc n 18, 1974, pp. 954–958. doi: 10.1063/1.3141859.
[76] O. Slezak, R. Yasuhara, A. Lucianetti, and T. Mocek, "Wavelength dependence of magneto-optic properties of terbium gallium garnet ceramics," *Opt. Express*, vol. 23, no. 10, p. 13641, May 2015, doi: 10.1364/oe.23.013641.
[77] R. Yasuhara *et al.*, "Design and Performance of a Diode-Pumped Nd:Silica-Phosphate Glass

Zig-Zag Slab Laser Amplifier for Inertial Fusion Energy," 2006. doi: 10.1364/OA_License_v1#VOR.
[78] H. Yoshida *et al.*, "Faraday effect; (140.3580) Lasers, solid-state," EDP sciences, 2006. doi: 10.1364/OA_License_v1#VOR.

CHAPTER 2 – MATERIALS AND EXPERIMENTAL METHODS

2. Raw Materials

All raw materials used for the preparation of the glass and glass-ceramic samples were of analytical grade and used as received without further purification. The starting oxides included BaO (99.9%, Sigma-Aldrich), PbO (99.99%, Sigma-Aldrich), Bi_2O_3 (99.9%, Sigma-Aldrich), GeO_2 (99.99%, Sigma-Aldrich), Ga_2O_3 (99.99%, Sigma-Aldrich), Y_2O_3 (99.99%, Sigma-Aldrich), Fe_2O_3 (99.9%, Lumintech), and Tb_4O_7 (99.9%, Lumintech).

Nitric acid (HNO_3, 37%, Exodo Científica) was used during the post-processing stage for selective crystal recovery/extraction from the amorphous phase.

The compositions were formulated according to the required stoichiometry for each system, and batches were prepared for both PbO- and BaO-containing glass matrices.

2.1 Glass Synthesis

The synthesis of the PbO- and BaO-based glass compositions as presented in Table 3. ($PbO–GeO_2–Ga_2O_3–Bi_2O_3$ and $BaO–GeO_2–Ga_2O_3–Bi_2O_3$) was carried out at the Laboratório de Vidros Especiais (LAVie), Institute of Chemistry, UNESP, Araraquara–SP. The base glass compositions were prepared by melting the respective oxides in platinum crucibles using high-temperature furnaces capable of reaching up to 1400 °C. Precise temperature control was maintained throughout the process to ensure compositional homogeneity and to minimize the incorporation of impurities that could interfere with crystallization or alter the final glass properties.

Table 3. Bulk Glasses for PGGB and BGGB

Nominal Compositions in mol %						
Sample	**PbO**	**BaO**	**GeO_2**	**Ga_2O_3**	**Bi_2O_3**	**Total**
PGGB	40	0.00	20	15	25	100
BGGB	0.00	40	20	15	25	100

Before melting, high-purity raw materials (PbO, BaO, Bi_2O_3, GeO_2, and Ga_2O_3) were accurately weighed and mixed using a Flactek speed mixer machine to guarantee uniform blending. For each composition, 10 g batches were prepared. The homogeneous mixtures were then melted for approximately 1 h at temperatures ranging from 1250 °C to 1300 °C, depending on the specific glass system. Careful attention was given to achieve complete homogenization of the melt, which is essential for producing optically clear, bubble-free glasses.

The molten glass was subsequently cast into preheated molds maintained at 300 – 500 °C, depending on the composition, and then transferred to an annealing furnace to relieve thermal stress and prevent optical anisotropy. The annealing process lasted 6–8 h at a temperature below the glass transition temperature (Tg), as determined by differential scanning calorimetry (DSC) (Figure 28). After annealing, the samples were slowly cooled inside the furnace to room temperature to avoid thermal shock and cracking.

Finally, the annealed glass samples were polished using silicon carbide (SiC) abrasive papers of progressively finer grain sizes until an optically smooth surface was obtained. This polishing step was critical to prepare the samples for subsequent optical, structural, and thermal characterizations.

2.2 Synthesis of $Tb_3Ga_5O_{12}$ (TGG) Single Crystals with Pb-Free Glass

Different batch compositions were designed by gradually replacing PbO with BaO while preserving the stoichiometric proportions required for $Tb_3Ga_5O_{12}$ (TGG) formation. Five compositions, labeled C1–C5, were prepared and investigated in this work. For each composition, 5 g glass batches were weighed using an analytical balance with a precision of ±0.001 g. The precursor powders were initially mixed in an agate mortar and subsequently homogenized using a Speed Mixer (DAC) for 5 min before melting. The compositions investigated are listed in Table 4.

Table 4. The glass-ceramics for TGG single crystals							
Nominal Compositions in mol %							
Sample	**PbO**	**BaO**	**GeO_2**	**Ga_2O_3**	**Bi_2O_3**	**Tb_4O_7**	**ToTal**
C1	39.4	0.00	19.7	18.8	24.6	1.5	100
C2	29.4	9.8	19.6	14.7	24.5	2	100
C3	19.6	19.6	19.6	14.7	24.5	2	100
C4	9.8	29.4	19.6	14.7	24.5	2	100
C5	0.00	39.2	19.6	14.7	24.5	2	100

The prepared powder batches were melted in platinum crucibles using an electric furnace under a controlled heating schedule (Fig. 21). Initially, the mixtures were heated to 700 °C at a rate of 20 °C·min^{-1} and briefly held for 1 min to eliminate residual volatiles. The temperature was then increased to 1100 °C at 10 °C·min^{-1} and maintained for 1 min to ensure proper melting of the lower-temperature components.

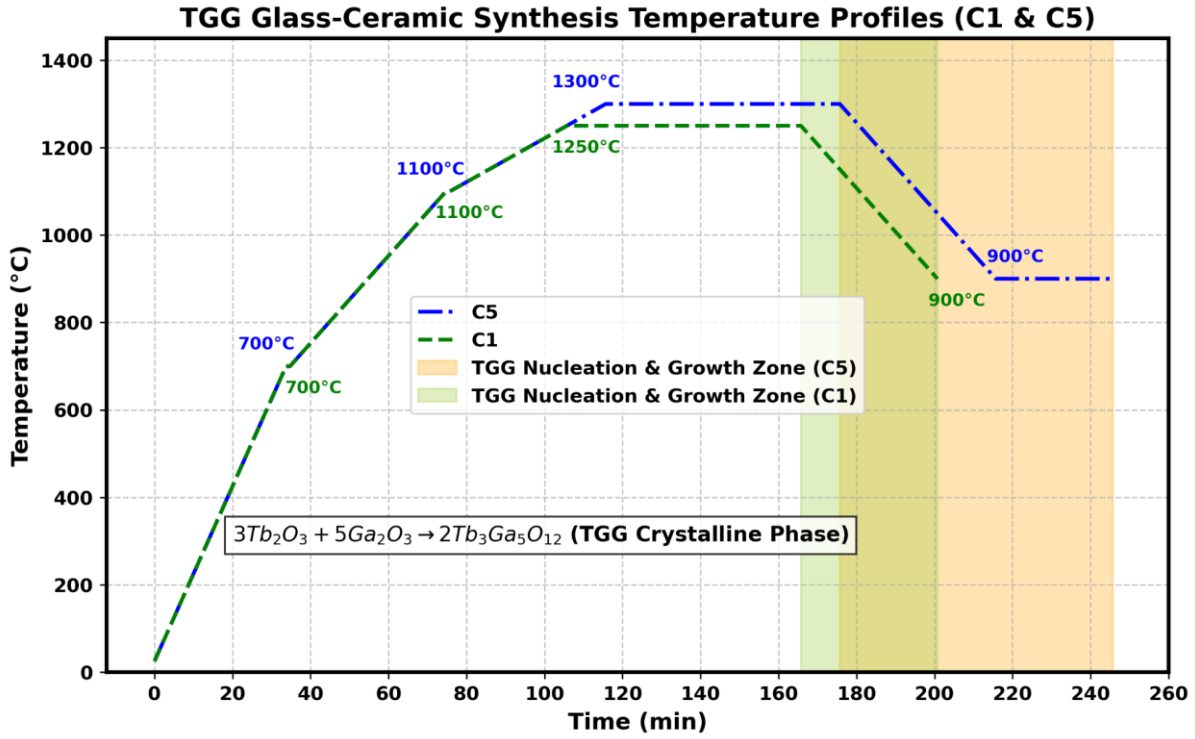

Figure 21. TGG Glass-ceramic synthesis temperature profile of C1 and C5

Further heating was carried out at 5 °C·min^{-1} up to the final melting temperatures, which were set at 1250 °C for PbO-containing compositions and 1300 °C for BaO-containing

compositions. The melts were held at these temperatures for 2 h to achieve full homogenization and to avoid phase separation.

After this stage, controlled cooling was applied at a rate of 10 °C·min^{-1} down to 900 °C. For compositions C1–C4, the crucibles were removed from the furnace immediately upon reaching this temperature. In contrast, the fully Pb-free composition (C5) was held at 900 °C for 30 min before removal. This additional holding step accounts for the higher viscosity of BaO-rich melts Click or tap here to enter text.Click or tap here to enter text. and supports the formation of well-defined cubic crystals.

This cooling approach promotes sufficient undercooling and supersaturation within the melt, which are necessary conditions for the nucleation and growth of TGG crystals inside the glass matrix. After removal at 900 °C, the samples consisted of a glassy phase containing embedded micrometer-sized crystals.

2.3 Synthesis of $Y_3Fe_5O_{12}$ (YIG) Glass-Ceramics

The glass-ceramics were synthesized from the base glass compositions by substituting Ga_2O_3 with Fe_2O_3 and introducing Y_2O_3, followed by controlled crystallization to promote the in-situ formation of yttrium iron garnet ($Y_3Fe_5O_{12}$, YIG) within the glass matrix. The powdered batches, as summarized in Tables 5-7, were melted in platinum crucibles using an electric furnace (Figure 22) under a carefully controlled thermal program (Figure 23).

Table 5. PbO-based GC compositions for $Y_3Fe_5O_{12}$ (YIG) single crystals.

Nominal composition (mol%)						
Label	***PbO***	***Bi_2O_3***	***GeO_2***	***Fe_2O_3***	***Y_2O_3***	***Total***
Pb_YIG1	38	15	20	22	5	100
Pb_YIG2	38	14.5	20	22	5.5	100
Pb_YIG3	38	13	20	24	5	100
Pb_YIG4	38	15	20	22.5	4.5	100
Pb_YIG5	38	15	20	24	3.29	100

Table 6. BaO-based GC compositions for $Y_3Fe_5O_{12}$ (YIG) single crystals.						
Nominal composition (mol%)						
Label	***BaO***	***Bi_2O_3***	***GeO_2***	***Fe_2O_3***	***Y_2O_3***	***Total***
Ba_YIG1	38	15	20	22	5	100
Ba_YIG2	38	14.5	20	22	5.5	100
Ba_YIG3	38	13	20	24	5	100
Ba_YIG4	38	14	20	22.5	5.5	100
Ba_YIG5	38	12	20	23	7	100

Table 7. PbO & BaO Mixed GC compositions for $Y_3Fe_5O_{12}$ (YIG) single crystals.							
Nominal composition (mol%)							
Label	**PbO**	**BaO**	**Bi_2O_3**	**GeO_2**	**Fe_2O_3**	**Y_2O_3**	**Total**
PB-YIG5%	28.5	9.5	15	20	22	5	100

Initially, the mixtures were heated to 700 °C at 20 °C·min^{-1} and held for 1 min to remove volatile components.

Figure 22. Schematic of YIG single-crystal synthesis in glass-ceramics.

The temperature was then increased to 1100 °C at 10 °C·min^{-1} and held for 10 min to ensure complete dissolution of low-melting oxides. Subsequently, the temperature was raised to the final melting temperatures of 1300 °C for the PbO-based system and 1350 °C for the BaO-based system and maintained for 1 h to promote chemical homogeneity and prevent phase segregation.

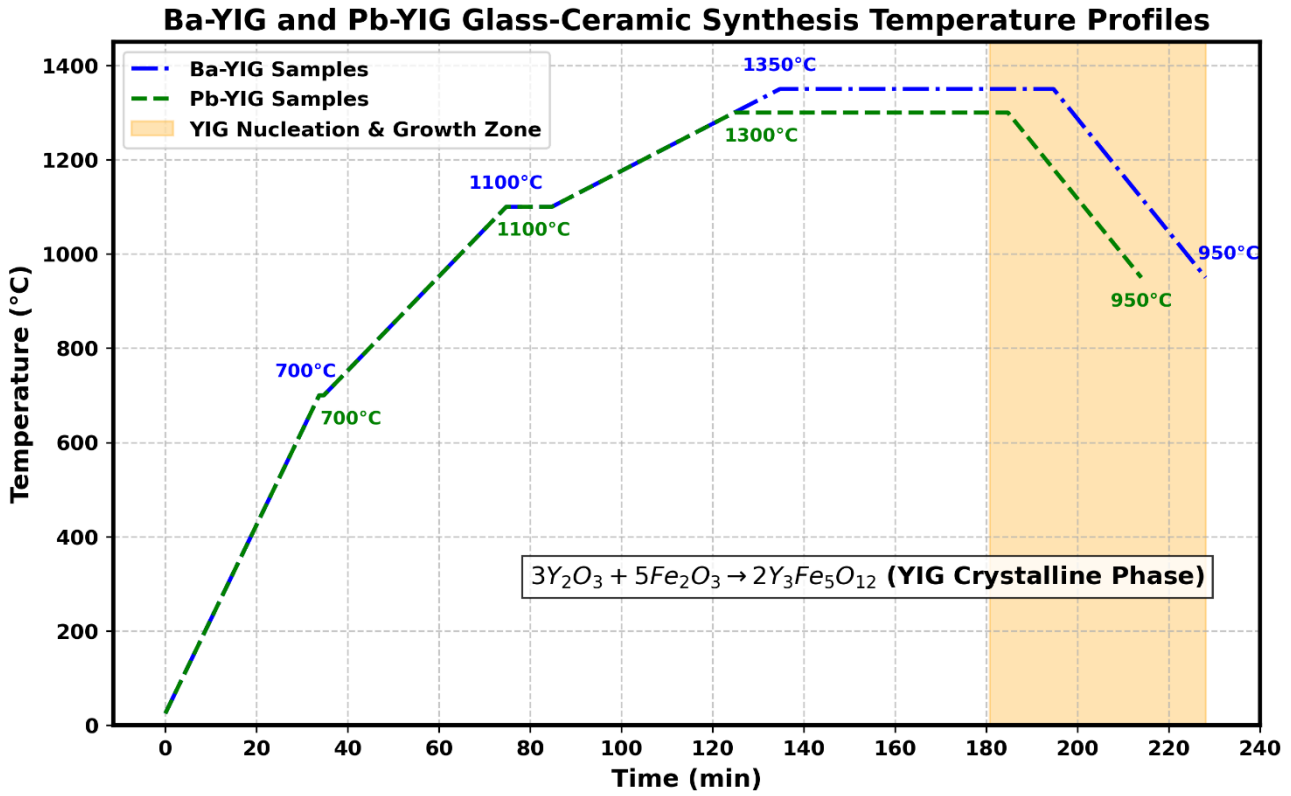

Figure 23. Thermal profile used to synthesize YIG single-crystals.

After homogenization, the furnace was cooled at a controlled rate of 12 °C·min^{-1} down to 950 °C. At this point, the crucible was removed from the furnace, and the resulting samples exhibited an opaque appearance, indicating successful crystallization. This controlled cooling process promotes nucleation and subsequent crystal growth, leading to the formation of micrometer-sized YIG crystals uniformly distributed within the glassy matrix.

2.4 Crystal Isolation and Extraction (TGG and YIG)

The isolation of crystalline phases (TGG and YIG) from the glass-ceramic matrix was carried out by selective dissolution of the residual glass phase using nitric acid (HNO_3). The thermally treated samples were immersed in 5 mL of HNO_3 for 24 h, allowing the acid to dissolve the glassy matrix while preserving the embedded crystals.

After the etching process, the suspension was filtered to recover the liberated crystals. The collected crystals were thoroughly washed with deionized water and isopropyl alcohol to remove any residual acid. Finally, the samples were dried at 100 °C to ensure complete moisture removal prior to further structural and morphological characterization. SEM observations shown in Fig. 24 reveal the presence of YIG crystals embedded in the glass-ceramic matrix prior to etching, and the well-defined, isolated cubic crystals obtained after chemical extraction.

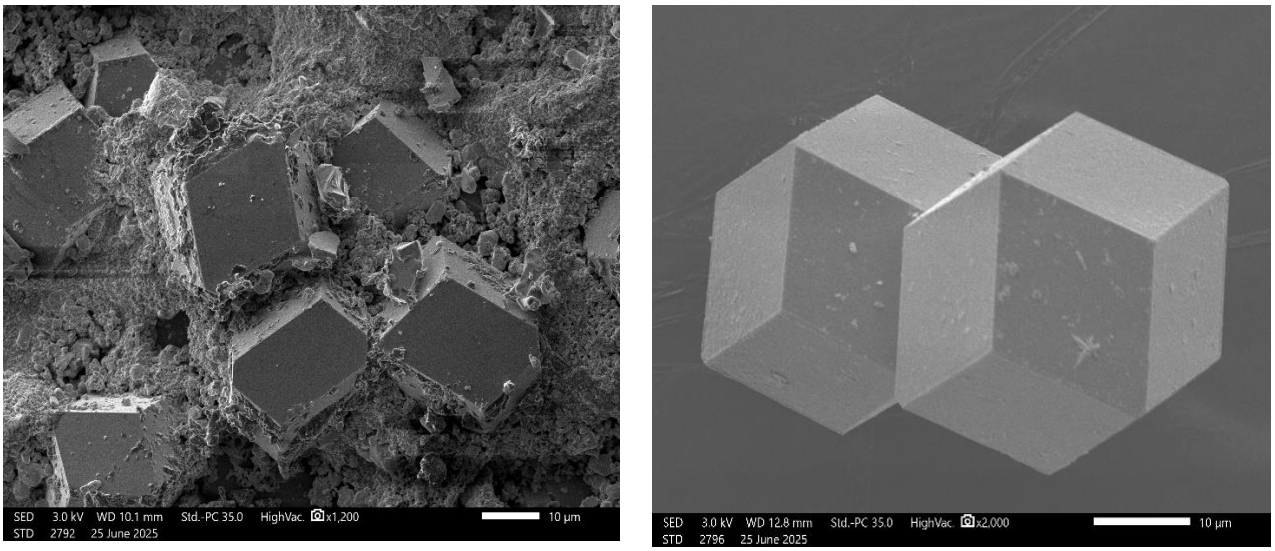

(a) **(b)**

Figure 24. SEM images of $Y_3Fe_5O_{12}$ (YIG) crystals: (a) YIG crystals embedded within the glass-ceramic matrix after thermal treatment, and (b) isolated YIG single crystals obtained after chemical etching of the residual glass phase.

2.5 Characterization Techniques

2.5.1 Differential Scanning Calorimetry (DSC)

Differential scanning calorimetry (DSC) is a thermal analysis technique used to investigate the thermal behavior of materials by measuring heat flow as a function of temperature. For glass systems, DSC is commonly employed to determine characteristic temperatures such as the glass transition temperature (Tg), crystallization temperature (Tx), and melting temperature (Tm), providing information about thermal stability and crystallization behavior.

In this work, DSC measurements were performed at the Institute of Chemistry (IQ), UNESP, Araraquara-SP, using a Netzsch DSC 404 F3 Pegasus instrument. Approximately 30 mg of glass sample was placed in platinum crucibles and heated at a rate of 10 °C·min^{-1} up to 900 °C under a nitrogen atmosphere, using an empty platinum crucible as the reference. The measurement uncertainty was approximately ±3 °C for Tg and Tx.

2.5.2 Optical Microscopy

Optical microscopy was used to examine the morphology, size distribution, and spatial arrangement of the formed crystals within the glass-ceramic matrix. The analysis focused on $Y_3Fe_5O_{12}$ (YIG) and $Tb_3Ga_5O_{12}$ (TGG) crystals. The observations were carried out using a Leica DM2500M optical microscope equipped with 5, 10, 20, 50, and 100x objective lenses, providing both low-magnification overview and detailed inspection of the microstructure.

Images were obtained from both bulk glass-ceramic samples and from crystals isolated after removal of the glassy matrix. This approach enabled evaluation not only of the distribution of crystals within the matrix but also of their individual morphology and size, without interference from the surrounding glass phase.

2.5.3 SEM-EDS Analysis

Scanning Electron Microscopy (SEM) coupled with Energy-Dispersive X-ray Spectroscopy (EDS) was used to study the surface morphology, and chemical composition was investigated using field-emission scanning electron microscopy (FEG-SEM, *JEOL JSM-7500F*). Elemental mapping and spot analyses were obtained using an *UltraDry EDS detector* (Thermo Fisher Scientific) operated at 10.0 kV with a take-off angle of 49.1°. Samples were gold-coated prior to imaging to improve conductivity.

2.5.4 X-Ray Diffraction Powder

X-ray diffraction (XRD) is a widely used technique for investigating the structural characteristics of materials and identifying crystalline and amorphous phases. The technique is based on the diffraction of X-rays by atomic planes in a material, producing characteristic diffraction patterns that can be used to determine phase composition and crystal structure. Crystalline materials generate sharp diffraction peaks, whereas amorphous materials typically exhibit broad diffuse halos due to the absence of long-range structural order.

In this work, XRD measurements were performed on powdered samples to identify crystalline phases and confirm the formation of $Y_3Fe_5O_{12}$ (YIG) and $Tb_3Ga_5O_{12}$ (TGG) crystals within the glass matrices. The analyses were carried out using a Bruker D8 Advance diffractometer equipped with Cu Kα radiation (λ = 1.5406 Å). Data were collected over a 2θ range of 10–80° with a step size of 0.02° and a scanning rate of $1°\cdot min^{-1}$ at room temperature.

2.5.5 (2.5.4.1) X-Ray Diffraction Single-crystal

Single-crystal X-ray diffraction data were collected using an XtaLAB Synergy diffractometer equipped with a HyPix hybrid pixel detector and a microfocus sealed-tube X-ray source, operating with Mo Kα radiation (λ = 0.71073 Å). The measurements were carried out at 100 K in order to reduce thermal vibrations and improve data quality.

Data collection, integration, scaling, and absorption correction were performed using

the CrysAlisPro software package. The crystal structure was solved by intrinsic phasing with SHELXT and refined using full-matrix least-squares on F^2 with SHELXL, both implemented within the Olex2 interface.

The refinement proceeded smoothly, with well-defined atomic positions and displacement parameters, and no restraints were required. This indicates a high-quality crystal structure and reliable diffraction data.

2.5.6 Raman Spectroscopy

Raman spectroscopy is a vibrational characterization technique based on the inelastic scattering of monochromatic light by the material. The resulting Raman bands provide information about the local bonding environment, crystal structure, and vibrational modes of the material. Because Raman-active modes are associated with changes in polarizability, Raman spectroscopy is complementary to infrared (IR) spectroscopy, which depends on changes in dipole moment.

In this work, Raman measurements were performed at room temperature to confirm the formation of the garnet phase and evaluate the structural integrity of the crystals. The analyses were carried out using a Jobin-Yvon Horiba LABRAM HR 800 micro-Raman spectrometer. A He–Ne laser with an excitation wavelength of 632 nm and an output power of 17 mW was used for the measurements.

2.5.7 Fourier-Transform Infrared Spectroscopy (FTIR)

Fourier Transform Infrared Spectroscopy (FTIR) were recorded using a *Thermo Scientific Nicolet iS5* spectrometer equipped with an iD1 transmission module. Measurements were collected in the 4000–400 cm^{-1} range, with a resolution of 2 cm^{-1} and 64 scans for both background and sample. Samples were mixed with KBr (Merck spectroscopy grade) and pressed into pellets at 5 tons for 1 min.

2.5.8 UV-Visible-NIR spectroscopy

UV–Visible–NIR spectroscopy was used to evaluate the optical properties of the samples by measuring their transmission over a broad spectral range. The technique is based on the interaction of electromagnetic radiation with the material, resulting in electronic transitions that depend on its structure and composition. In this work, special attention was given to the transparency at 1550 nm, a wavelength of particular interest for telecommunications and magneto-optical applications. The measurements were performed using an Agilent Cary 5000 UV–Vis–NIR spectrophotometer in transmission mode over the wavelength range of 350–2000 nm.

2.5.9 Linear Refractive Index

The refractive index of the bulk PGGB and BGGB glass samples was measured using the prism coupling technique with a Metricon 2010/M M-lines spectrometer at a wavelength of 632 nm. This technique is based on coupling a laser beam into the sample through a high-refractive-index prism. At specific incident angles, light is coupled into the material, producing characteristic mode lines that are directly related to the refractive index. The Metricon system uses this principle to provide rapid and accurate refractive index measurements of bulk materials.

2.5.10 Magnetic Susceptibility Measurements (SQUID)

Magnetic measurements were carried out at the Laboratory of Nanomaterials Synthesis and Magnetic Characterization (LSNCM) using a VSM–SQUID magnetometer (Quantum Design PPMS3). The superconducting quantum interference device (SQUID) technique is highly sensitive and allows accurate detection of very small magnetic signals.

Magnetization curves were recorded as a function of the applied magnetic field up to 70 kOe at temperatures of 2 K and 300 K. In addition, temperature-dependent magnetic susceptibility measurements were performed over the range of 2–300 K under a constant applied field of 100 Oe.

CHAPTER 3 – RESULTS AND DISCUSSION

3. RESULTS AND DISCUSSION FOR TGG SINGLE CRYSTALS

The TGG system was employed as a model to validate the feasibility of the Pb-free BaO-based supersaturated glass-melt route for garnet crystallization. This approach builds on previous work using PbO-based systems [1], with the aim of assessing whether BaO can effectively replace PbO while maintaining controlled nucleation and growth of garnet single crystals.

The results obtained in this work demonstrate that BaO can successfully replace PbO for the synthesis of micrometer-sized $Tb_3Ga_5O_{12}$ (TGG) single crystals using the supersaturated glass-melt approach. A series of glass compositions (C1–C5) was prepared by progressively decreasing the PbO content while increasing the BaO proportion, with the Tb_4O_7 concentration fixed at 2 mol%.

It was observed that the fully Pb-free composition (C5) required a higher melting temperature of 1300 °C, along with adjustments in the thermal treatment conditions. This behavior is attributed to the higher viscosity and structural rigidity of BaO-rich glass melts. Despite these changes, well-defined TGG single crystals were successfully formed within the glass matrix, indicating that BaO-based heavy metal oxide glasses are suitable hosts for controlled crystallization of garnet phases. Based on these observations, the composition $98(39.2BaO–24.5Bi_2O_3–19.6GeO_2–14.7Ga_2O_3)–2Tb_4O_7$ was selected as the optimized system for further investigation. To the best of our knowledge, this specific composition has not been previously reported for TGG crystal growth. In the following sections, the thermal properties of the glasses, as well as the structural, morphological, and optical characteristics of the TGG crystals formed within the glass matrix, are presented and discussed.

Importantly, the successful crystallization of TGG in BaO-based glass confirms that Pb-free compositions can support garnet formation using this approach. This validation provides the basis for extending the same design strategy to the synthesis of $Y_3Fe_5O_{12}$ (YIG) glass-ceramics, which are discussed in chapter 4 of this project.

3.1 Glass conception and optical properties of the bulk matrices

To understand how replacing PbO with BaO affects the crystallization of TGG, the optical properties of the base glass matrices were first examined. The study focused on the undoped glasses. The appearance of the bulk glasses is shown in Fig. 26.

Figure 26. *The blank glasses for PbO (PGGB) and BaO-based systems (BGGB).*

The UV-Vis-NIR absorption spectra of the PbO-based (PGGB) and BaO-based (BGGB) glasses are presented in Fig. 27, while the refractive index measured at 632 nm was used to give additional information about their optical behavior.

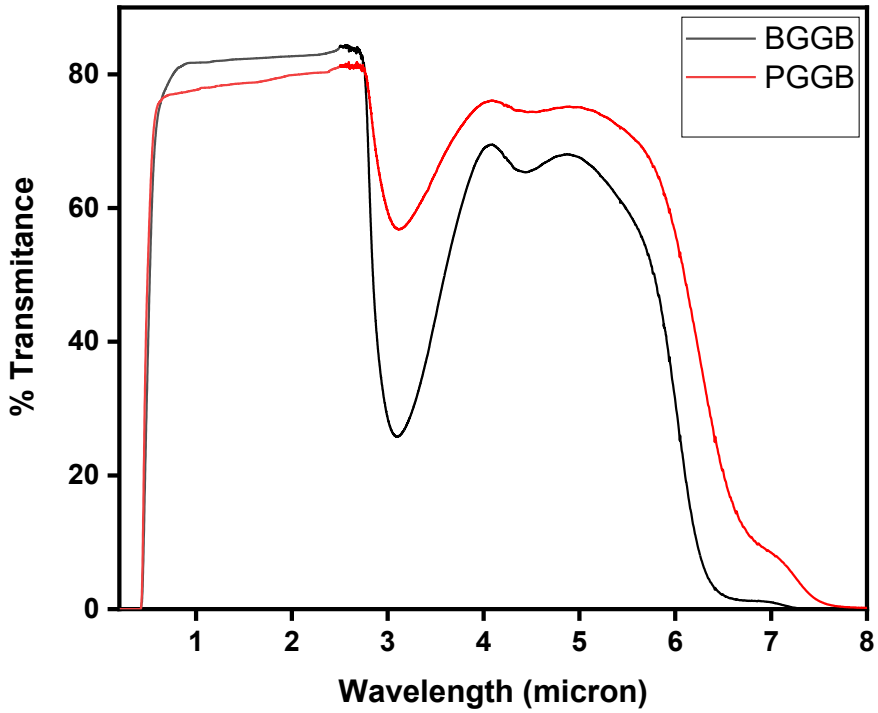

Figure 27. Optical transmittance window of both lead containing-PGGB and barium containing-BGGB glasses from UV to mid-infrared.

The absorption spectra show some differences between the two glass types. Both have good transparency in the 0.5 to 2.5 microns range and a sharp absorption edge in the visible region due to electronic transitions. The BaO-based glass has slightly lower infrared transmission than the PbO-based glass, which is likely due to differences in network connectivity, modifier-field strength, and the vibrational modes of Ba–O bonds. These factors increase phonon-related absorption in the infrared region. Both samples show water absorption bands around 3.1 μm [48], linked to O-H groups from sample preparation. There is also an absorption band around 4.3 μm, which is due to atmospheric CO_2 and its strong vibrational absorption in this region [49-50]. The PGGB glass has more extended multiphonon absorption, likely because lead is heavier than barium. Still, these differences do not have a major impact on the infrared transparency of the BGGB glass. The optical window was measured using two different pieces of equipment, as explained in the experimental section, and the curves were slightly adjusted to match at 2.5 mm. This adjustment did not change the overall shape of the curves. Also, the intensity of the water

absorption bands and the transmittance were not corrected for sample thickness, so these values should not be considered absolute.

Replacing PbO with BaO does not significantly change the optical transmittance, but it does affect the refractive index. The PGGB glass has a higher refractive index (n = 2.17 at 632 nm) than the BGGB glass (n = 1.98 at 632 nm). This difference is due to the higher electronic polarizability of Pb^{2+} ions compared to Ba^{2+}, which raises the refractive index in heavy metal oxide glasses [32]. Pb^{2+} also makes the glass network less rigid [47], while Ba^{2+} forms stronger bonds with oxygen, resulting in a more rigid structure [33].

When PbO is replaced with BaO, the glass has lower polarizability and higher bond strength and thermal stability [30]. This is also seen in the higher glass transition temperature measured by DSC. These changes do not stop the glass from being a good medium for TGG crystallization. The BGGB glass still has the right chemical properties and optical transparency for crystal growth without using lead.

3.2 Thermal behavior of the bulk glass compositions (DSC)

Differential Scanning Calorimetry (DSC) was used to study the thermal properties of both the undoped base glasses and the Tb-doped compositions. The DSC curves of the undoped PbO-based (PGGB) and BaO-based (BGGB) glasses are shown in Fig. 28.

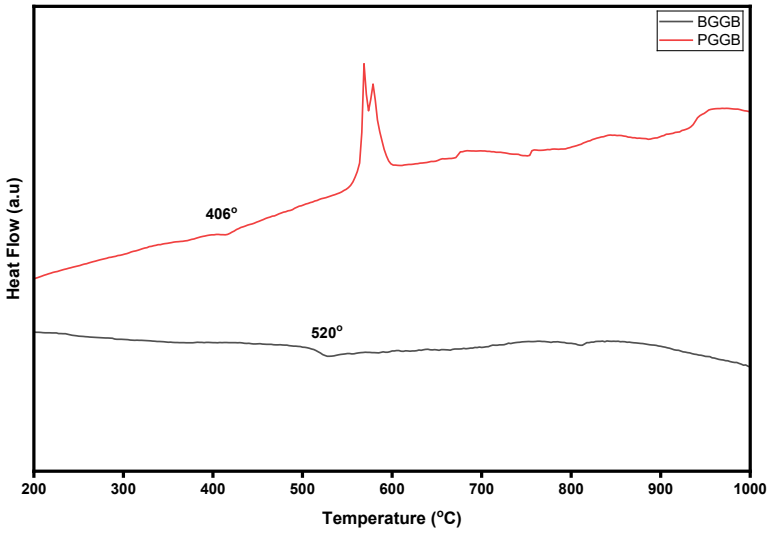

Figure 28. DSC curves of PGGB and BGGB blank glass. Tg values were obtained as the intersection between two tangent dashed lines.

The BaO-based glass shows a higher glass transition temperature (Tg = 520 °C) compared to the PbO-based glass (Tg = 406 °C). This increase in Tg indicates that the glass network becomes more rigid when BaO is introduced [7, 8]. In contrast, the lower Tg of the PbO-based glass suggests a more flexible structure [5,9,10].

For the BGGB composition, no crystallization peaks were observed up to 600 °C. This indicates that the glass remains stable over this temperature range and does not easily undergo crystallization. Such behavior is important for controlling the crystallization process during heat treatment.

3.3 Morphological Analysis

Fig. 29 presents photographs (a), optical microscopy images of TGG crystals embedded in the glass matrix (b), and isolated crystals obtained after acid etching (c) for compositions C1–C5. All samples appeared opaque, which is attributed to light scattering from the embedded crystalline phase. Optical microscopy revealed the presence of well-formed crystals with sizes ranging from approximately 5 to 50 μm across all compositions.

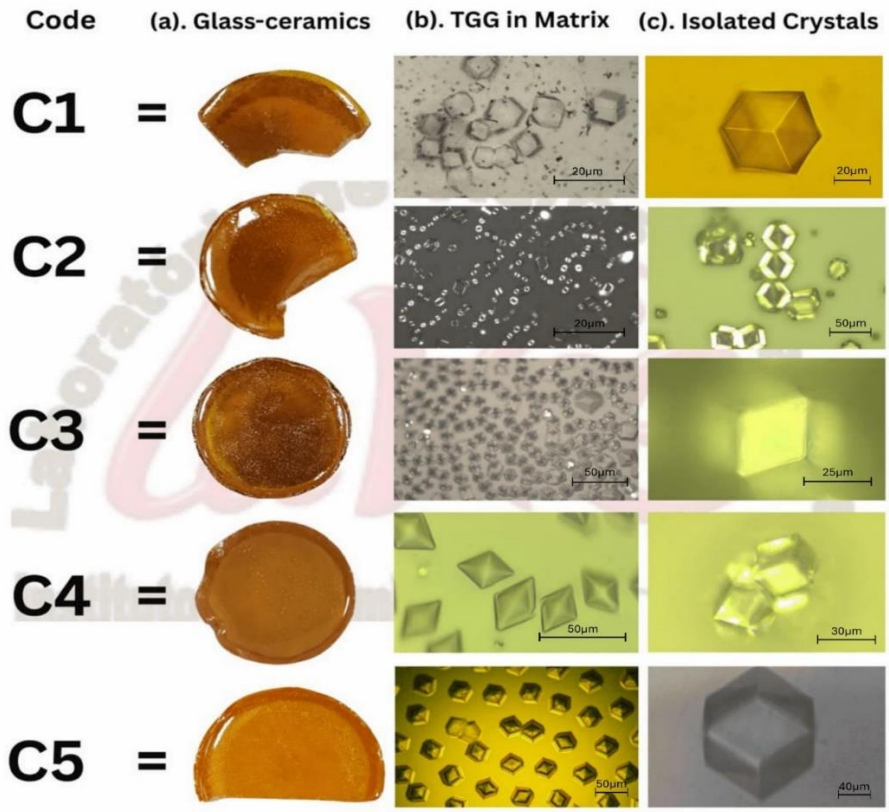

Figure 29. A) Photographs of glass-ceramic (C1-C5) embedded with TGG single-crystals in the matrix.

For the fully Pb-free composition (C5), the crystals exhibited a relatively narrower size distribution and slightly modified crystal compared to PbO-rich compositions. In contrast, PbO-based samples (e.g., C1) displayed a broader size distribution, consistent with faster crystal growth in melts of lower viscosity. These differences are attributed to changes in melt properties associated with PbO substitution by BaO.

After selective chemical dissolution of the glass matrix, the isolated crystals exhibited well-defined cubic morphologies, confirming the formation of quality TGG single-crystals in both PbO- and BaO-containing systems.

3.4 Structural Properties

3.4.1 X-ray Diffraction (XRD) Powder

The XRD patterns of $Tb_3Ga_5O_{12}$ (TGG) crystals obtained from samples C1 to C5 are shown in Fig. 30. All samples present sharp diffraction peaks at 28.9°, 32.3°, 35.5°, 53.3°, and 59.7°. These peaks correspond to the cubic garnet structure with space group Ia-3d and are consistent with standard ICSD cards no. 19178, 20831, and 184934 [11], [12].

In addition to the crystalline peaks, an amorphous halo is observed in all patterns. This indicates that the crystals are formed within a remaining glass matrix. No secondary phases were detected, which confirms that phase-pure TGG was obtained for all compositions.
A comparison between PbO-based and BaO-based samples shows that replacing PbO with BaO does not change the crystal structure. The same garnet phase is formed in all cases. This result shows that BaO can replace PbO without preventing the formation of TGG.

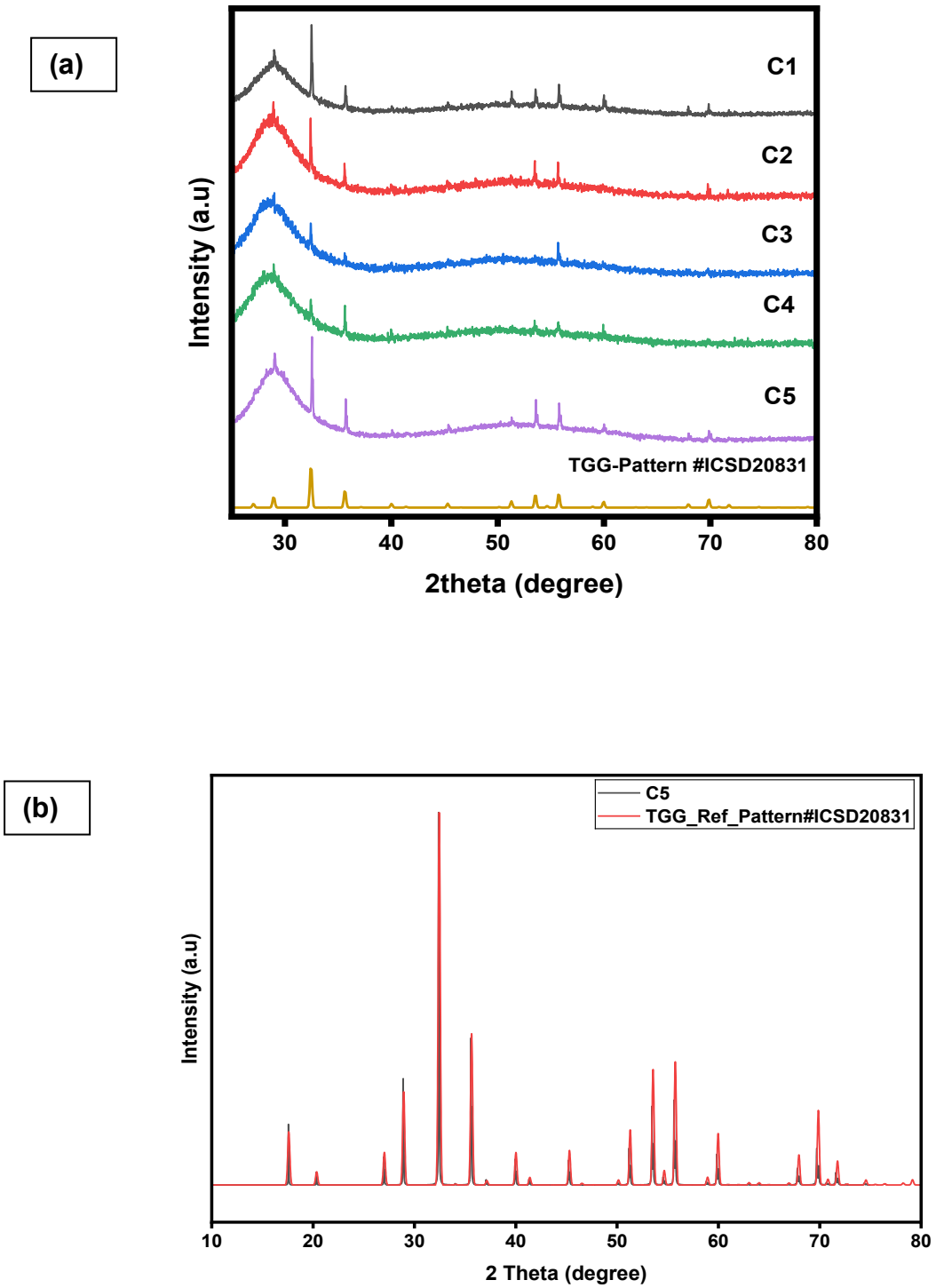

Figure 30. a) XRD Patterns of C1 - C5 powder of glass-ceramics and the TGG reference pattern. b) XRD of isolated single crystals obtained using VESTA software corresponding to the TGG pattern ICSD20831 reference.

Meanwhile, Fig. 31b shows the XRD pattern calculated from the single-crystal CIF file

using VESTA and its comparison with the reference TGG pattern (ICSD 20831). The diffraction peaks are well defined and match the reference pattern, confirming that the isolated crystals correspond to the $Tb_3Ga_5O_{12}$ phase [1]. The peak positions agree with the cubic garnet structure (space group Ia–3d), as also observed in the powder XRD results (Fig. 31a). No additional peaks are detected, indicating the absence of secondary phases. Compared to the powder pattern, the simulated pattern shows sharper and more discrete reflections, as expected for single-crystal data. These results confirm that the isolated crystals extracted from the glass matrix are pure TGG and are consistent with structural data reported for TGG by Orives J. Resges et al., 2025.

3.4.2 X-ray Diffraction (XRD) Single-crystal

Single-crystal X-ray diffraction analysis of the C5 sample confirms that the isolated crystals correspond to $Tb_3Ga_5O_{12}$ (TGG). The structure is cubic with space group Ia-3d, which is expected for lanthanide gallium garnets [36]. The refined lattice parameter (a = 12.3539(3) Å) agrees well with values reported for TGG obtained from both conventional crystal growth and glass-ceramic methods [1,14,15]. The obtained refeinement parameters are resumed in Table 8.

Table 8. - Single-Crystal data and structure refinement details for TGG (C5)

Crystal Data	
Chemical Formula	$Tb_3Ga_5O_{12}$
M_r	1017.36
Chemical System, Space Group	Cubic, *Ia*-3*d* (No. 230)
a = b = c (Å)	12.3539(3)
α = β = γ (°)	90
Unit Cell Volume ($Å^3$)	1885.44(14)
Z	8
Temperature (K)	99.99(10)
Radiation type	Mo Kα (λ = 0.71073 Å)
Absorption coefficient, μ (mm^{-1})	36.316
Crystal Size (mm^3)	0.14 × 0.11 × 0.11
Data Collection	
Diffractometer	XtaLAB Synergy, Dualflex, HyPix
Absorption correction	Gaussian Numerical absorption correction based on gaussian integration over a multifaceted crystal model. Empirical absorption correction using spherical harmonics, implemented in SCALE3 ABSPACK scaling algorithm.
T_{min}, T_{max}	0.062 / 0.126
No of measured, independent and observed [I >2σ(I)] reflections	1740 / 211 / 196
R_{int}	0.0391
(sin θ/λ)max ($Å^{-1}$)	0.675
Refinement	
R[I >2σ(I)], R_1 (all data), wR_2 (all data)	0.0224, 0.0236 0.0603
Goodness-of-fit on F^2	1.297
No of reflections	211
Parameters refined	18
Δρmax, Δρmin (e $Å^{-3}$)	+1.139, −0.851
Completeness (%)	100

The cation distribution follows the standard garnet arrangement, with Tb^{3+} occupying dodecahedral sites and Ga^{3+} distributed between octahedral and tetrahedral sites. This confirms that the crystallization process within the glass matrix leads to the correct long-range ordering required for garnet formation.

The refinement converged with low residuals and full data completeness, indicating good crystallographic quality. No secondary phases or structural distortions were detected. This is an important result, as it shows that the change from PbO to BaO in the glass composition does not introduce detectable defects or structural disorder in the resulting crystals. Therefore, the local chemical environment provided by the BaO-based glass

remains suitable for stabilizing the garnet structure. This supports the idea that the supersaturated glass-melt approach is not limited to PbO-containing systems and can be extended to Pb-free compositions without compromising crystal quality. A structural representation of the garnet crystal packing is shown in Fig. 31, below:

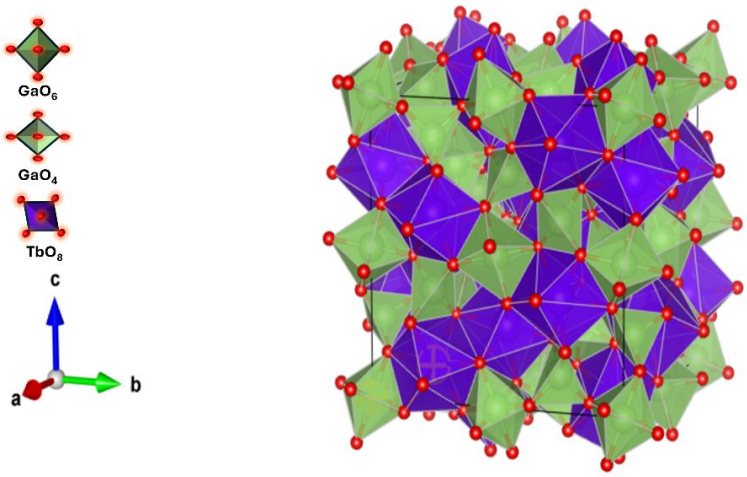

Figure 31. shows the crystal packing of C5-TGG generated with the VESTA software, emphasizing the TbO_8, GaO_6, and GaO_4 structural units.

3.5 Microstructural and chemical analysis (SEM–EDS)

The microstructure of the C5 sample was analysed using scanning electron microscopy (SEM), as shown in Fig. 32a. The image shows TGG crystals embedded in the BaO-based glass matrix. The crystals have a well-defined cubic shape and their size ranges between 10 and 50 μm. They are distributed throughout the matrix in a similar way to what is observed in PbO-based systems [1]. However, in the BaO-based sample, the crystal size distribution appears more uniform, suggesting that BaO helps to better control crystal growth during heat treatment.

The elemental distribution obtained from EDS mapping (Fig. 33b) confirms the composition of both the crystals and the surrounding glass. The crystals mainly contain Tb, Ga, and O, which is consistent with the expected composition of $Tb_3Ga_5O_{12}$. The glass matrix, on the other hand, contains Ba, Ge, and Bi, and these elements are not incorporated into the crystal structure.

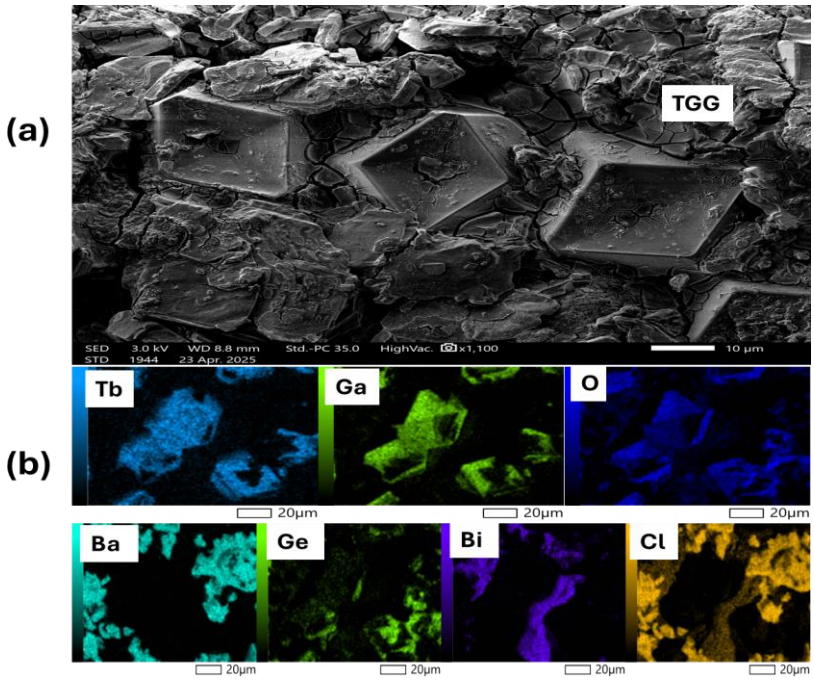

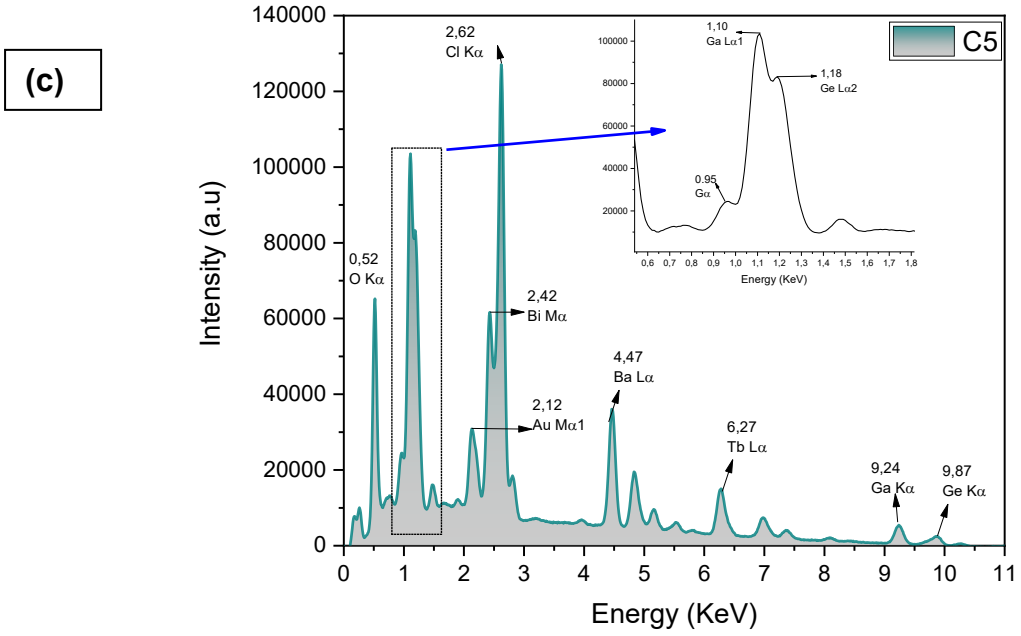

Figure 32. SEM-EDS analysis a) SEM image of C5 b) elemental mapping of C5 and c) EDS spectra of C5.

Although Ge and Ga have similar atomic numbers and overlapping signals, the mapping clearly shows that Ga is located in the crystalline regions, while Ge remains in the

glass matrix. This helps to distinguish their roles in the system.

The EDS spectra further confirm these results. Tb is identified by peaks at 1.24 keV (Ec(M5)), 6.27 keV ($L\alpha_1$), 6.97 keV ($L\beta_1$), and 7.36 keV ($L\beta_2$). Ga shows peaks at 0.95 keV (L_1) and 1.098 keV ($L\alpha_1$), while oxygen appears at 0.5 keV (Kα). In the glass matrix, Ba is detected at 1.0 keV (M_r), 4.3 keV (Lα), 4.7 keV (Lα), and 5.2 keV ($L\beta_2$). Ge appears at 1.19 keV ($L\alpha_1$), and Bi at 2.42 keV ($M\alpha_{1,2}$). A small Cl signal at 1.84 keV is also observed. This does not come from the glass itself but is related to the use of HCl during sample preparation to remove the glass matrix.

Importantly, the acid treatment did not change the crystal shape or composition. The cubic morphology is preserved, and the elemental composition remains consistent. These results confirm that stoichiometric TGG crystals are successfully formed within the BaO-based glass, with a clear separation between the crystalline phase and the glass phase.

3.6 Vibrational Spectroscopy

3.6.1 Raman Spectroscopy

The Raman spectra (Fig. 33) indicate the formation of the TGG phase in the BaO-containing samples (C1–C5), with characteristic bands around 350 cm^{-1} and 580 cm^{-1} corresponding to Ga–O and Tb–O vibrations [1]. The presence of these modes indicates that the local bonding environment is consistent with the garnet structure [14,16–19].

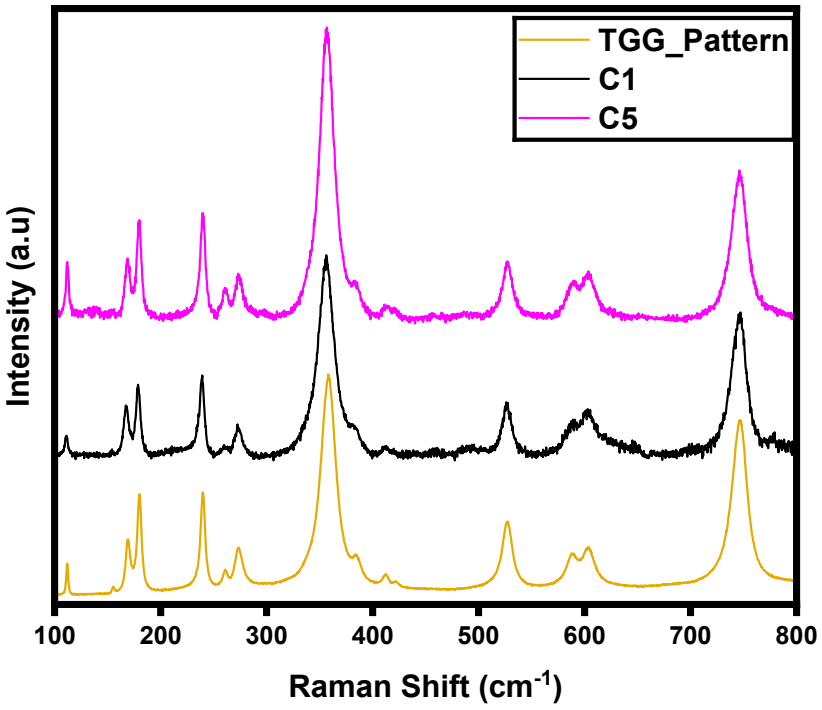

Figure 33(a). Raman spectra for C1, C5, and TGG commercial patterns.

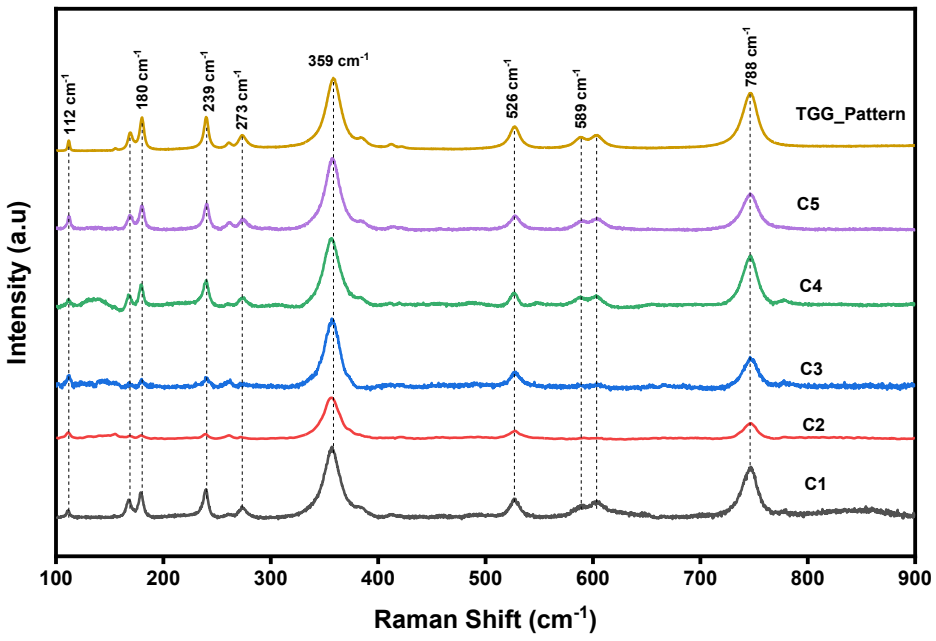

Figure 33(b). Stacked Raman spectra of the C1–C5 glass-ceramic samples compared with

the commercial TGG reference pattern, showing the evolution of the vibrational bands associated with the garnet structure.

The stacked spectra (Fig. 33b) show that the C1 and C5 samples exhibit the closest agreement with the commercial TGG reference pattern, particularly in the main bands located around 359 , 526 , and 788 cm^{-1}. These results indicate that the garnet structure is more clearly developed in these compositions. The intermediate compositions also exhibit bands associated with TGG formation, although with broader features and lower spectral resolution, suggesting differences in crystallinity and local structural ordering across the series.

The good agreement with the commercial TGG reference [20] further supports the formation of the garnet phase in the BaO-containing system. The Raman results also confirm that the short-range structural order is preserved after modifying the glass composition. This behavior is consistent with the XRD results and indicates that replacing PbO with BaO does not suppress TGG formation, but instead influences the crystallization behavior and structural organization of the resulting phases.

3.6.2 FTIR Spectroscopy

The FTIR spectra of TGG single crystals obtained from compositions C1 and C5 are shown in Fig. 34. The observed absorption bands are associated with lattice vibrations of $Tb_3Ga_5O_{12}$. The main features in the 500–800 cm^{-1} region correspond to Tb–O and Ga–O stretching modes, which are characteristic of the garnet structure [21], [22]. These vibrations are consistent with the framework of interconnected tetrahedral and octahedral units reported for rare-earth gallium garnets [21], [23].

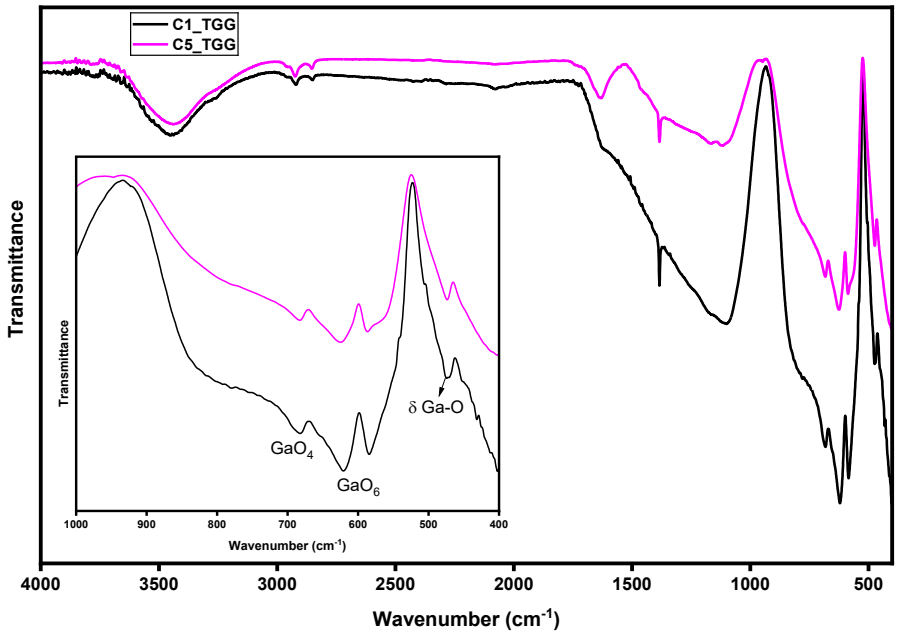

Figure 34. FTIR spectra of C1 and C5 TGG single-crystals.

A band around 473 cm^{-1} can be associated with Tb–O vibrations related to Tb^{3+} ions in dodecahedral coordination. The relatively low wavenumber of this band is consistent with the high atomic mass of terbium [22]. This confirms that Tb occupies the correct crystallographic sites within the garnet structure. The main absorptions from the GaO_6 and GaO_4 polyhedra can be observed in the range of 500-700 and 700-800 cm^{-1}, respectively. Additional bands observed at higher wavenumbers are not related to the intrinsic crystal structure. The broad band near 3440 cm^{-1} and the weaker band around 1637 cm^{-1} are attributed to O–H stretching and H–O–H bending vibrations, respectively [24]. These features are likely due to surface hydroxyl groups introduced during sample preparation and do not reflect the bulk structure of the crystals. A weak feature near 1385 cm^{-1} may be associated with asymmetric stretching of residual carbonate species or traces of remaining glass components after the etching process [29].

Both C1 and C5 compositions show very similar spectral features, indicating that the local bonding environment remains unchanged after replacing PbO with BaO. This suggests that the substitution does not affect the short-range order of the garnet structure. The small differences in band intensity may be related to variations in residual glass content or slight differences in thermal treatment conditions, rather than any structural modification. The FTIR results support the formation of the TGG garnet phase in the investigated glass system.

3.7 Optical measurements of TGG crystals

The optical transmission spectra of TGG crystals obtained from compositions C1–C5 are presented in Fig. 35. The measurements were performed over the 400–2400 nm range, which is relevant for photonic and magneto-optical applications.

Among the samples, C2 shows the highest transmittance, reaching values close to 80% in the visible and near-infrared regions. Samples C1 and C5 also exhibit good transparency, although their transmittance is slightly lower. These differences are not likely due to changes in the crystal structure, but rather to variations in microstructure, such as crystal size distribution, volume fraction of the crystalline phase, and light scattering within the glass-ceramic matrix.

A clear absorption band is observed around 487 nm in all compositions. This band is associated with the $^{7}F_{6} - {}^{5}D_{4}$ electronic transition of Tb^{3+} ions and is characteristic of terbium-containing garnets [21,22,25]. The presence of this transition confirms that Tb^{3+} ions are incorporated into the garnet structure and retain their optical activity.

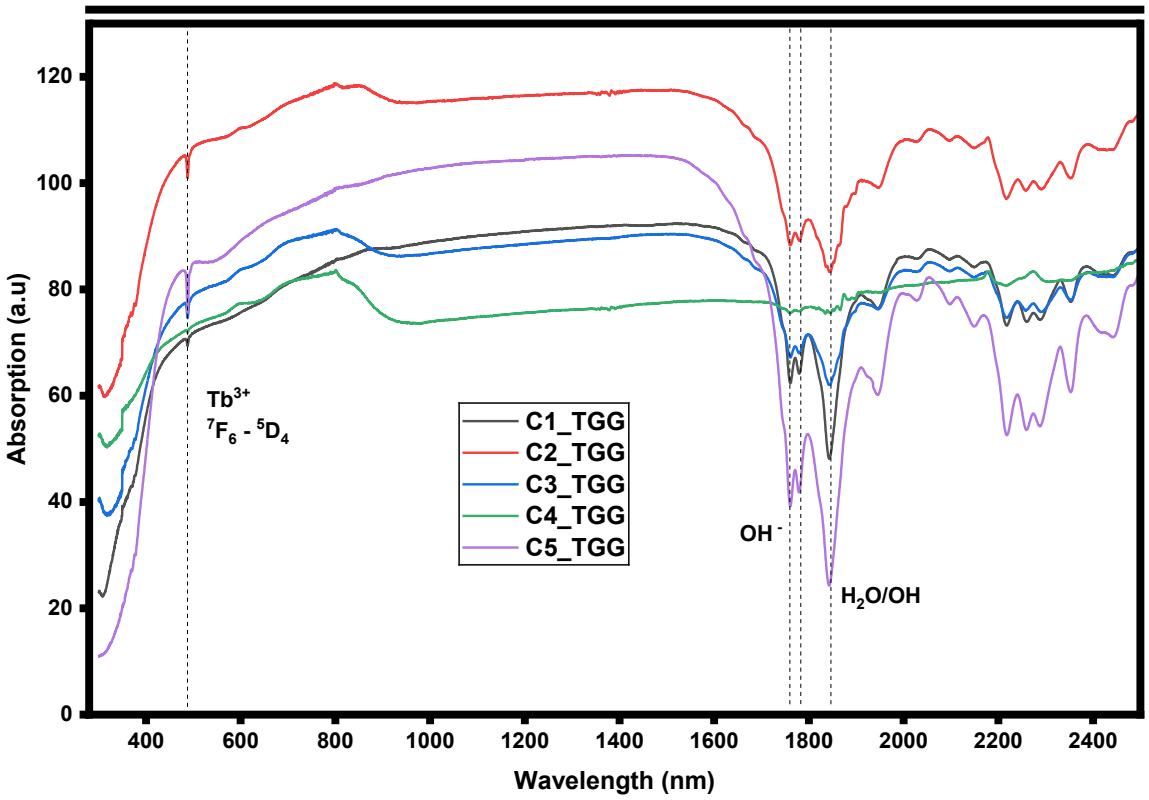

Figure 35. The optical transmission spectra of C1 - C5 TGG single crystals

Additional absorption features are observed in the near-infrared region between approximately 1500 and 2000 nm. The bands centered near 1760–1800 nm and 1840–1950 nm are mainly attributed to hydroxyl (OH^-) and molecular water-related vibrational overtones and combination bands commonly present in oxide glasses and glass-ceramic systems [45]. These absorptions are associated with residual hydroxyl groups incorporated during sample preparation or with adsorbed atmospheric moisture. Similar infrared absorption behavior has been reported for terbium-containing photonic glasses and magneto-optical oxide systems [45].

The overall transmission behavior suggests that the BaO-based glass-ceramic system can produce TGG crystals with good optical quality. However, the variation in transmittance between samples indicates that processing conditions play an important role in controlling optical losses. In particular, scattering from crystals and residual glass phases appears to be a limiting factor. Therefore, further optimization of heat treatment and composition may be required to improve optical performance. The results show that replacing PbO with BaO does not degrade the optical properties of TGG crystals, and the resulting transparency is suitable for magneto-optical applications.

3.8 Thermal Behavior of TGG glass-ceramics

The DSC curves of the glass-ceramic samples containing TGG crystals (C1–C5) are presented in Fig. 36. A progressive increase in the glass transition temperature (Tg) is observed from C1 to C5, with values of 365 °C, 370 °C, 450 °C, 467 °C and 486 °C, respectively. This evolution follows the gradual substitution of PbO by BaO. This increase in Tg reflects changes in the remaining residual glass network. As BaO content increases, the structure becomes more rigid, which is typically associated with stronger bonding and higher melt viscosity. In contrast, PbO-rich compositions show lower Tg values, indicating a more flexible network. This behaviour is in line with trends reported for similar oxide glass systems [3, 8].

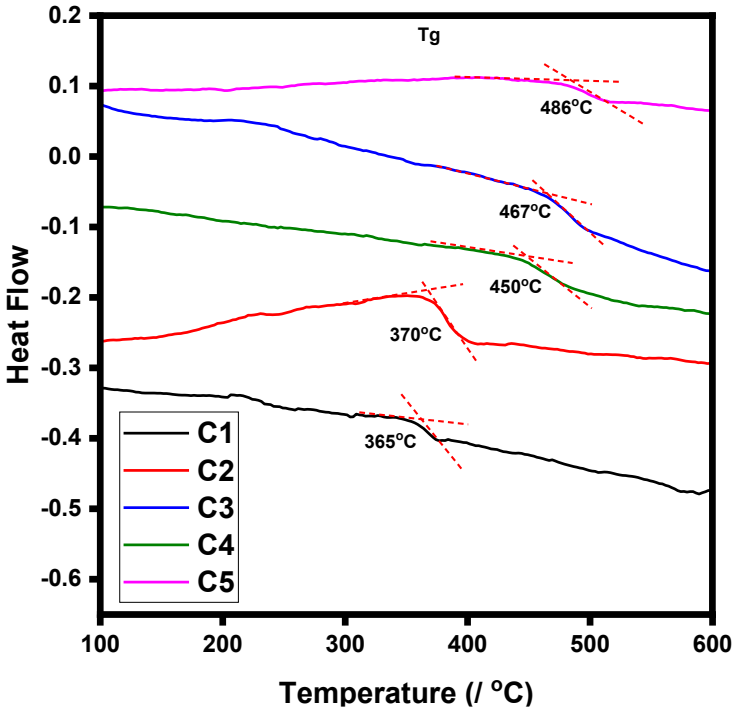

Figure 36. DSC curves of C1 - C5. Tg values were obtained at the intersection between two tangent dashed lines.

The shift in Tg also has implications for crystallization. A higher Tg usually means that more energy is required to activate atomic mobility, which can slow down the onset of crystallization. At the same time, the increased rigidity can help limit uncontrolled crystal growth, making the process easier to manage during heat treatment. The DSC curves suggest that, even with these changes, the temperature range available for controlled crystallization remains accessible across all compositions.

The difference in Tg between the C5 glass-ceramic and the undoped BGGB glass is linked to the presence of the crystalline phase. In C5, part of the gallium and terbium has already been consumed to form TGG crystals. This reduces their contribution to the glass network and changes the composition of the remaining amorphous phase, which in turn affects the Tg value. These observations show that replacing PbO with BaO modifies the thermal behaviour in a predictable way, without disrupting the conditions required for TGG crystallization.

3.9 Magnetic Properties of TGG Single-crystals

The impact of substituting PbO with BaO on the magnetic performance of the crystallized phase was assessed through magnetic characterization of the C5-TGG sample. These results were compared with previously reported data for TGG crystals grown in PbO-based glass matrices to determine whether the magnetic nature of the Tb^{+3} ions remains consistent across different glass modifiers [1], [26]. Magnetic susceptibility measurements were conducted from 2 K to 300 K under an applied field of 100 Oe. Figure 37 presents the results, which were fitted using the Curie-Weiss law [27]:

$$X_m = \frac{C}{T-\theta} - X_0 \quad (1) \qquad \text{(Eq. 13)}$$

In this context, C denotes the Curie constant, θ represents the paramagnetic Curie-Weiss temperature, and X_0 is a temperature-independent term associated with the diamagnetic contribution to the measurement. The inset of Figure 37 displays the inverse molar susceptibility $(1/X_m)$ as a function of temperature. The observed linear behavior confirms that the magnetic response is accurately described by the Curie-Weiss model.

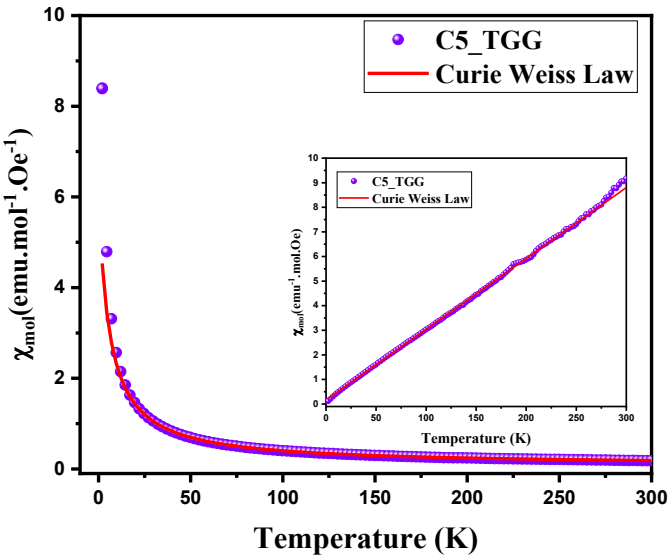

Figure 37. χm vs T curves for C5-TGG; the inset shows the 1/χm curves, where the solid red line represents the fit to the Curie-Weiss law. Inset: Inverse molar susceptibility $(1/X_m)$ as a function of temperature

The Weiss temperature was determined to be θ = -5.78 K, indicating weak antiferromagnetic interactions between the Tb^{+3} ions [9],[28]. The Curie constant, obtained from the slope of the linear fit, was C = 34.73 emu·K·mol^{-1}. Based on this value, the effective magnetic moment (μ_{eff}) was calculated using the following equation:

$$\mu_{eff} = \sqrt{\frac{8C}{n}}\mu_B \quad (2) \qquad \text{(Eq. 14)}$$

The effective magnetic moment (μ_{eff}) was calculated to be 9.62μ_B, which closely matches the theoretical free-ion value of 9.72 μ_B for the Tb^{+3} ion. These findings are consistent with results obtained for TGG systems synthesized using PbO-based precursor glasses [9],[26], indicating that substituting PbO with BaO does not affect the local electronic configuration or the magnetic moment of the terbium ions in the crystallized TGG phase.

The influence of an external magnetic field at constant temperatures was investigated for the C5-TGG sample, as illustrated in Figure 38a (2 K) and Figure 39b (300 K). At 2 K, the sample does not exhibit a hysteresis loop, as the magnetic response arises from localized 4f electrons of Tb^{+3} ions and saturates above 60 kOe. At 300 K, the material displays characteristic paramagnetic behavior. The low-temperature magnetization data were fitted using the Brillouin function.

$$M = NgJ\mu_b B_{j(x)} \quad (3) \qquad \text{(Eq. 15)}$$

$$B_{j(x)} = \left[\frac{2J+1}{J}\right] coth\left[\frac{(2J+1)x}{J}\right] - \left[\frac{1}{2J}\right] coth\left[\frac{x}{2J}\right] \quad (4) \qquad \text{(Eq. 16)}$$

$$x = \frac{Jg\mu_b}{K_b(T+T_0)} \quad (5) \qquad \text{(Eq. 17)}$$

In this equation, M represents the magnetization, N is the number of ions, g is the Landé factor, and J is the total angular momentum. For the Tb^{+3} ions in the C5-TGG crystal, values of g = 1.5 and J = 6 were used for the refinement.

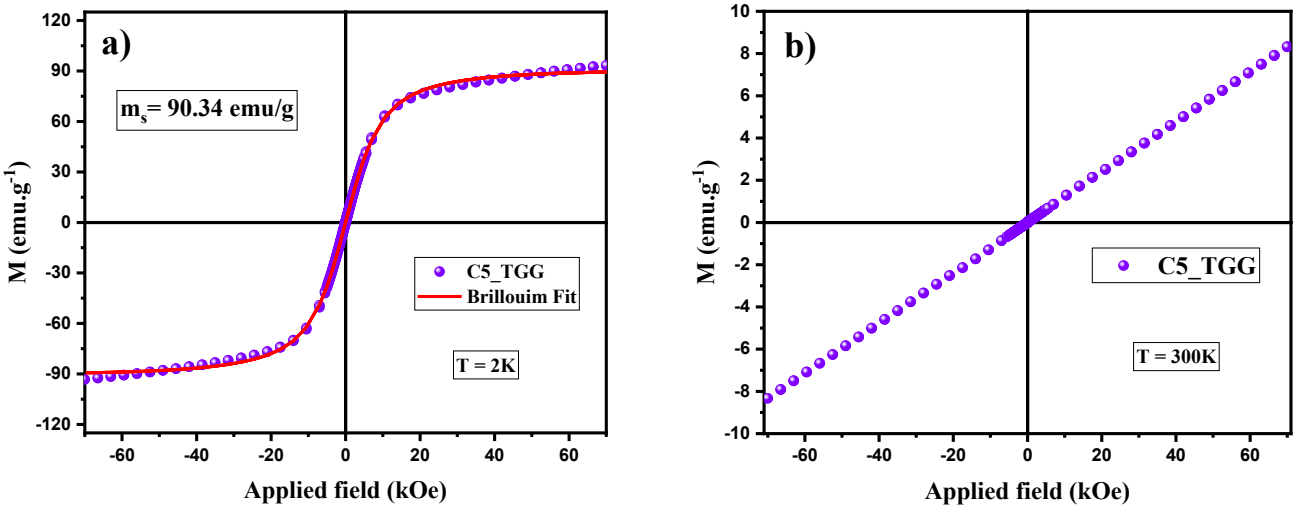

Figure 38. Magnetization as a function of the applied magnetic field (M vs H) of the C5-TGG is shown for (a) and (b) at 2K and 300K, respectively.

In Figure 38a, the solid red line represents the fit, which aligns with the experimental data. These results are consistent with studies involving PbO glass matrices, with C5-TGG exhibiting a saturation magnetization of Ms = 90.34 emu/g at 2 K. The magnetic performance is comparable to that of PbO-based systems [1], indicating that substituting PbO with BaO does not alter the fundamental magnetic properties of TGG crystals.

3.9 Conclusion – TGG System

This study demonstrates the successful synthesis of micrometer-sized $Tb_3Ga_5O_{12}$ (TGG) single crystals in Pb-free BaO-based heavy metal oxide glass using a supersaturated glass-melt approach. A systematic replacement of PbO by BaO was achieved without disrupting the crystallization of the cubic garnet phase, yielding well-defined TGG single crystals with sizes ranging from 5 to 50 µm. Structural characterization by powder and single-crystal X-ray diffraction confirmed the formation of phase-pure cubic TGG with lattice parameters consistent with literature values. Raman and FTIR spectroscopy further verified the preservation of the garnet structure, while SEM–EDS mapping demonstrated the clear separation between the crystalline phase (Tb, Ga, O) and the surrounding glass matrix (Ba, Ge, Bi). Optical transmission measurements revealed good transparency in the visible and near-infrared regions, confirming the optical suitability of the crystals for photonic applications.

Thermal analysis indicated that substitution of PbO with BaO increases the glass transition temperature and enhances thermal stability, while maintaining a crystallization window suitable for controlled TGG crystal growth. Magnetic characterization of the Pb-free composition (C5) revealed paramagnetic behavior consistent with Tb^{3+} ions. Curie–Weiss analysis yielded an effective magnetic moment ($\mu_{eff} \approx 9.62\ \mu B$), in close agreement with the theoretical value for Tb^{3+}, and a small negative Weiss temperature ($\theta \approx -5.78$ K), indicating weak antiferromagnetic interactions. Magnetization measurements further confirmed the expected paramagnetic response with no hysteresis.

These results demonstrate that BaO-based glass-ceramic systems provide a viable Pb-free alternative for the synthesis of TGG crystals while preserving their structural, optical, and magnetic properties. The approach offers a scalable and environmentally safer pathway for producing TGG crystals that may serve as seeds for conventional melt-growth methods such as the Czochralski process, enabling sustainable production of magneto-optical materials.

References

[1] J. R. Orives *et al.*, “A supersaturated glass-melt approach for growing micrometer-sized TGG single crystals,” *Ceram. Int.*, 2025, doi: 10.1016/j.ceramint.2025.08.137.

[2] H. An, P. Qian, Y. Ye, and S. Wang, “Structural and magneto-optical properties of PbO–Bi2O3–B2O3–Al(PO3)3 glasses,” *J. Non. Cryst. Solids*, vol. 538, Jun. 2020, doi: 10.1016/j.jnoncrysol.2020.120021.

[3] J. Bhemarajam, P. S. Prasad, M. M. Babu, M. Özcan, and M. Prasad, “Investigations on structural and optical properties of various modifier oxides (Mo = zno, cdo, bao, and pbo) containing bismuth borate lithium glasses,” *Journal of Composites Science*, vol. 5, no. 12, Dec. 2021, doi: 10.3390/jcs5120308.

[4] T. Guérineau *et al.*, “Toward low-loss mid-infrared Ga2O3–BaO–GeO2 optical fibers,” *Sci. Rep.*, vol. 13, no. 1, Dec. 2023, doi: 10.1038/s41598-023-30522-1.

[5] A. E. Souza *et al.*, “Heavy metal oxide glass-ceramics containing luminescent gallium-garnets single crystals for photonic applications,” *J. Alloys Compd.*, vol. 864, May 2021, doi: 10.1016/j.jallcom.2021.158804.

[6] I. Saber *et al.*, “Synthesis and characterization of new eco-friendly vitreous system Bi2O3–B2O3–BaO: Structural, morphologic, and thermal analysis,” *Opt. Mater. (Amst).*, vol. 149, Mar. 2024, doi: 10.1016/j.optmat.2024.115079.

[7] A. Ardiansyah *et al.*, “Physical, mechanical, optical, and gamma radiation shielding properties of the BaO-based glass system prepared by the melt-quench technique: A review,” Sep. 01, 2023, *Elsevier Ltd*. doi: 10.1016/j.radphyschem.2023.111059.

[8] R. Mishra *et al.*, “Structural, thermo-mechanical, optical and gamma-ray shielding properties of lead-free BaO–ZnO–B2O3–SiO2 and lead-based PbO–Bi2O3–K2O–SiO2 glasses,” *Ceram. Int.*, vol. 50, no. 20, pp. 38495–38506, Oct. 2024, doi: 10.1016/j.ceramint.2024.07.214.

[9] J. H. Song, J. Heo, and S. H. Park, “Emission properties of PbO-Bi2O3-Ga2O3-GeO2 glasses doped with Tm3+ and Ho3+,” *J. Appl. Phys.*, vol. 93, no. 12, pp. 9441–9445, Jun. 2003, doi: 10.1063/1.1571968.

[10] Y. S. Han, J. H. Song, and J. Heo, “Analysis of cross relaxation between Tm3+ ions in PbO-Bi 2O3-Ga2O3-GeO2 glass,” *J. Appl. Phys.*, vol. 94, no. 5, pp. 2817–2820, Sep. 2003, doi: 10.1063/1.1595148.

[11] R. Wawrzyńczak *et al.*, “Magnetic order and single-ion anisotropy in Tb3Ga5 O12,” *Phys. Rev. B*, vol. 100, no. 9, Sep. 2019, doi: 10.1103/PhysRevB.100.094442.

[12] C. P. Reshmi, S. Savitha Pillai, K. G. Suresh, and M. R. Varma, “Magnetic and magnetocaloric properties of Gd 3-xTb xGa 5O 12 (x=0, 1, 2, 3) garnets,” *J. Magn. Magn. Mater.*, vol. 324, no. 12, pp. 1962–1966, Jun. 2012, doi: 10.1016/j.jmmm.2012.01.030.

[13] P. Mukherjee and S. E. Dutton, “Enhanced Magnetocaloric Effect from Cr Substitution in Ising Lanthanide Gallium Garnets Ln3CrGa4O12 (Ln = Tb, Dy, Ho),” *Adv. Funct. Mater.*, vol. 27, no. 32, Aug. 2017, doi: 10.1002/adfm.201701950.

[14] M. Watanabe *et al.*, “Czochralski growth and composition control of Tb3Ga5O12 single crystals,” *J. Cryst. Growth*, vol. 665, Sep. 2025, doi: 10.1016/j.jcrysgro.2025.128205.

[15] M. Watanabe, Y. Anzai, and I. Tanaka, “Characterization of defects in Tb3Ga5O12 single crystals grown by the Czochralski method,” *J. Cryst. Growth*, vol. 634, May 2024, doi: 10.1016/j.jcrysgro.2024.127687.

[16] L. V. Albino *et al.*, “Innovative synthesis of Tm^{3+}/Er^{3+}-doped Yb-YGG single crystals for upconversion-based white light emission,” *Ceram. Int.*, vol. 51, no. 12, pp. 16700–16709, May 2025, doi: 10.1016/j.ceramint.2024.11.480.

[17] M. Nalin *et al.*, “Novel scalable synthesis of luminescent and magnetic single crystal garnets,” *Mater. Horiz.*, Apr. 2025, doi: 10.1039/d5mh00254k.

[18] W. Jin *et al.*, “Growth and performance research of $Tb_3Ga_5O_{12}$ magneto-optical crystal,” *J. Cryst. Growth*, vol. 484, pp. 17–20, Feb. 2018, doi: 10.1016/j.jcrysgro.2017.12.024.

[19] W. Jin *et al.*, “Fabrication and magneto-optical properties of TGG transparent ceramics,” *Physica B Condens. Matter*, vol. 555, pp. 96–98, Feb. 2019, doi: 10.1016/j.physb.2018.11.053.

[20] X. Zhao *et al.*, “High Verdet Constant Glass for Magnetic Field Sensors High Verdet Constant Glass for Magnetic Field Sensor,” *ACS Appl. Mater. Interfaces*, vol. 2022, no. 51, doi: 10.1021/ac.

[21] X. Li *et al.*, “Fabrication and characterizations of highly transparent Tb3Ga5O12 magneto-optical ceramics,” *Opt. Mater. (Amst).*, vol. 88, pp. 238–243, Feb. 2019, doi: 10.1016/j.optmat.2018.11.048.

[22] X. Li *et al.*, “Transparent $Tb_3Ga_5O_{12}$ magneto-optical ceramics sintered from co-precipitated nano-powders calcined at different temperatures,” *Opt. Mater. (Amst).*, vol. 90, pp. 26–32, Apr. 2019, doi: 10.1016/j.optmat.2019.02.009.

[23] V. I. Nizhankovskiy, “Temperature evolution of optical transition $^7F_6 \Rightarrow {}^5D_4$ in $Tb_3Ga_5O_{12}$ and $Tb_2(MoO_4)_3$ from 4.2 to 300 K,” *J. Alloys Compd.*, vol. 903, May 2022, doi: 10.1016/j.jallcom.2022.163880.

[24] K. Papagelis *et al.*, “Vibrational properties of $(Gd_{1-x}Y_x)_3Ga_5O_{12}$ solid solutions,” *J. Appl. Phys.*, vol. 107, no. 11, Jun. 2010, doi: 10.1063/1.3393259.

[25] Z. Chen, L. Yang, X. Wang, J. Wang, and Y. Hang, “Highly transparent terbium gallium garnet crystal fabricated by the floating zone method for visible-infrared optical isolators,” *Opt. Mater. (Amst).*, vol. 46, pp. 12–15, Aug. 2015, doi: 10.1016/j.optmat.2015.03.034.

[26] D. F. Franco *et al.*, “Fundamental studies of magneto-optical borogermanate glasses and derived optical fibers containing Tb^{3+},” *Journal of Materials Research and Technology*, vol. 11, pp. 312–327, Mar. 2021, doi: 10.1016/j.jmrt.2021.01.010.

[27] S. Mugiraneza and A. M. Hallas, “Tutorial: a beginner’s guide to interpreting magnetic susceptibility data with the Curie-Weiss law,” Dec. 01, 2022, *Nature Research*. doi: 10.1038/s42005-022-00853-y.

[28] X. Y. Wang *et al.*, “Optical, magnetic susceptibilities and magneto-optical properties of neodymium doped $Tb_3Ga_5O_{12}$ with meliorated properties for near-infrared optical isolators,” *J. Alloys Compd.*, vol. 649, pp. 1085–1088, Aug. 2015, doi: 10.1016/j.jallcom.2015.07.168.

[29] Q. Chen *et al.*, “A new strategy to fabricate YIG ferrite joint with novel magnetic Bi_2O_3-CoO-Fe_2O_3-B_2O_3 glass,” *Mater. Des.*, vol. 215, Mar. 2022, doi: 10.1016/j.matdes.2022.110521.

CHAPTER 4 - RESULTS AND DISCUSSION

4. RESULTS AND DISCUSSION - YIG SINGLE CRYSTALS

Building on the successful validation of the BaO-based supersaturated glass-melt route using the TGG system discussed in Chapter 3 of this project, this section focuses on the synthesis and crystallization of yttrium iron garnet ($Y_3Fe_5O_{12}$, YIG) in PbO-GeO_2-Bi_2O_3-Fe_2O_3-Y_2O_3, BaO-GeO_2-Bi_2O_3-Fe_2O_3-Y_2O_3, and PbO-BaO-GeO_2-Bi_2O_3-Fe_2O_3-Y_2O_3 glass systems. The results demonstrate that specific glass compositions across the three glass systems highlighted above can promote the controlled crystallization of YIG single crystals during cooling. This crystallization behavior is highly dependent on the interplay between glass composition and thermal treatment, indicating that YIG formation is governed by well-defined thermodynamic and kinetic conditions rather than occurring randomly.

A critical factor in this process is the incorporation of Y_2O_3 and Fe_2O_3 into the glass network. In the absence of Y_2O_3, the base compositions remain fully amorphous (fig. 28, chapter 3), forming transparent glasses without any evidence of crystallization [1], [2]. However, when Ga_2O_3 is replaced by Fe_2O_3 and Y_2O_3 is introduced, the system provides the necessary chemical environment for the nucleation and growth of the garnet phase. This highlights the importance of achieving the appropriate Y–Fe stoichiometric balance required for YIG formation [3]. These observations confirm that both compositional design and thermal processing must be carefully controlled to obtain phase-pure YIG crystals within glass-ceramic matrices. The following sections present a detailed analysis of the structural, microstructural, spectroscopic, and magnetic properties of the YIG crystals formed under these conditions.

4.1 X-ray Diffraction

The X-ray diffraction (XRD) patterns of the glass-ceramics prepared in both systems are shown in Fig. 39. For the BaO-based compositions (Ba-YIG1 to Ba-YIG5) and the PB-YIG5% sample, the diffraction peaks match well with the reference pattern of $Y_3Fe_5O_{12}$ (YIG) [4]. This indicates that the garnet phase is successfully formed within the glass matrix. Among these samples, Ba-YIG1 shows a few weak additional peaks, which may be related to small amounts of secondary phases, possibly intermediate iron oxides. The other BaO-based

compositions present clearer and more defined peaks corresponding to the cubic YIG structure, including reflections such as (420), (422), (521), and (444), as shown in Fig. 40.

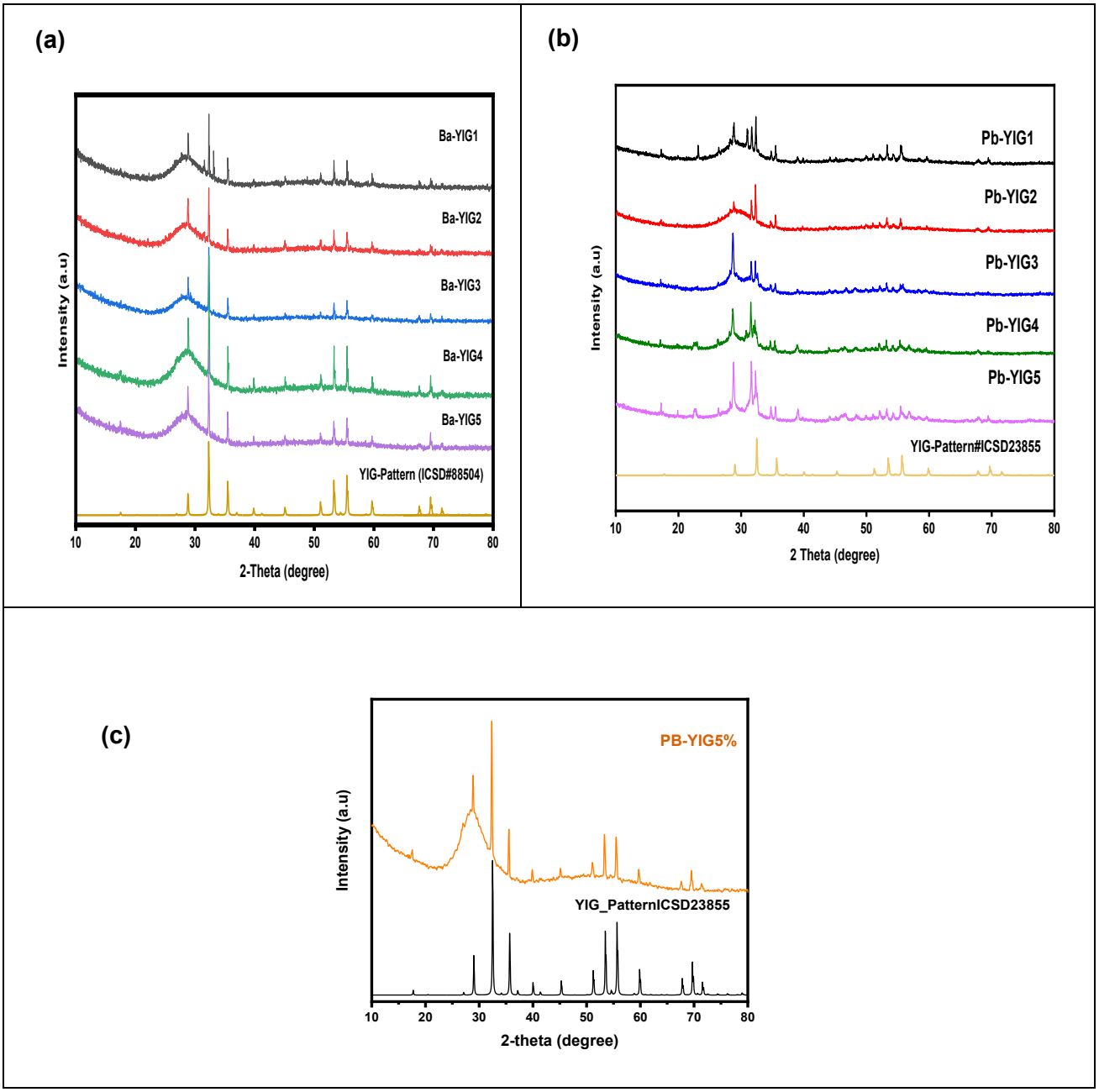

Figure 39. *XRD patterns of (a) BaO-based, (b) PbO-based, and (c) Pb–Ba mixed samples compared with the YIG reference pattern.*

In the PbO-based samples, especially Pb-YIG2, the diffraction pattern shows that YIG is the main crystalline phase, as several peaks match the YIG reference pattern. Still, there are extra peaks that do not fit the garnet structure. For Pb-YIG2, additional features appear at 23.2°, 39.9°, 50.0°, 52.1°, 54.3°, and 67.9° 2θ. Some of these matches reported positions for iron-containing secondary phases, close to reflections reported for α-Fe_2O_3 (JCPDS 33-0664) and $BiFeO_3$ (JCPDS 71-2494). [5], [6], [7], [8]. This suggests that the PbO-based system leads to a more complex crystallization process than the BaO-based system. Because a full multiphase Rietveld refinement was not done, these secondary phases cannot be confirmed. The most reliable conclusion is that YIG is the main phase, but other crystalline phases are also present, and phase selectivity is lower in the PbO-based glass-ceramic. This is supported by the higher χ^2 and visible residuals seen for Pb-YIG2 in the Rietveld refinement.

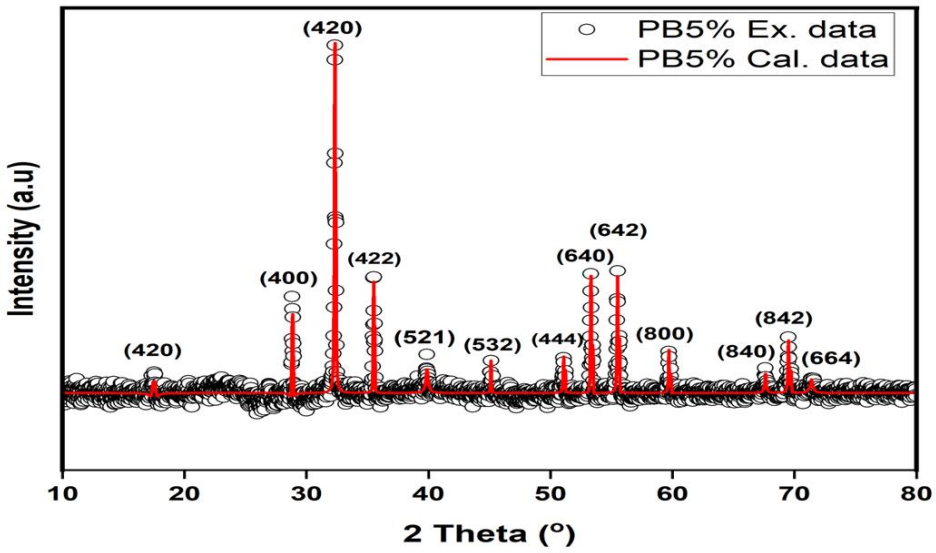

Figure 40. *Structural Deconvolution for PB-YIG5%*

In both systems, a broad halo is observed between 20° and 35° (2θ), which comes from the remaining amorphous glass phase [9, 10]. The presence of both sharp diffraction peaks and this amorphous background confirms that crystallization occurs within a glassy matrix, rather than in a fully crystalline material.

4.1.1 Phase Identification and Rietveld Refinement Analysis

Phase identification was carried out using the QualX2.0 software with the POW_COD database (Altomare et al., 2015). The analysis of the diffraction data, shown in Fig. 41, confirms the phases present in the samples.

For example, the diffraction pattern of Ba-YIG4 (blue line) shows good agreement with the reference pattern of $Y_3Fe_5O_{12}$ (PDF# 00-100-8628, purple line). The alignment of the main peaks confirms that YIG has crystallized within the glass matrix. The background signal remains broad, as expected due to residual glass.

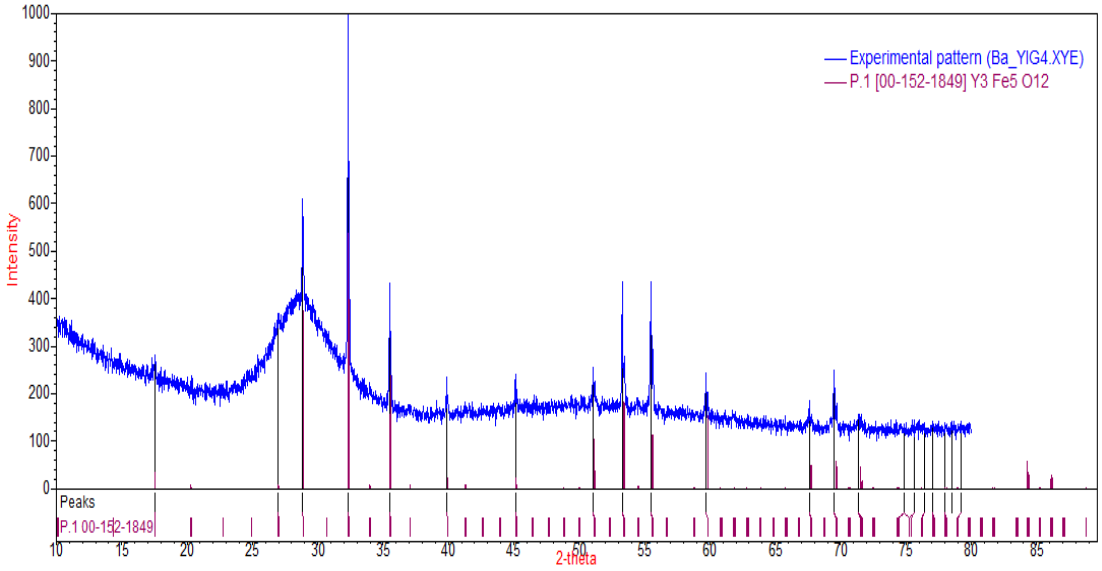

Figure 41. *Phase identification of the Ba-YIG4 sample*

Rietveld refinement was performed on selected samples from both systems, including Ba-YIG5, Pb-YIG2, and PB-YIG5%. The refinement was carried out using the FullProf software, based on the cubic $Y_3Fe_5O_{12}$structure (space group Ia-3d, CIF Nº. 1533341). The refinement profiles are presented in Fig. 42, and the corresponding parameters are listed in Table 9.

Table 9. - Lattice Parameters and Refinement Data

						Goodness of Fit			
S/N	**Samples**	**a**	**b**	**c**	**α,β,Υ**	X^2	**Rwp**	**Rexp**	**Rp**
1	Ba-YIG5	12.3872	12.3872	12.3872	90	4.99	56.0	24.98	174
2	Pb-YIG2	12.4022	12.4022	12.4022	90	8.55	75.5	25.82	251
3	PB-YIG5%	12.3891	12.3891	12.3891	90	4.38	48.4	23.10	173
4	YIG_Ref #CIF-1533341	12.3814	12.3814	12.3814	90	1.19	13.33	11.97	9.01

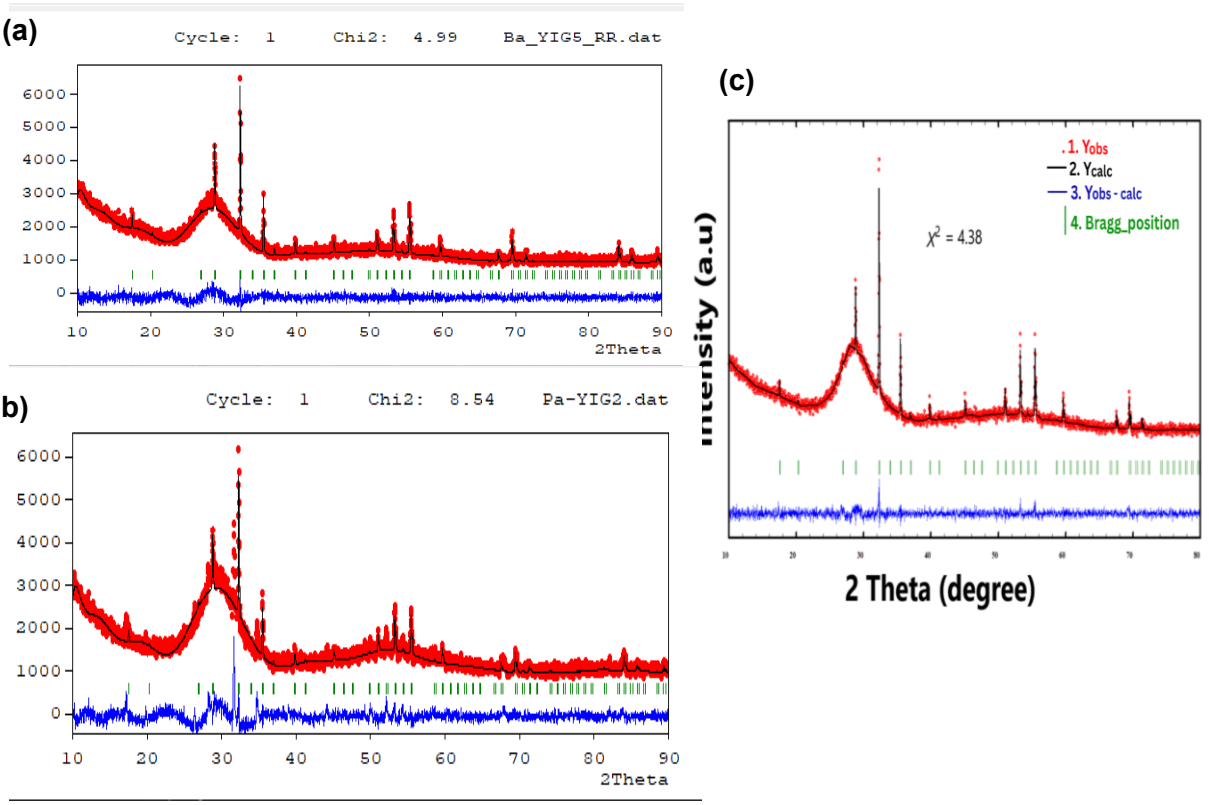

Figure 42. *Rietveld refinement of (a) Ba-YIG5, (b) Pb-YIG2, and (c) PB-YIG5% samples.*

For the Ba-YIG5 sample and the PB-YIG5% sample, the experimental diffraction patterns show very good agreement with the calculated YIG reference pattern [4]. The difference curve (Yobs – Ycalc) remains low and shows no significant features across the main peaks, indicating that the YIG model describes the crystalline phase well in both samples. The refined lattice parameters (a = 12.389 Å for PB-YIG5% and a = 12.3872 Å for Ba-YIG5) are very close to the reported value for pure YIG (a = 12.381 Å), confirming that the crystals retain the expected cubic garnet structure [5]. No additional phases were needed

during refinement, suggesting that the BaO-based matrix supports the formation of a single YIG phase.

For the Pb-YIG2 sample, the refinement gives a higher χ^2 value (8.55) and more noticeable differences between the experimental and calculated patterns. The main peaks still correspond to YIG, but additional reflections are present, indicating the formation of secondary phases. The lattice parameter (a = 12.402 Å) is slightly larger than the reference value, which may be related to lattice distortion or internal strain.

All samples show relatively high R-factors (Rwp, Rp) and χ^2 values compared to fully crystalline YIG materials. This is expected, as the samples are glass-ceramics, in which a crystalline phase coexists with a residual amorphous matrix. The amorphous contribution increases the background signal and affects the fitting quality, even when the crystalline phase is well described.

The results show that Ba-YIG5 and PB-YIG5% mainly contain a well-formed YIG phase, while Pb-YIG2 presents a more complex structure with additional phases. This difference reflects how the glass composition influences the crystallization process.

4.1.2 XRD Single crystal

Single-crystal X-ray diffraction analysis (Table 10) resolved the crystal structures of both Ba-YIG2 and Pb-Ba-YIG5% samples, confirming that the isolated crystals in each composition correspond to yttrium iron garnet ($Y_3Fe_5O_{12}$) [4]. In both samples, the structure crystallizes in the cubic system with space group Ia-3d (No. 230), which is characteristic of garnet-type oxides [2] and aligns with established YIG crystallography [4].

Table 10. Single-Crystal XRD and structure refinement data for YIG

Crystal Data	**Ba-YIG2**	**Pb-Ba-YIG5%**
Chemical Formula	$Y_3Fe_5O_{12}$	$Y_3Fe_5O_{12}$
M_r	737.98	737.98
Chemical System, Space Group	Cubic, *Ia*-3*d* (No. 230)	Cubic, *Ia*-3*d* (No. 230)
a = b = c (Å)	12.3942(2)	12.4006(2)
α = β = γ (°)	90	90
Unit Cell Volume ($Å^3$)	1903.95(9)	1906.90(9)
Z	8	8
Temperature (K)	100.00(11)	100(2)
Radiation type	Mo Kα (λ = 0.71073 Å)	Mo Kα (λ = 0.71073 Å)
Absorption coefficient, μ (mm^{-1})	25.522	25.482
Crystal Size (mm^3)	0.16 × 0.11 × 0.04	0.24 × 0.19 × 0.14
Data Collection		
Diffractometer	XtaLAB Synergy, Dualflex, HyPix	
Absorption correction	Gaussian numerical absorption correction + spherical harmonics (SCALE3 ABSPACK)	
T_{min}, T_{max}	4.027 / 26.958	
No of measured, independent and observed [I >2σ(I)] reflections	16764 / 178 / 176	10528 / 166 / 166
R_{int}	0.0518	0.0828
(sin θ/λ)max ($Å^{-1}$)	0.638 $Å^{-1}$	0.80 $Å^{-1}$
Refinement		
R[I >2σ(I)], R_1 (all data), wR_2 (all data)	0.0386, 0.0390, 0.1292	0.0463, 0.0463, 0.1246
Goodness-of-fit on F^2	1.251	1.264
No of reflections	178	166
Parameters refined	18	18
Δρmax, Δρmin (e $Å^{-3}$)	+0.998, −1.792	+1.098, −1.383
Completeness (%)	100.00	100.00

A direct comparison of the two samples reveals only a marginal variation in the lattice parameter, increasing from a = 12.3942(2) Å for Ba-YIG2 to a = 12.4006(2) Å for Pb-Ba-YIG5%. This slight expansion (~0.006 Å) is measurable and suggests that Pb incorporation within the Ba-containing glass matrix subtly modifies the crystallization environment. Since the refined chemical formula remains unchanged ($Y_3Fe_5O_{12}$), this shift is likely associated

with lattice strain or minor local distortions rather than direct substitution into the garnet structure. This behavior aligns with previous observations in substituted YIG systems, where small lattice changes result from indirect effects such as strain, defect chemistry, or residual glass interactions rather than full cation incorporation into crystallographic sites.

The unit cell volumes exhibit a similar trend, increasing from 1903.95(9) Å³ for Ba-YIG2 to 1906.90(9) Å³ for Pb-Ba-YIG5%, further supporting the presence of slight lattice expansion. Despite this, the preservation of cubic symmetry and the absence of symmetry-lowering confirm that the garnet structure remains intact. Such structural stability is characteristic of YIG, which possesses a highly constrained oxygen sublattice and a rigid cation coordination network.

Both structural refinements confirm the classical garnet topology (Fig. 43), with Y^{3+} occupying the dodecahedral (24c) sites and Fe^{3+} distributed between octahedral (16a) and tetrahedral (24d) sites [4], [6]. This cation distribution defines YIG and underpins its magnetic and structural stability [7], [8], [9]. The preservation of this arrangement in both compositions indicates that the glassy phase does not disrupt cation ordering within the garnet lattice. Instead, the glass matrix primarily influences the environment from which crystallization occurs.

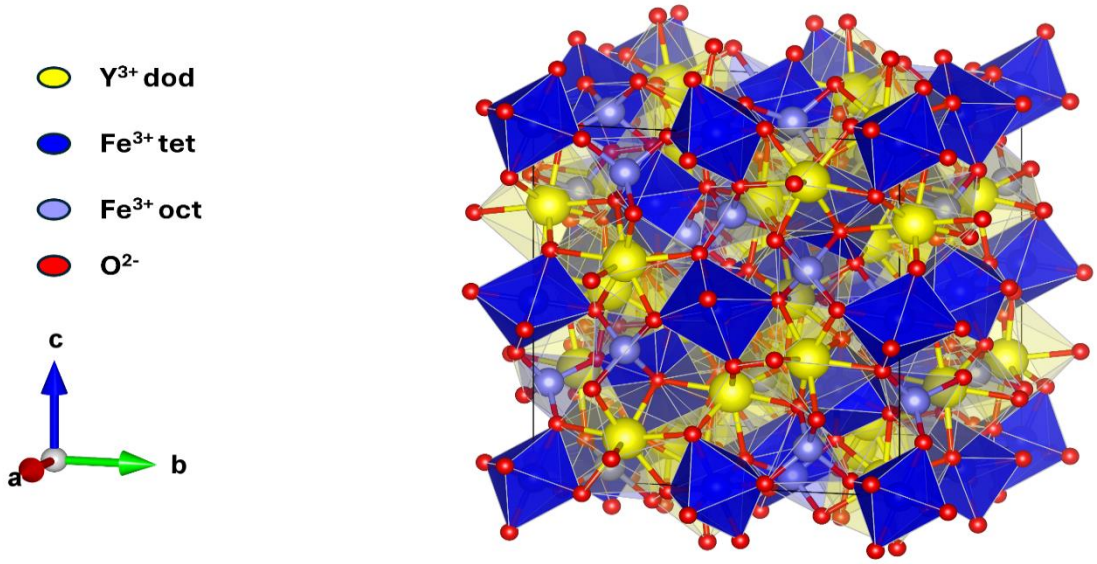

Figure 43. Unit cell of YIG garnet structure with a lattice constant a = 12.3942(2) Å, which consists of 160 atoms, including 24 Y, 40 Fe, and 96 O atoms. [Author ownership].

The refinement quality offers additional insight into structural differences between the samples. Ba-YIG2 demonstrates slightly better agreement factors (R_1 = 0.0386, Rint = 0.0518) than Pb-Ba-YIG5% (R_1 = 0.0463, Rint = 0.0828). While both sets of values are within acceptable limits for single-crystal refinements, the higher residuals in the Pb-containing sample may reflect increased microstructural complexity. This complexity could result from minor disorder, strain fields, or compositional heterogeneity introduced during crystallization from the Pb-containing glass. The increase in $(\sin\theta/\lambda)_{max}$ from 0.638 $Å^{-1}$ to 0.80 $Å^{-1}$ further suggests differences in data resolution that may affect refinement stability.

Despite these differences, both samples exhibit 100% completeness and comparable goodness-of-fit values (1.25–1.26), indicating reliable datasets and well-converged refinements. Notably, no additional atomic sites or secondary crystalline phases were detected in either structure, confirming that both compositions yield phase-pure YIG at the single-crystal level. This finding is significant, as powder XRD indicated more complex phase behavior, including a mixture of crystalline and amorphous phases, suggesting that the single-crystal analysis was performed on an isolated iron garnet crystal.

These results demonstrate that crystallization from Ba- and Pb-modified glass matrices yields structurally consistent YIG crystals, with only minor variations in lattice parameters and refinement quality. The invariance of the space group and cation distribution underscores the structural tolerance of the garnet lattice. The observed lattice expansion and increased residuals in Pb-Ba-YIG5% are attributed to secondary effects associated with the crystallization environment rather than intrinsic structural modification.

In summary, analysis of Table 10 and the unit cell representation (Fig. 43) demonstrates that the supersaturated glass route reliably produces well-defined YIG single crystals. However, the presence of Pb introduces measurable, albeit limited, structural perturbations that merit further investigation, particularly regarding local strain, defect chemistry, and their potential effects on functional properties such as magnetism and optical behavior.

4.2 Raman Spectroscopy

The Raman spectra of the synthesized glass-ceramics are shown in Fig. 44 for the BaO-based, PbO-based, and PB-YIG5% systems. A reference Raman spectrum reported for yttrium iron garnet ($Y_3Fe_5O_{12}$) was used for comparison.

YIG crystallizes in the cubic garnet structure with space group Ia-3d, for which group theory predicts 25 Raman-active modes ($3A_1g + 8E\ g + 14T_2g$) [4]. In practice, only part of these modes is clearly resolved because of band overlap, crystallinity effects, and differences in Raman scattering intensity. The most prominent Raman features are associated with internal vibrations of FeO_4 tetrahedra and FeO_6 octahedra, while the low-frequency modes below 300 cm^{-1} are mainly related to translational vibrations involving Y^{3+} and Fe^{3+} ions in the garnet lattice [4]. Characteristic Raman bands of YIG are commonly reported near 188, 267, 340, 500, 580, and 730 cm^{-1} [3], [10].

The Raman spectra of the BaO-based samples are presented in Fig. 45a, while the full spectral range of Ba-YIG2 is shown in the inset of Fig. 45b. The detailed Raman spectrum and mode assignments for Ba-YIG2 are shown in Fig. 45c, and the experimental Raman-active modes are summarized in Table 11. The measured peak positions are in good agreement with reported Raman modes for cubic YIG [3], [11].

For the BaO-based samples (Ba-YIG1 to Ba-YIG5) and PB-YIG5%, the spectra reproduce the main Raman features associated with YIG formation. The bands near 169–190 cm^{-1} and around 268 cm^{-1} are attributed to low-frequency lattice vibrations involving Fe–O polyhedra. Additional bands observed between approximately 300 and 700 cm^{-1} are associated with internal vibrational modes of FeO_4 tetrahedra and FeO_6 octahedra, while the high-frequency band near 728–730 cm^{-1} is assigned to symmetric Fe–O stretching vibrations of the garnet structure [3], [10].

In most BaO-based samples, the band near 268 cm^{-1} appears more intense than the band near 189 cm^{-1}, which agrees with previously reported Raman spectra of YIG and Bi:YIG systems [3], [10]. However, in Ba-YIG1 the band near 189 cm^{-1} becomes relatively more pronounced. This difference may be related to local structural disorder, incomplete crystallization, or the presence of minor secondary phases, which is consistent with the weak hematite reflections observed in the XRD pattern of Ba-YIG1.

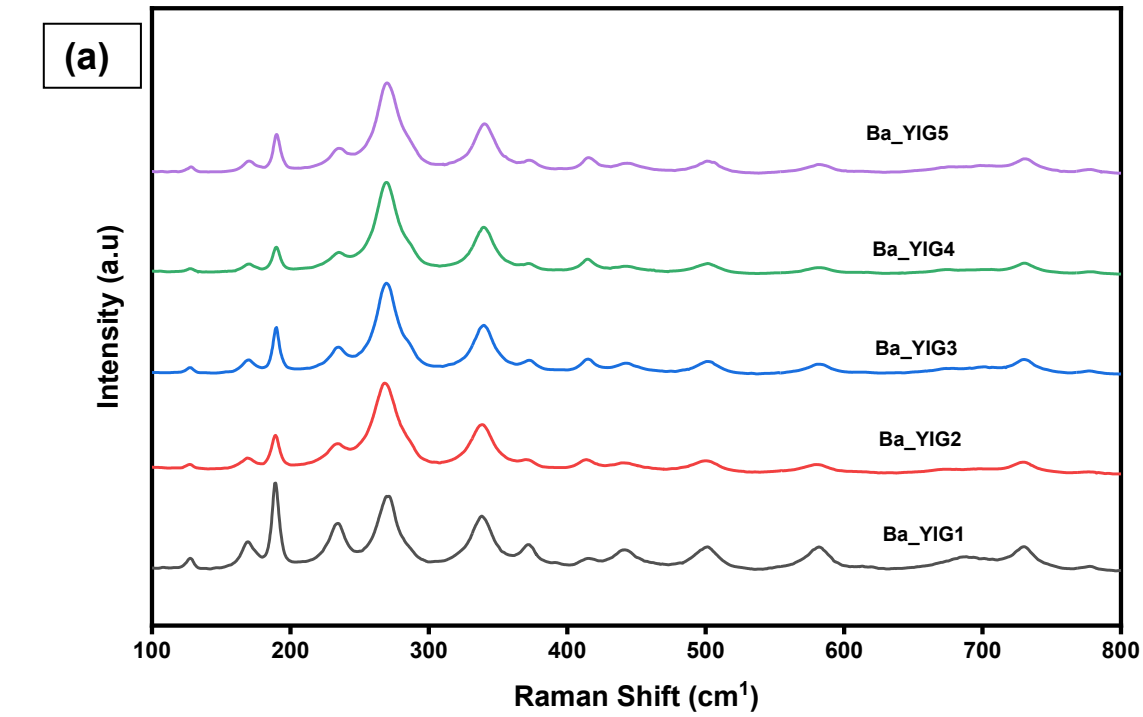
(a)
Ba_YIG5
Ba_YIG4
Ba_YIG3
Ba_YIG2
Ba_YIG1
Intensity (a.u)
100
200
300
400
500
600
700
800
Raman Shift (cm1)

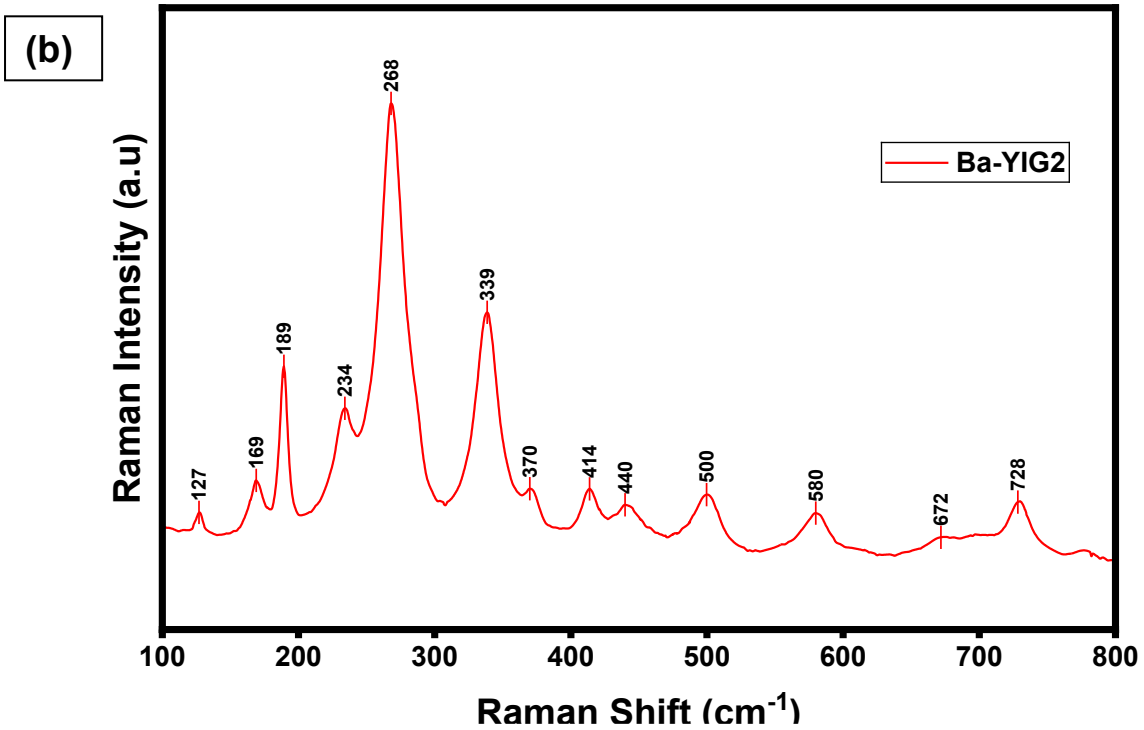
(b)
Ba-YIG2
Raman Intensity (a.u)
127
169
189
234
268
339
370
414
440
500
580
672
728
100
200
300
400
500
600
700
800
Raman Shift (cm-1)

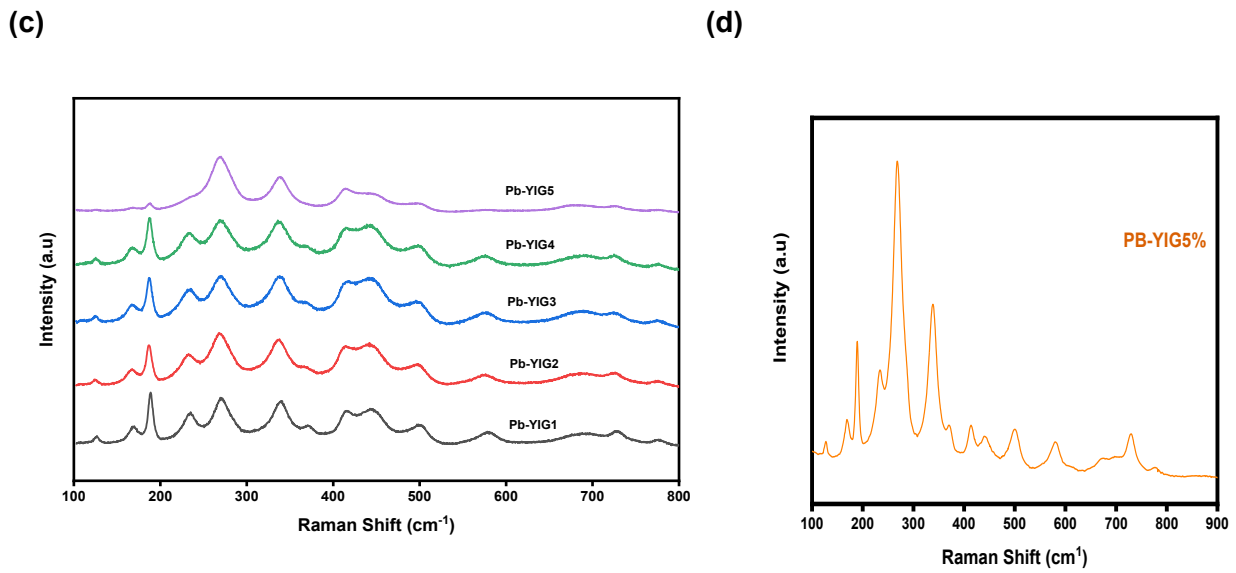

Figure 44. Raman spectra of the YIG glass-ceramic samples: (a) (Ba-YIG1 to Ba-YIG5) samples (b), detailed Raman spectrum of Ba-YIG2 with peak assignments, (c) PbO-containing samples (Pb-YIG1 to Pb-YIG5), and (d) PB-YIG5%.

The Raman spectra of the PbO-based samples (Pb-YIG1 to Pb-YIG5), shown in Fig. 45d, are broader and less resolved compared with the BaO-based compositions. Although several bands associated with YIG are still observed, the characteristic band near 268 cm^{-1} becomes less distinct, and broader spectral features are present in the 400–500 cm^{-1} region. These changes suggest increased structural disorder and possible overlap with additional iron-containing phases, in agreement with the XRD results. The broader Raman bands also indicate lower crystallinity and a less ordered local structure in the PbO-based samples.

The PB-YIG5% sample (Fig. 45e) exhibits Raman bands that are better defined than those of the PbO-based series and remain close to the characteristic YIG modes. This behavior suggests that partial substitution of PbO by BaO improves the structural ordering of the garnet phase and favors YIG crystallization.

Table 11. Experimental Raman-active Modes Assignments and Wavenumbers (YIG Samples)

	References for YIG Modes Assignments		Investigated YIG Single-crystals Modes		
Symmetry mode	**Literature 1 position after [12](cm⁻¹)**	**Literature 2 measured position [4] (cm⁻¹)**	**Ba-YIG1 (cm⁻¹)**	**Ba-YIG2 (cm⁻¹)**	**Ba-YIG5 (cm⁻¹)**
T	131	122	127	127	128
T	174	163	169	168	170
T	194	186	189	189	190
T	238	233	234	234	235
E + T	274	265	270	268	269
E	346	333	338	338	340
T	378	364	372	369	372
E/T	416/419	403/411	415	413	415
T/E	445/456	435/445	440	439	442
A	504	500	501	500	501
T	592	577	581	579	581
A or E + T	736	725	729	728	730

4.3 Morphological Analysis

The size, shape, and distribution of the YIG crystals were examined using an optical microscope (Leica DM2500M) with magnifications ranging from 5× to 100×. Observations were made both on the as-prepared glass-ceramic samples and on crystals isolated after removing the glass matrix.

Figure 45 shows photographs and optical micrographs of the samples and the crystals that were isolated after the matrix was removed. The first row (a) presents the bulk glass-ceramics for the PbO-based, BaO-based, and PB-YIG5% systems. It was observed macroscopically that the BaO-based samples appear more rigid and mechanically stable

compared to the PbO-based ones. The second row (b) shows the optical microscopy of the crystals within the glass-ceramic matrix, which confirms that nucleation and growth happened during controlled cooling. After dissolving the amorphous matrix with acid, the isolated crystals have clear cubic shapes. The third row (c) shows the isolated crystals after acid etching.

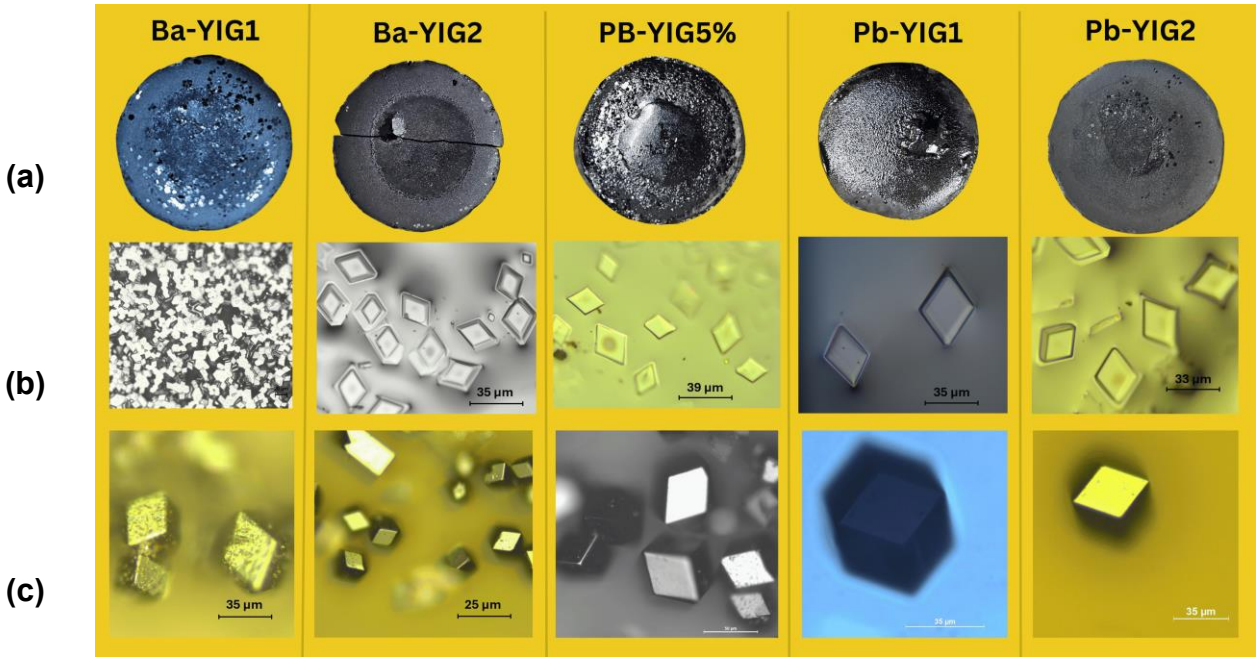

Fig. 45. Photographs and optical micrographs (20×) of YIG crystals before and after glass matrix removal: (a) Ba-YIG1–Ba-YIG5 glass-ceramics as prepared, (b) YIG crystals embedded in the glass matrix, and (c) isolated YIG single crystals after acid etching.

The crystals maintain a well-defined cubic shape, with sizes ranging from about 5 to 50 µm. Their sharp edges and regular shapes match the cubic garnet structure of $Y_3Fe_5O_{12}$. Albino et al. also reported similar faceted garnet crystals for Tm^{3+}/Er^{3+}-doped Yb-YGG single crystals made by controlled cooling of a multicomponent glass matrix, which further supports the effectiveness of this glass-based crystal growth method for rare-earth garnet systems [14].

4.4 SEM–EDS Analysis

The composition and microstructure of the samples were studied using SEM coupled with EDS. The analysis was carried out on polished surfaces of the PbO-based, BaO-based, and PB-YIG5% glass-ceramics containing YIG crystals.

Figure 46(a) shows YIG crystals set in the glass matrix. These crystals are well developed and surrounded by residual amorphous material, indicating in situ crystallization during heat treatment. Their separate placement suggests that nucleation and growth were controlled inside the glass.

Once the glass phase is removed, the crystals shown in Figure 46 (b) have a clear cubic shape and are about 10 micrometers in size. Their sharp edges and regular form match the cubic garnet structure of $Y_3Fe_5O_{12}$ [16], which often yields well-shaped crystals due to its symmetry. Since the crystals are not clumped together, they formed separately rather than by sintering. These details confirm that well-formed YIG single crystals were produced.

Compared to the SEM images of LHPG-grown YIG single-crystal fibers by Hong et al. [17], which showed more irregular and rounded crystal shapes at larger sizes (about 20 μm), the YIG crystals in this study have a clear cubic structure even at around 10 μm. This suggests a high level of crystallographic development.

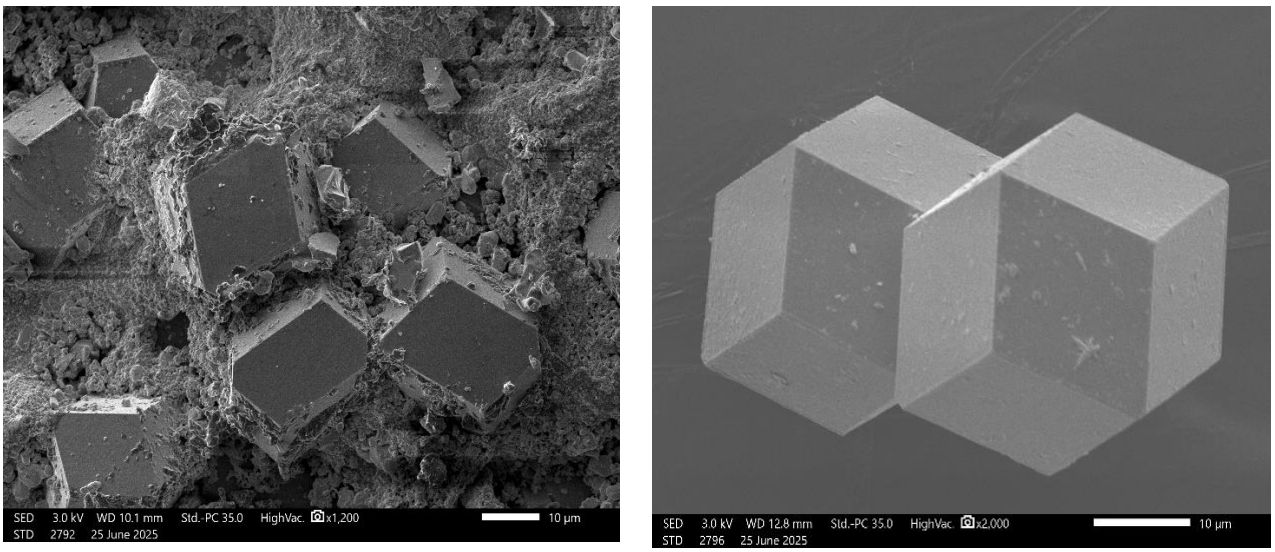

(a) **(b)**

Figure 46. SEM images of $Y_3Fe_5O_{12}$ (YIG) crystals: (a) YIG crystals embedded within the glass-ceramic matrix after thermal treatment, and (b) isolated YIG single crystals obtained after chemical etching of the residual glass phase.

Fig 47. Present the EDS spectra show peaks corresponding to Y, Fe, Bi, Pb, Ge, and Ba, which match the expected composition of the glass systems. Since the measurements were performed on the composite material, the detected elements come from both the crystalline phase (YIG) and the surrounding glass matrix.

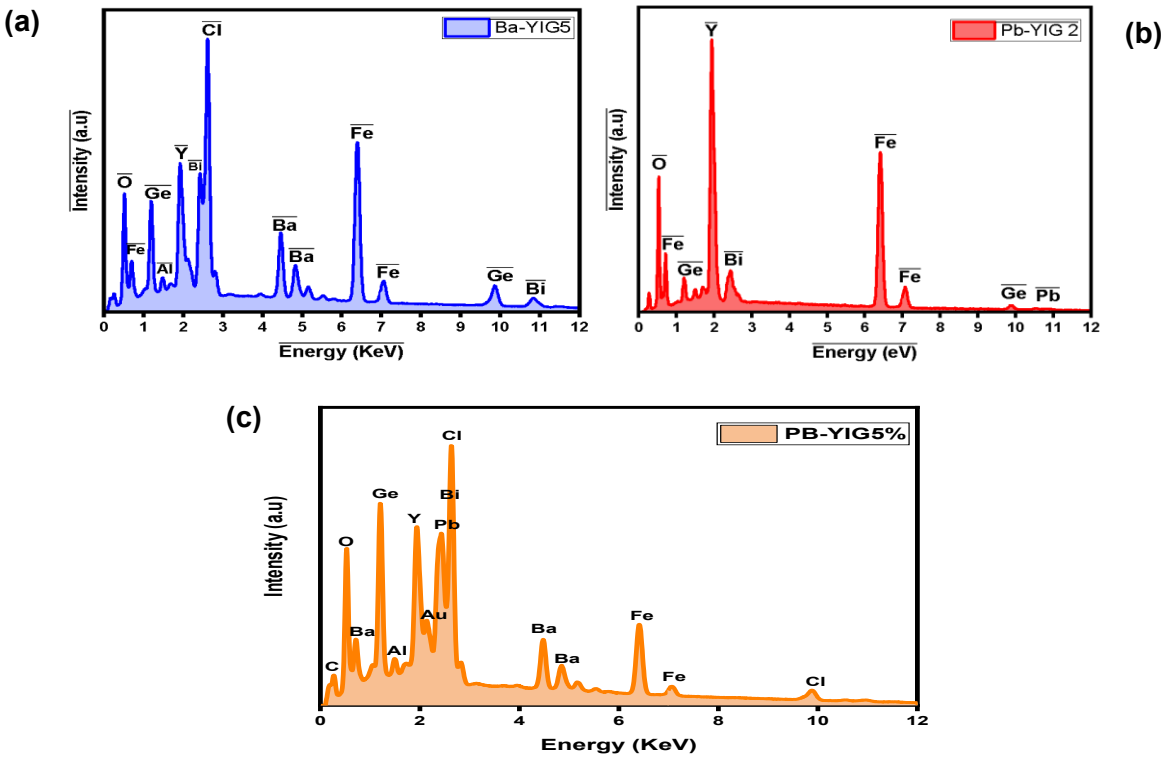

Figure 47. EDS spectra of (a) Ba-YIG1, (b) Pb-YIG2, and (c) Pb-YIG5% samples confirming elemental composition.

Elemental mapping gives a clearer picture of the phase distribution. The crystals are enriched in Y, Fe, and O (Fig. 48), confirming the synthesis of $Y_3Fe_5O_{12}$, as also reported by Hong et al., 2026 [31] . The surrounding glass contains Pb, Ge, and Bi in the PbO-based system, Ba, Ge, and Bi in the BaO-based system, and a combination of Pb, Ba, Ge, and Bi in PB-YIG5%, as expected.

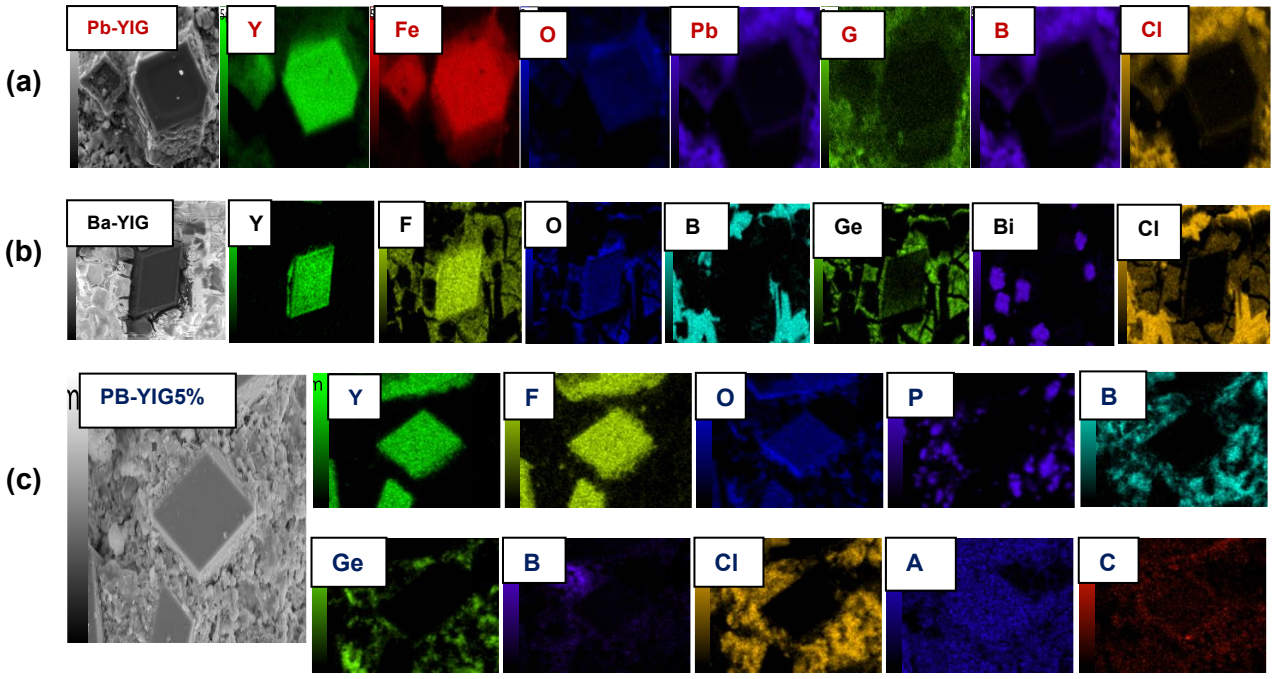

Figure 48. SEM micrographs of (a) Ba-YIG1, (b) Pb-YIG2, and (c) Pb-YIG5% glass-ceramics showing YIG crystal morphology.

No visible porosity was found, which shows that the material is well densified. The small Cl signals come from leftover HCl used during sem-eds to etch the glass surface and reveal the crystals, while the C signal comes from the carbon tape [16]. The Al and Au peaks are due to the sample holder and the sputter coating. These results show a clear separation between the crystalline and glassy phases, and also support that YIG single crystals formed in the glass matrix, matching the results from the XRD analysis.

4.5 FTIR Spectroscopy

FTIR spectroscopy was used to examine the bonding characteristics and phase formation of the YIG single-crystal samples. The spectra recorded in the 400–4000 cm^{-1} region are shown in Fig. 49a for the Ba-YIG series and in Fig. 49c for PB-YIG5%. All samples exhibit strong absorption bands within the 470–750 cm^{-1} region, which is characteristic of metal–oxygen vibrations in garnet structures.

A low-frequency band near 473 cm^{-1} is assigned mainly to Fe–O vibrations associated with octahedral sites of the garnet structure, with possible contribution from Y–O vibrations related to Y^{3+} ions in dodecahedral coordination [14]. The relatively low position of this band is consistent with the higher atomic mass of yttrium compared with lighter cations. Broad

bands observed around 3450 cm^{-1} and 1635 cm^{-1} correspond to O–H stretching and H–O–H bending vibrations, respectively, indicating the presence of adsorbed moisture or hydroxyl groups on the crystal surfaces. A weak feature near 1375 cm^{-1} may be associated with residual carbonate species or traces of remaining glass components after the etching process [15].

(a)

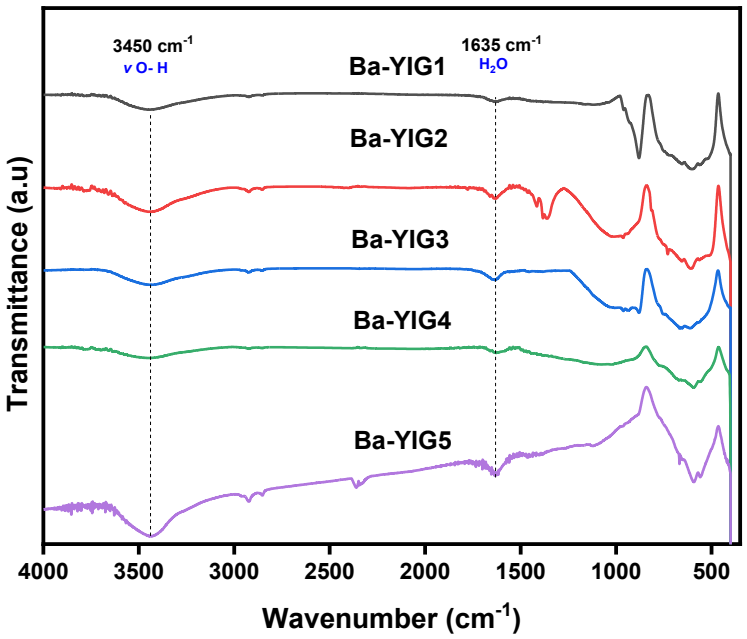

(b)

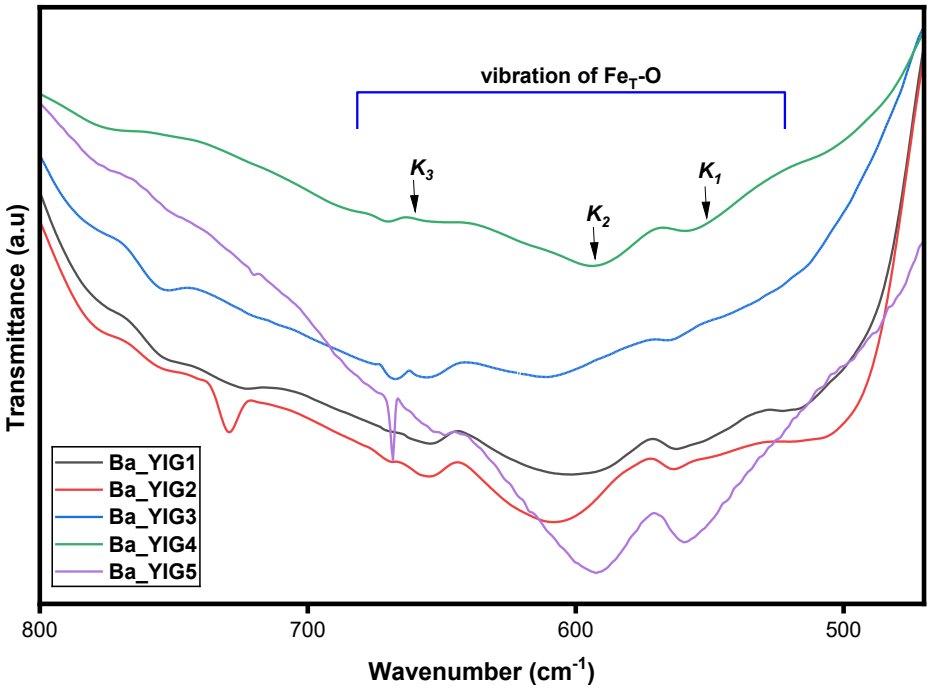

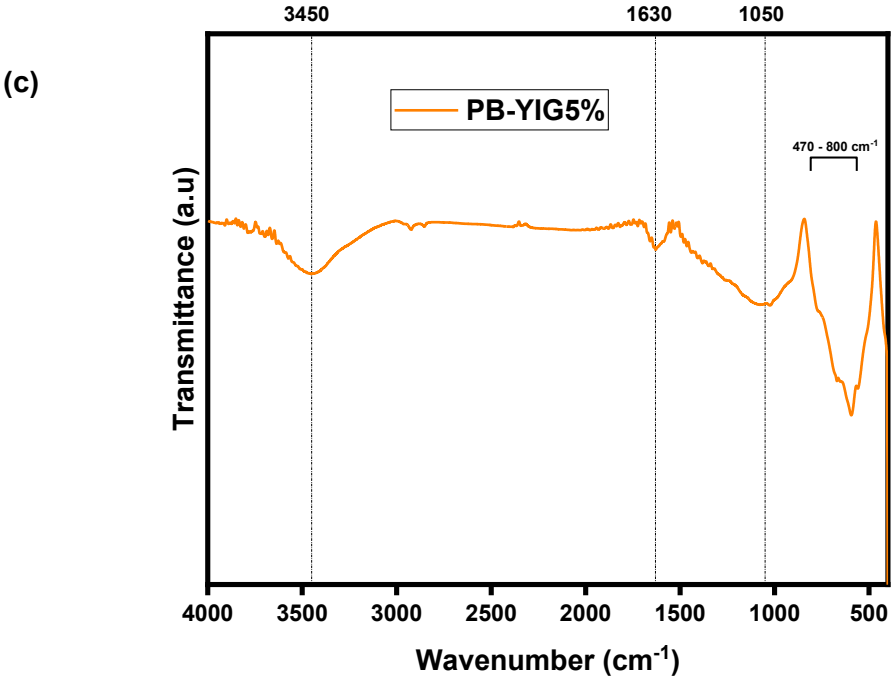

Figure 49. FTIR spectra of YIG single-crystal samples: (a) Ba-YIG1 to Ba-YIG5 over the 400–4000 cm^{-1} range, showing the characteristic Fe–O and O–H vibrational bands; (b) expanded view of the 470–800 cm^{-1} region highlighting the Fe–O vibrational bands (k_1, k_2, and k_3); and (c) FTIR spectrum of PB-YIG5% showing the characteristic Fe–O and O–H vibrational bands.

To better visualize the metal–oxygen vibrations, the 470–800 cm^{-1} region is enlarged in Fig. 49b. Three characteristic bands are observed near 565 cm^{-1} (k_1), 610 cm^{-1} (k_2), and 664 cm^{-1} (k_3). These bands are associated with Fe–O stretching vibrations involving tetrahedral FeO_4 units in the garnet lattice [16]. Slight variations in band position and spectral definition are observed among the Ba-YIG samples, suggesting small differences in the local bonding environment and crystallization state. Similar behavior has been reported for rare-earth iron garnets, where variations in lattice dimensions and Fe–O bond lengths influence the vibrational frequencies of the garnet structure [17], [18].

The FTIR spectrum of PB-YIG5% shown in Fig. 49c exhibits the same characteristic Fe–O vibrational region observed for the Ba-YIG series, confirming the formation of the garnet structure in the mixed Pb/Ba system. The bands associated with Fe–O vibrations are

relatively well defined, which agrees with the XRD and Raman results obtained for this sample. In addition, the O–H stretching and bending bands near 3450 cm^{-1} and 1630 cm^{-1} are also present, indicating small amounts of adsorbed moisture on the crystal surface.

Overall, the observed vibrational bands are consistent with previous infrared studies of YIG and related garnet systems, where the characteristic phonon modes are commonly located within the 400–700 cm^{-1} region [19]. The FTIR results therefore support the formation of the YIG garnet phase in both the BaO-based and mixed Pb/Ba glass-ceramic systems.

4.6 Magnetic Properties of YIG Single crystals

A simple qualitative test of the magnetic behavior of the glass-ceramic and the YIG single crystals is shown in Fig. 50. The glass-ceramic sample is attracted to an external magnet, indicating the presence of a magnetic phase. A similar behavior is observed for the isolated YIG crystals in Fig. 51, where the particles respond quickly when suspended in water and exposed to a permanent magnet. The particles are clearly drawn toward the magnetic source, demonstrating a strong magnetic response consistent with previous observations [28].

Figure 50. *Image showing the YIG glass-ceramic and its response to a magnetic field.*

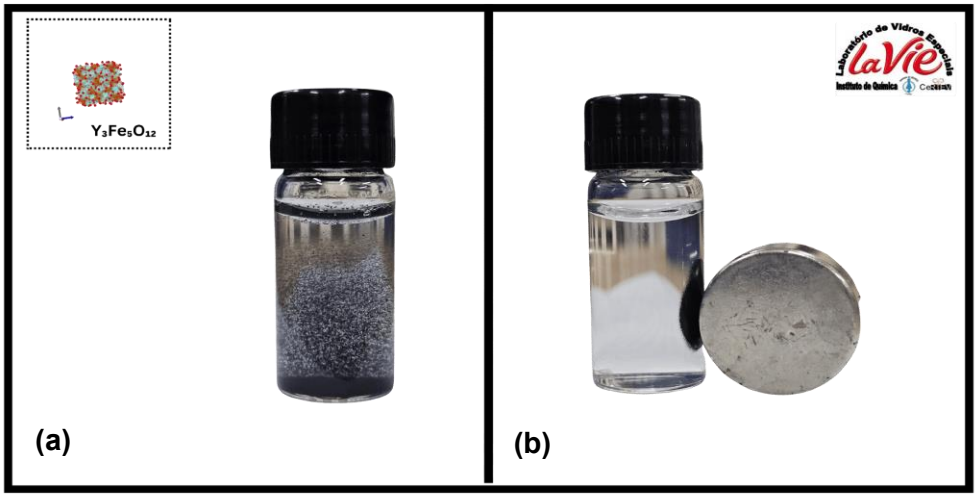

Figure 51. *(a) YIG single crystals suspended in water and (b) their response to an external magnetic field.*

The effect is visible at the macroscopic scale, as the particles move and accumulate in the direction of the applied magnetic field. This behavior originates from the ferrimagnetic nature of $Y_3Fe_5O_{12}$. In the garnet structure, oxygen ions form the framework, while cations occupy three types of sites: dodecahedral (c), octahedral (a), and tetrahedral (d). The cation distribution follows $Y_3(Fe^{3+})_2[Fe^{3+}]_3O_{12}$, where Y^{3+} occupies the dodecahedral sites and Fe^{3+} occupies both octahedral and tetrahedral sites.

The magnetic moment mainly arises from Fe^{3+} ions. The magnetic moments at the octahedral and tetrahedral sites are aligned in opposite directions through superexchange interactions mediated by oxygen ions. This results in a net magnetic moment and explains the observed ferrimagnetic behavior.

These results indicate that the crystals may be useful for magnetic–dielectric applications, particularly at radio frequencies. Mallmann et al. [17] reported similar behavior in chitosan/gelatin/YIG composites prepared using glutaraldehyde as a crosslinking agent, where the materials also showed potential for functional magnetic biocomposites.

The garnet structure is also responsible for the magneto-optical properties of YIG and its low magnetic losses, which are important for optical and microwave applications.

4.6.1 Magnetic Hysteresis of YIG Single-crystals

The magnetic properties of the YIG single crystals were investigated using magnetization–field (M–H) measurements at 300 K and 2 K. The hysteresis loops for Ba-YIG2 and Ba-YIG5 are shown in Figure 52(a–b).

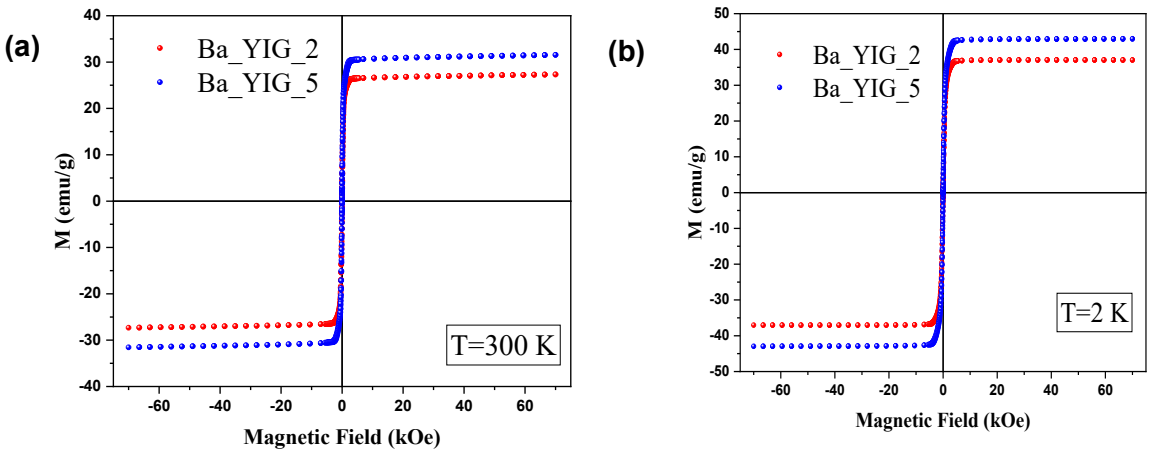

Figure 52. Magnetization as a function of the applied magnetic field (M–H loops) for YIG single crystals Ba-YIG2 and Ba-YIG5 measured at (a) 300 K and (b) 2 K, with

At both temperatures, the samples exhibit narrow hysteresis loops with rapid saturation, indicating typical soft ferrimagnetic behavior of $Y_3Fe_5O_{12}$. The magnetization approaches saturation at relatively low fields, while the coercive field remains small, which is consistent with reported YIG systems [32], [37].

The saturation magnetization M_s, remanent magnetization M_r, and coercive field H_c were extracted from the corrected M–H loops, these properties are presented in Table 12. The saturation magnetization was estimated after linear high-field correction using:

$$M_{corr} = M_{measured} - \chi H \qquad \text{(Eq. 18)}$$

where χ is the high-field susceptibility obtained from the linear region of the M–H curve.

Table 12. Properties obtained from hysteresis loop for YIG single-crystals.

Sample	T (K)	(Ms) (emu/g)	(Mr) (emu/g)	(Hc) (Oe)
Ba-YIG2	300	26.75	1.82	24.7
Ba-YIG5	300	30.80	2.29	25.0
Ba-YIG2	2	37.0	1.52	25
Ba-YIG5	2	42.9	0.56	3.04

The increase in M_s at 2 K is attributed to reduced thermal spin disorder, which enhances magnetic ordering. Ba-YIG5 shows higher M_s compared to Ba-YIG2 at both temperatures, suggesting improved magnetic phase contribution or crystallinity. The overall shape of the loops remains unchanged with temperature, which suggests that the magnetic ordering is stable.

The coercivity values remain low (3–25 Oe), confirming the soft magnetic nature of the samples. Such low H_c values are typical for YIG due to its low magneto-crystalline anisotropy [37]. Comparable values of M_s 23.23 emu/g and H_c 30.1 Oe have been reported for well-crystallized YIG materials [31]. The low coercivity also suggests low pinning of domain walls, which can be related to good crystal quality and low defect concentration.

For the Pb_Ba_YIG5% sample, the hysteresis loop shows a similar shape but with a slightly lower magnetization compared to the Ba-YIG samples. The loop remains narrow, indicating that the ferrimagnetic character is preserved. The reduction in magnetization may be related to differences in phase purity or the presence of non-magnetic components originating from the glass system.

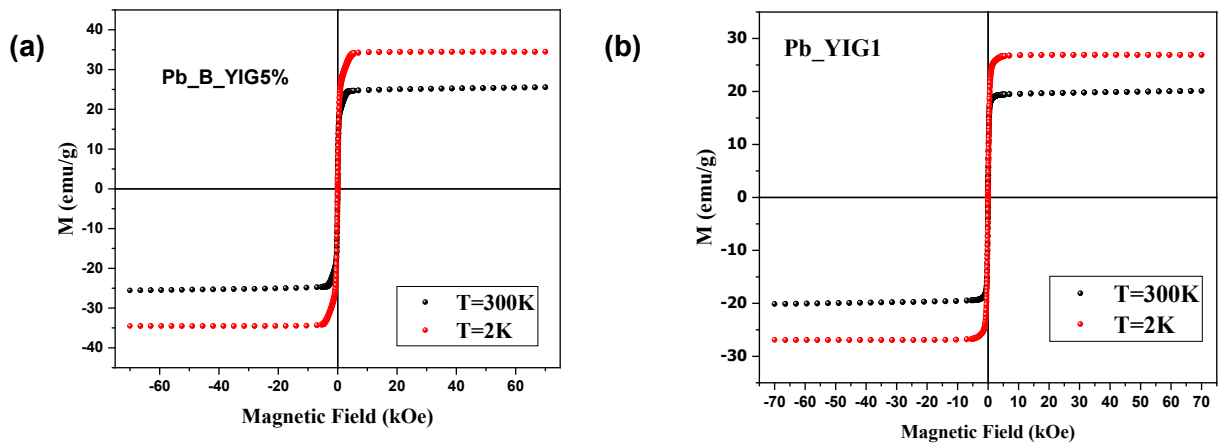

Figure 53. Magnetic hysteresis cycles for a) Pb-Ba-YIG5% and b) Pb-YIG samples measured at 300 K and 2 K.

In contrast, the Pb-YIG1 sample shows a lower magnetization overall and a less steep approach to saturation. The loop still indicates ferrimagnetic behaviour, but the reduced magnetization and slight change in shape suggest that the magnetic phase is less developed. This is consistent with the earlier structural results, where secondary phases were observed in Pb-based compositions.

Across all samples, the increase in magnetization at 2 K compared to 300 K follows the expected behaviour for ferrimagnetic materials. The absence of any significant loop opening or anomalous features indicates that no superparamagnetic behaviour is present, which is in line with the micrometer size of the crystals.

4.6.2 ZFC and FC Measurements of YIG Single-crystals

The temperature dependence of magnetization measured under an applied field of 100 Oe is shown in Fig. 54(a,b) for Ba-YIG2 and Ba-YIG5.

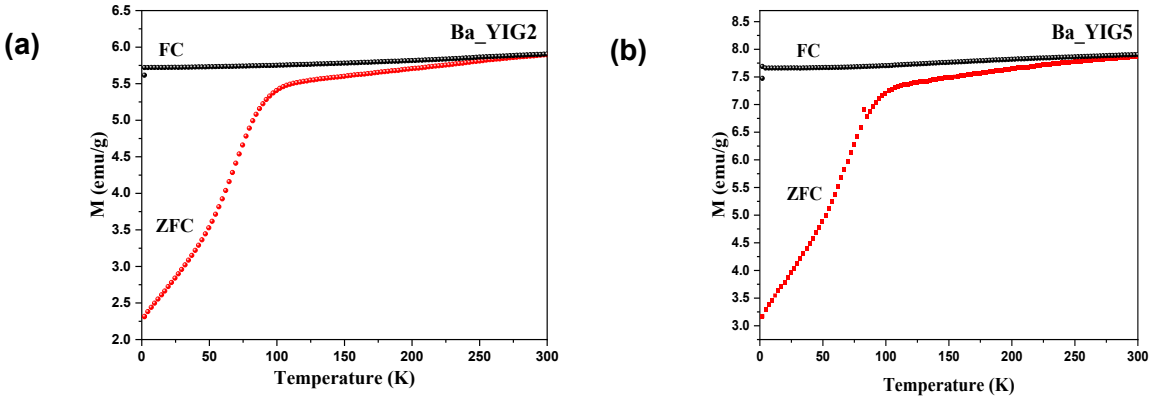

Figure 54. Temperature dependence of magnetization measured by zero-field-cooled (ZFC) and field-cooled (FC) methods for (a) Pb-Ba-YIG5% and (b) Pb-YIG samples. (Own authorship).

The FC magnetization remains higher than the ZFC magnetization throughout the measured temperature range, while the ZFC curve gradually approaches the FC branch with increasing temperature. No blocking peak is observed in the ZFC curves.

This behavior confirms the absence of superparamagnetic effects and indicates stable ferrimagnetic ordering, which is consistent with YIG and its high Curie temperature (~559 K) [32]. The separation between the ZFC and FC curves is more pronounced at low temperatures and decreases as the temperature increases. This behavior is typical of ferrimagnetic systems where magnetic anisotropy and domain wall pinning affect the magnetization at low temperature, while thermal energy assists domain alignment at higher temperatures.

For both Ba-YIG2 and Ba-YIG5, the FC curves remain nearly constant over the measured temperature range, whereas the ZFC curves start at lower magnetization values and gradually increase with temperature before approaching the FC branch. Ba-YIG5 exhibits higher magnetization values than Ba-YIG2 across the full temperature range, which agrees with the hysteresis results and suggests improved crystallization or a higher fraction of magnetic YIG phase in this sample.

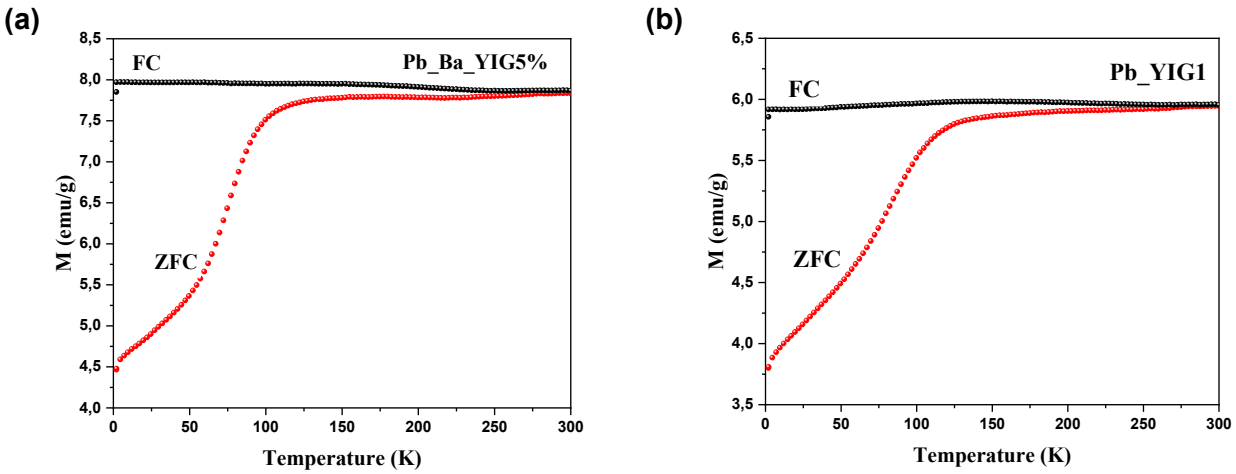

Figure 55. Temperature dependence of magnetization measured by zero-field-cooled (ZFC) and field-cooled (FC) methods for (a) Pb-Ba-YIG5% and (b) Pb-YIG samples. (Own authorship).

The Pb-Ba-YIG5% sample exhibits behavior similar to the Ba-based samples, with gradual convergence of the ZFC and FC curves at higher temperatures. The overall magnetization remains comparable to the Ba-YIG samples, indicating that the mixed Pb/Ba system also supports the formation of ferrimagnetic YIG.

For the Pb-YIG samples, the magnetization values are lower and the ZFC curve increases more gradually with temperature. The smaller separation between the ZFC and FC curves suggests weaker magnetic interactions and a reduced fraction of well-crystallized YIG phase, which is consistent with the XRD and Raman results.

4.6.3 Magnetic and Magneto-Optical Performance Correlation

The magnetic parameters obtained in this study are consistent with reported YIG systems. The relatively high saturation magnetization and low coercivity indicate the successful formation of ferrimagnetic $Y_3Fe_5O_{12}$ single crystals with stable magnetic behavior.

The higher Ms observed for Ba-YIG5 suggests improved crystallinity and a lower contribution from non-magnetic phases or residual glass impurities. In contrast, the slightly lower magnetization values obtained for Ba-YIG2 may be associated with minor structural disorder or residual amorphous content remaining after the extraction process.

The saturation magnetization values obtained for Ba-YIG2 and Ba-YIG5 fall within the range commonly reported for YIG materials employed in magneto-optical applications. Interestingly, the Pb-Ba-YIG5% sample exhibited the highest saturation magnetization among all investigated compositions, suggesting that the combined PbO/BaO system may favor improved magnetic phase development and ferrimagnetic ordering.

Previous studies have shown that YIG and substituted iron garnets such as Bi:YIG and Ce:YIG exhibit enhanced Faraday rotation and high Verdet constants when high magnetic ordering and phase purity are achieved.

To further contextualize the magnetic behavior of the synthesized crystals, Table 13 compares the saturation magnetization values obtained in this work with reported YIG-based materials used in magneto-optical applications, including systems with measured Verdet constants.

Table 13. Comparison of saturation magnetization and reported Verdet constants for YIG-based materials.

Sample	**Ms (emu/g)**	**Verdet constant/MO Response**	**Wavelength**	**Reference**
Ba-YIG2	26.75	—	—	This work
Ba-YIG5	30.80	—	—	This work
Pb-Ba-YIG5%	34.53	—	—	This work
Pb-YIG1	26.93	—	—	This work
YIG single crystal	25.43 26.9	232 ± 23 rad/m	1.86 μm	[28][29]
YIG	23.23 & 16.43	3.8×10^2 rad T^{-1} m^{-1}	780 nm	[30] [31]
Bi:YIG thin films	26.6	1072038°/T/m 451853○/T/m	1550 nm	[32][29]
Ce:YIG (low/high Ce)	15–28	990 deg/cm 144 deg./cm	1550 nm region	[33] [34][35]
Bi-substituted YIG	11.23	1,565,470 °/T/m 946,238 °/T/m	1310 nm 1550 nm	[36] [37]

Although the Verdet constant was not measured in the present work, the combination of relatively high saturation magnetization, low coercivity, and stable ferrimagnetic behavior suggests that the synthesized crystals are promising candidates for future magneto-optical characterization. The higher Ms observed for Ba-YIG5 may indicate stronger magnetic ordering, which is frequently associated with improved Faraday rotation performance in iron garnet systems.

The relationship between magnetic and magneto-optical properties is particularly relevant for future investigations at telecom wavelengths (~1.55 μm), where YIG-based materials are attractive for nonreciprocal photonic devices such as optical isolators, optical circulators, and integrated magneto-optical components.

The magnetic results confirm that the extracted crystals exhibit the intrinsic ferrimagnetic behavior of $Y_3Fe_5O_{12}$, with properties suitable for applications in microwave devices, magnetic functional materials, and future magneto-optical photonic systems.

4.7 Conclusion – YIG System

Yttrium iron garnet ($Y_3Fe_5O_{12}$) single crystals were obtained in PbO-based, BaO-based, and Pb–Ba mixed glass-ceramics through controlled cooling, with crystal sizes in the range of 5–50 μm. Structural analyses show that the BaO-based and PB-YIG5% systems favor the formation of well-defined cubic YIG with minimal secondary phases, while PbO-based compositions contain additional crystalline phases, consistent with the XRD and Raman results.

Microscopy and SEM–EDS confirm that the crystals are uniformly distributed within the glass matrix and enriched in Y, Fe, and O, in agreement with the YIG composition. After extraction, the crystals show a well-defined cubic morphology, indicating good crystal development during the heat treatment. Magnetic measurements support these observations. The hysteresis loops are narrow and nearly closed, with low coercive fields and rapid saturation, which is typical of soft ferrimagnetic materials. The magnetization increases at low temperature (2 K) compared to 300 K, while the loop shape remains essentially unchanged, indicating stable magnetic ordering.

Among the compositions, Ba-YIG samples show higher saturation magnetization, while the Pb–Ba system exhibits similar behavior with slightly lower values. In contrast, Pb-based samples show lower magnetization and a less defined approach to saturation, consistent with the presence of secondary phases and a less developed magnetic phase.
The ZFC and FC measurements show no blocking peak and a gradual convergence of both curves with increasing temperature. This behavior is typical of ferrimagnetic systems with stable magnetic domains and confirms that the crystals are in the micrometer size range, with no evidence of superparamagnetic effects.

Overall, the results show that controlled crystallization in glass-ceramics can produce micrometer-sized YIG crystals with consistent structural and magnetic properties. The BaO-based and mixed systems provide more suitable conditions for obtaining well-crystallized and magnetically stronger YIG phases than the PbO-based compositions.

CHAPTER 5 – GENERAL CONCLUSIONS

This work investigated a glass-ceramic route for growing garnet single crystals directly within a glass matrix. The study focused on both terbium gallium garnet (TGG) and yttrium iron garnet (YIG), using heavy metal oxide glass systems based on PbO and BaO.

The results show that the supersaturated glass-melt method can be used to form micrometer-sized single crystals inside glass-ceramics. This approach avoids some of the limitations of conventional crystal growth methods, particularly in terms of processing complexity and scalability.

TGG was first used to establish and validate the method. The formation of well-defined cubic crystals with good optical quality confirmed that controlled crystallization in these systems is achievable. The substitution of PbO with BaO did not degrade the structural or magnetic properties of the material, indicating that BaO-based glasses can serve as a viable alternative.

Thermal analysis showed that increasing BaO content leads to a more rigid glass network and higher glass transition temperatures. These changes influence crystallization behavior and improve control over crystal formation. However, variations in optical transparency indicate that scattering from crystals and residual glass phases still needs to be reduced.

The approach was then extended to YIG, which presents stricter compositional and phase stability requirements. The results confirm that YIG single crystals can also be formed within glass-ceramics. Structural and spectroscopic analyses verified the formation of the garnet phase, while magnetic measurements confirmed ferrimagnetic behavior.

A clear difference between the two systems was observed. BaO-based compositions produced YIG with higher phase purity and fewer secondary phases compared to PbO-based systems. This suggests that BaO provides a more stable environment for crystallization in this case.

Overall, the study shows that glass-ceramic processing can be used to produce functional garnet crystals with controlled microstructure. The results also indicate that BaO-based systems can replace PbO while maintaining performance, which is relevant from both environmental and materials design perspectives.

6. Summary of Major Findings

The main findings of this work are:

- Garnet single crystals (TGG and YIG) can be grown directly inside glass-ceramics using a supersaturated glass-melt process
- TGG was successfully used to validate the synthesis approach and confirm controlled crystal formation
- BaO can replace PbO without loss of structural or magnetic performance
- BaO-based glasses show higher glass transition temperatures and improved network stability
- YIG single crystals were successfully formed in glass-ceramics
- BaO-based systems produced YIG with higher phase purity and fewer secondary phases than PbO-based systems
- Crystal formation is strongly influenced by glass composition and thermal treatment conditions

CHAPTER 7 – PERSPECTIVES AND FUTURE WORK

The results obtained in this work suggest several directions for future research. These are based on the outcomes achieved with TGG and YIG, as well as the requirements for moving toward practical applications.

One important next step is the fabrication of optical fibers using the developed glass-ceramic compositions. The current results show that both TGG and YIG crystals can be formed within the glass matrix with controlled size and distribution. This provides a basis for producing multi-mode optical fibers containing active magneto-optical phases. Such fibers could combine light guiding and magnetic functionality in a single material. The main challenge will be maintaining optical transparency during fiber drawing while preserving the crystalline phases and minimizing scattering.

Another direction is the evaluation of magneto-optical performance at the telecommunications wavelength of 1.55 μm. YIG is known for its transparency in the near-infrared region and its use in magneto-optical devices such as Faraday rotators. However, detailed measurements of Faraday rotation and optical losses in the synthesized glass-ceramics are still required. These measurements will allow comparison with existing materials and help assess their suitability for photonic applications.

Improving the magneto-optical response is also of interest. One approach is the introduction of dopants such as bismuth or cerium into the YIG structure. Bismuth substitution is known to enhance magneto-optical effects, particularly Faraday rotation, while cerium doping can modify the electronic structure and increase magneto-optical activity. Future work will focus on synthesizing Bi-substituted YIG (Bi:YIG) and Ce-substituted YIG (Ce:YIG) within glass-ceramic systems and evaluating their optical and magnetic properties.

To better understand these effects, advanced characterization techniques will be required. In particular, X-ray absorption spectroscopy (XAFS/XANES) at synchrotron facilities such as the LNLS XAFS beamline (Campinas) can provide information on local structure, oxidation states, and site occupancy. This will help clarify how dopants are incorporated into the garnet lattice and how they influence magneto-optical behavior.

Another area of interest is the use of YIG-based materials for sensing applications. YIG exhibits strong interaction between magnetic fields and light, which makes it suitable for optical sensing. Previous studies have shown its use in fiber-based magnetic field sensors.

Based on this, future work can explore YIG-containing glass-ceramics for sensing applications, including potential use in biosensing, where changes in the environment could be detected through variations in optical or magneto-optical signals.

Further optimization of glass composition and heat treatment conditions will also be necessary. Control of crystal size, distribution, and volume fraction remains critical for improving optical transparency and reducing scattering losses. This is particularly important for fiber fabrication and device integration.

Overall, the next stage of this work will focus on moving from material development toward application-oriented studies. The combination of fiber fabrication, magneto-optical characterization, compositional modification, advanced structural analysis, and sensing applications provides a clear direction for future research.

REFERENCES

[1] X. Zhao *et al.*, “High Verdet Constant Glass for Magnetic Field Sensors High Verdet Constant Glass for Magnetic Field Sensor,” *ACS Appl. Mater. Interfaces*, vol. 2022, no. 51, doi: 10.1021/ac.

[2] J. R. Orives *et al.*, “Micrometric patterning of a borogermanate glass containing terbium by thermal poling to manage luminescence and second order optical properties,” *JPhys Materials*, vol. 7, no. 3, Jul. 2024, doi: 10.1088/2515-7639/ad4ba0.

[3] N. Askarzadeh and H. Shokrollahi, “Spintronic Innovations with Yttrium Iron Garnet,” Dec. 01, 2025, *Springer*. doi: 10.1007/s11664-025-12411-7.

[4] M. Schabikowski *et al.*, “Yttrium iron garnet single-crystal particles—a simple and effective synthesis,” *Nano Express*, vol. 5, no. 3, Sep. 2024, doi: 10.1088/2632-959X/ad7bd6.

[5] K. L. Da Silva *et al.*, “Mechanosynthesized $BiFeO_3$ nanoparticles with highly reactive surface and enhanced magnetization,” *Journal of Physical Chemistry C*, vol. 115, no. 15, pp. 7209–7217, Apr. 2011, doi: 10.1021/jp110128t.

[6] L. Liu *et al.*, “A Gas Sensor With Fe_2O_3 Nanospheres Based on Trimethylamine Detection for the Rapid Assessment of Spoilage Degree in Fish,” *Front. Bioeng. Biotechnol.*, vol. 8, Sep. 2020, doi: 10.3389/fbioe.2020.567584.

[7] H. A. M. A. Azmy, N. A. Razuki, A. W. Aziz, N. S. A. Satar, and N. H. M. Kaus, “Visible light photocatalytic activity of $BiFeO_3$ nanoparticles for degradation of methylene blue,” *Journal of Physical Science*, vol. 28, no. 2, pp. 85–103, 2017, doi: 10.21315/jps2017.28.2.6.

[8] Akhtar, M. N., Sulong, A. B., Khan, M. A., Ahmad, M., Murtaza, G., Raza, M. R., ... & Kashif, M. (2016). Structural and magnetic properties of yttrium iron garnet (YIG) and yttrium aluminum iron garnet (YAIG) nanoferrites prepared by microemulsion method. Journal of Magnetism and Magnetic Materials, 401, 425-431.

https://doi.org/10.1016/j.jmmm.2015.10.060

[9] S. Kemethmüller, A. Roosen, F. Goetz-Neunhoeffer, and J. Neubauer, “Quantitative analysis of crystalline and amorphous phases in glass-ceramic composites like LTCC by the rietveld method,” *Journal of the American Ceramic Society*, vol. 89, no. 8, pp. 2632–2637, Aug. 2006, doi: 10.1111/j.1551-2916.2006.01113.x.

[10] A. E. Souza *et al.*, “Heavy metal oxide glass-ceramics containing luminescent gallium-garnets single crystals for photonic applications,” *J. Alloys Compd.*, vol. 864, May 2021, doi: 10.1016/j.jallcom.2021.158804.

[11] A. Chakrabarti and A. R. Molla, “Synthesis of Eu_2O_3 doped BaO-TiO_2-GeO_2 based glass-ceramics: Crystallization kinetics, optical and electrical properties,” *J. Non. Cryst. Solids*, vol. 505, pp. 354–366, Feb. 2019, doi: 10.1016/j.jnoncrysol.2018.11.002.

[12] H. He *et al.*, “Microstructure and properties of YIG/YIG magnetic homogenization joint fabricated by a novel Bi_2O_3–B_2O_3–NiO–Fe_2O_3 magnetic glass,” *Ceram. Int.*, vol. 50, no. 21, pp. 41673–41684, Nov. 2024, doi: 10.1016/j.ceramint.2024.08.018.

[13] T. Ishibashi, T. Kosaka, M. Naganuma, and T. Nomura, “Magneto-optical properties of Bi-substituted yttrium iron garnet films by metal-organic decomposition method,” in *Journal of Physics: Conference Series*, Institute of Physics Publishing, 2010. doi: 10.1088/1742-6596/200/11/112002.

[14] H. Shen *et al.*, “Recent advances of rare earth iron garnet magneto-optical single crystals,” *J. Cryst. Growth*, vol. 631, Apr. 2024, doi: 10.1016/j.jcrysgro.2024.127626.

[15] Q. Chen *et al.*, “A new strategy to fabricate YIG ferrite joint with novel magnetic Bi_2O_3-CoO-Fe_2O_3-B_2O_3 glass,” *Mater. Des.*, vol. 215, Mar. 2022, doi: 10.1016/j.matdes.2022.110521.

[16] W. Zhou *et al.*, “Synthesis and characterization of novel yellow-green Al-doped Y3Fe5O12 nano-pigments with high NIR reflectance,” *J. Alloys Compd.*, vol. 896, Mar. 2022, doi: 10.1016/j.jallcom.2021.162883.

[17] L. V. Albino *et al.*, “Innovative synthesis of Tm^{3+}/Er^{3+}-doped Yb-YGG single crystals for upconversion-based white light emission,” *Ceram. Int.*, vol. 51, no. 12, pp. 16700–16709, May 2025, doi: 10.1016/j.ceramint.2024.11.480.

[18] J.-J. Song, P. B. Klein, R. L. Wadsack, M. Selders, S. Mroczkowski, and R. K. Chang, “Raman-active phonons in aluminum, gallium, and iron garnets*.”

[19] K. Praveena, K. Sadhana, S. Srinath, and S. R. Murthy, “Structural and magnetic properties of nanocrystalline $Y_3Fe_5O_{12}$ using co-precipitation method,” in *AIP Conference Proceedings*, 2012, pp. 291–292. doi: 10.1063/1.4709994.

[20] S. Hosseinzadeh *et al.*, “High saturation magnetization, low coercivity and fine YIG nanoparticles prepared by modifying co-precipitation method,” *J. Magn. Magn. Mater.*, vol. 476, pp. 355–360, Apr. 2019, doi: 10.1016/j.jmmm.2018.12.090.

[21] M. Huang and Z. C. Xu, “Wavelength and temperature characteristics of BiYbIG film/YIG crystal composite structure for magneto-optical applications,” *Appl. Phys. A Mater. Sci. Process.*, vol. 81, no. 1, pp. 193–196, Jun. 2005, doi: 10.1007/s00339-004-2553-x.

[22] B. Mali, S. Das, and S. Elizabeth, “Magnetic Characterization of Zone-Refined Rare-Earth Orthoferrite Crystals Grown by the Optical Floating Zone Method,” *Cryst. Growth Des.*, vol. 24, no. 3, pp. 1003–1009, Feb. 2024, doi: 10.1021/acs.cgd.3c00967.

[23] Y. Cho, Y. W. Nahm, C. Decorse, and S. Cho, “Two-Step Floating Zone Method for Single-Crystal Growth of Er-Doped $Y_3Fe_5O_{12}$,” *ACS Omega*, vol. 10, no. 27, pp. 29421–29427, Jul. 2025, doi: 10.1021/acsomega.5c02558.

[24] D. Vojna, O. Slezák, R. Yasuhara, H. Furuse, A. Lucianetti, and T. Mocek, “Faraday rotation of Dy_2O_3, cef3 and $Y_3Fe_5O_{12}$ at the mid-infrared wavelengths,” *Materials*, vol. 13, no. 23, pp. 1–17, Dec. 2020, doi: 10.3390/ma13235324.

[25] Y. Kim, D. J. Bang, Y. Kim, and K. H. Kim, “Magneto-optical properties of spin-coated bismuth-substituted yttrium iron garnet films on silicon substrates at 1550-nm wavelength,” *AIP Adv.*, vol. 10, no. 2, Feb. 2020, doi: 10.1063/1.5137769.

[26] A. Ikesue, Y. L. Aung, R. Yasuhara, and Y. Iwamoto, “Giant Faraday rotation in heavily ce-doped YIG bulk ceramics,” *J. Eur. Ceram. Soc.*, vol. 40, no. 15, pp. 6073–6078, Dec. 2020, doi: 10.1016/j.jeurceramsoc.2020.05.062.

[27] J. Jiang *et al.*, “Perpendicular magnetic anisotropy and magneto-optical properties of Bi,Mn:YIG epitaxial films,” *CrystEngComm*, vol. 26, no. 1, pp. 32–39, Nov. 2023, doi: 10.1039/d3ce00760j.

28 D. Vojna, O. Slezák, R. Yasuhara, H. Furuse, A. Lucianetti, and T. Mocek, “Faraday Rotation of Dy_2O_3, CeF_3 and $Y_3Fe_5O_{12}$ at the Mid-Infrared Wavelengths,” Materials, vol. 13, no. 23, pp. 5324, Nov. 2020, doi: 10.3390/ma13235324.

29 Siao, Y. J., Qi, X., Lin, C. R., & Huang, J. C. A. (2011). Dielectric relaxation and magnetic behavior of bismuth-substituted yttrium iron garnet. *Journal of Applied Physics*, *109*(7). https://doi.org/10.1063/1.3559488

30 L. Weller, K. S. Kleinbach, M. A. Zentile, S. Knappe, I. G. Hughes, and C. S. Adams, “Optical Isolator Using an Atomic Vapor in the Hyperfine Paschen–Back Regime,” Opt. Lett., vol. 37, no. 16, pp. 3405–3407, Aug. 2012, doi: 10.1364/OL.37.003405.

31 Hosseinzadeh, S., Behboudnia, M., Jamilpanah, L., Sheikhi, M. H., Mohajerani, E., Tian, K., ... & Mohseni, S. M. (2019). High saturation magnetization, low coercivity and fine YIG nanoparticles prepared by modifying co-precipitation method. *Journal of Magnetism and Magnetic Materials*, *476*, 355-360. https://doi.org/10.1016/j.jmmm.2018.12.090

32 Y. Kim, D. J. Bang, Y. Kim, and K. H. Kim, “Magneto-Optical Properties of Spin-Coated Bismuth-Substituted Yttrium Iron Garnet Films on Silicon Substrates at 1550-nm Wavelength,” AIP Adv., vol. 10, no. 2, pp. 025306, Feb. 2020, doi: 10.1063/1.5137769.

33 A. Ikesue, Y. L. Aung, R. Yasuhara, and Y. Iwamoto, “Giant Faraday Rotation in Heavily Ce-Doped YIG Bulk Ceramics,” J. Eur. Ceram. Soc., vol. 40, no. 15, pp. 6073–6078, Dec. 2020, doi: 10.1016/j.jeurceramsoc.2020.05.062.

34 Xu, H., & Yang, H. (2008). Magnetic properties of YIG doped with cerium and gadolinium ions. *Journal of Materials Science: Materials in Electronics*, *19*(7), 589-593. DOI 10.1007/s10854-007-9394-2

35 Saini, J., Sharma, M., & Kuanr, B. K. (2021). Role of Ce concentration on the structural and magnetic properties of functional magnetic oxide particles. *Nanoscale Advances*, *3*(21), 6074-6087. DOI: 10.1039/D1NA00227A

36 Y. Kim, D. J. Bang, Y. Kim, J. Jung, N. Hur, C.-Y. You, and K. H. Kim, “Magneto-Optic Property Measurement of Bismuth-Substituted Yttrium Iron Garnet Films Prepared by Metal-Organic-Decomposition Method at the 1310-nm and 1550-nm Wavelengths,” J. Magn. Magn. Mater., vol. 492, pp. 165673, Dec. 2019, doi: 10.1016/j.jmmm.2019.165673.

37 Xu, H., Yang, H., Xu, W., & Yu, L. (2008). Magnetic properties of Bi-doped $Y_3Fe_5O_{12}$ nanoparticles. *Current Applied Physics*, *8*(1), 1-5. https://doi.org/10.1016/j.cap.2007.04.002

APPENDIX

Appendix I – Additional Results and Supporting Analysis

This appendix presents supplementary results obtained during the course of this study. The work involved the investigation of multiple glass systems and compositional designs, which led to the successful synthesis of garnet materials, including TGG and YIG single crystals in Pb-free systems. Due to the exploratory nature of the study and the range of compositions examined, several additional analyses were carried out that are not included in the main discussion.

These results include further SEM images, optical microscopy observations, and Raman spectra, which support the structural and microstructural interpretation presented in the main chapters.

In addition, bulk YIG samples were synthesized using a containerless processing technique (levitation melting) to enable magneto-optical measurements. The YIG crystals obtained from the glass-ceramic route were typically in the micrometer size range and could not be directly used for such measurements due to limitations in sample handling and alignment. To address this, stoichiometric amounts of Y_2O_3 and Fe_2O_3 corresponding to the YIG composition were used to produce bulk samples via levitation processing. This approach allowed the preparation of larger, homogeneous YIG materials suitable for magneto-optical characterization.

The results presented in this appendix provide additional context and support for the conclusions drawn in this work.

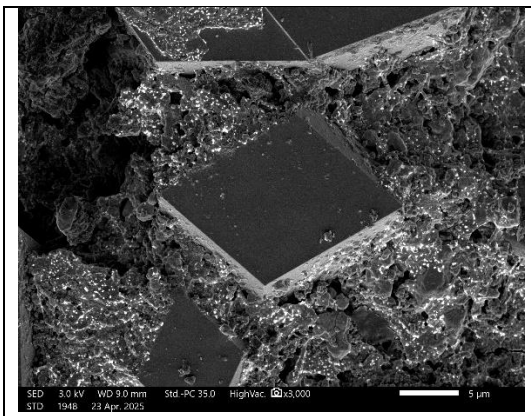

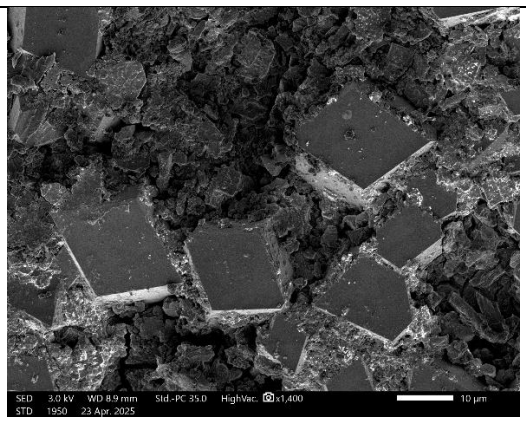

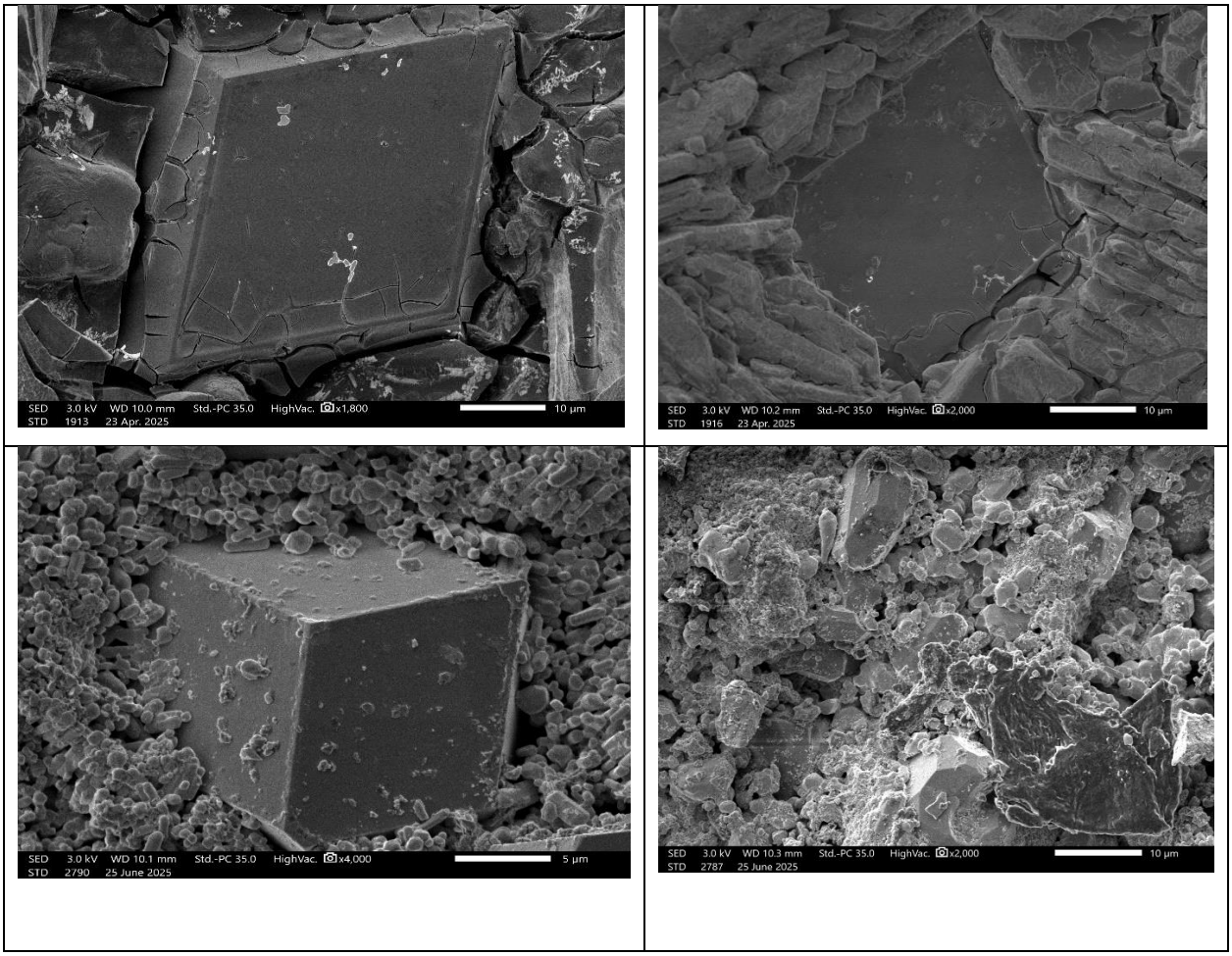

Figure A-1. SEM images of a) Ba-YIG b) Pb-Ba-YIG5% c) Pb-YIG2 d) Glassy phase

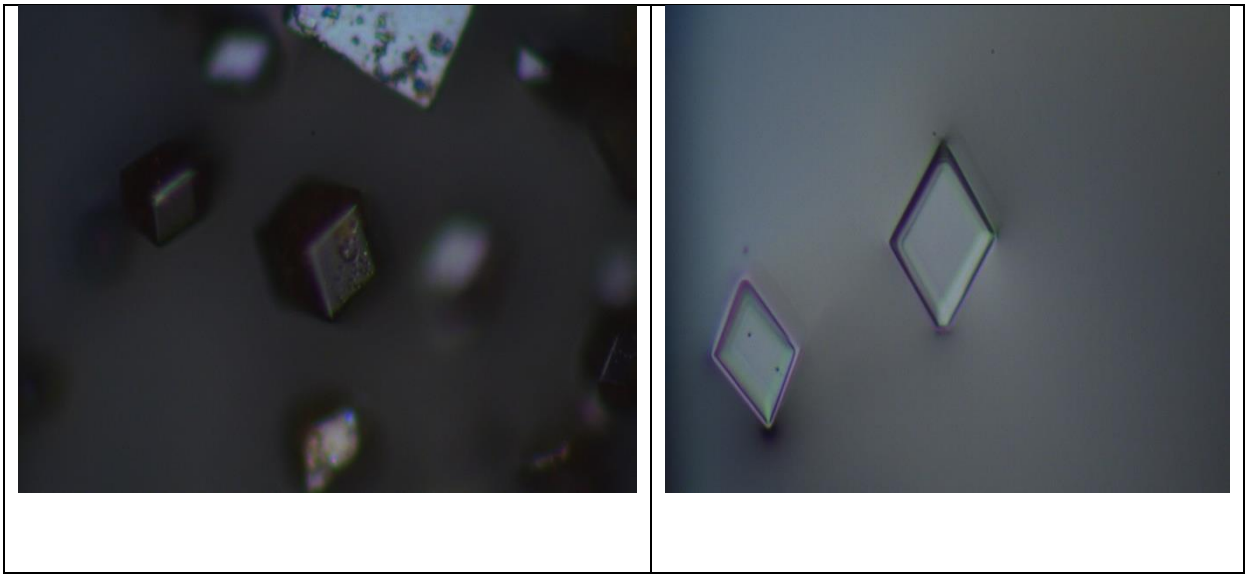

Figure A-2. Raman images of YIG crystals a) Outside glass matrix b) Inside glass matrix

Development of the micrometer YIG Single-crystal – The Journey

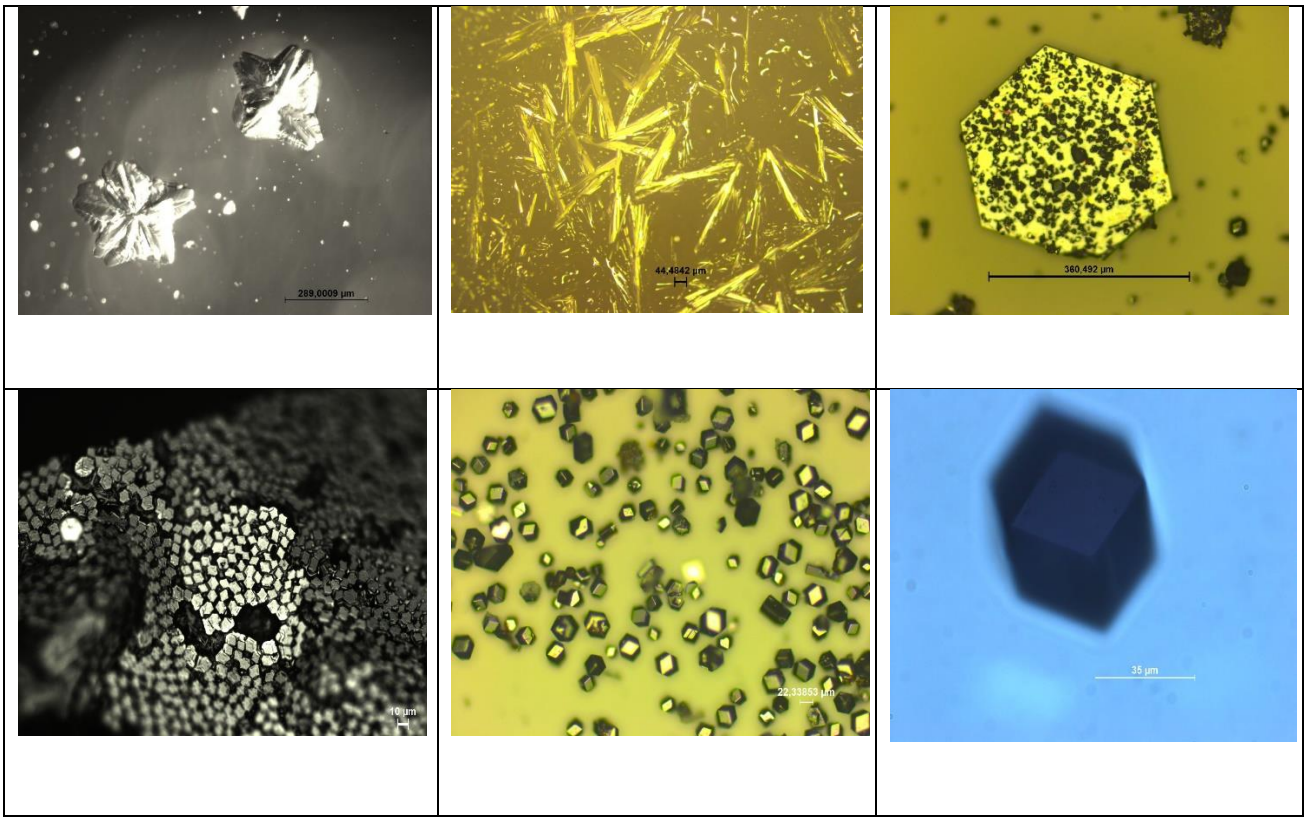

Figure A-3. Optical microscopy images of YIG crystals

Figure A-4. Bulk YIG samples were synthesized using a containerless processing technique (levitation melting) for MO measurements.

Supplementary Raman Spectroscopy Data

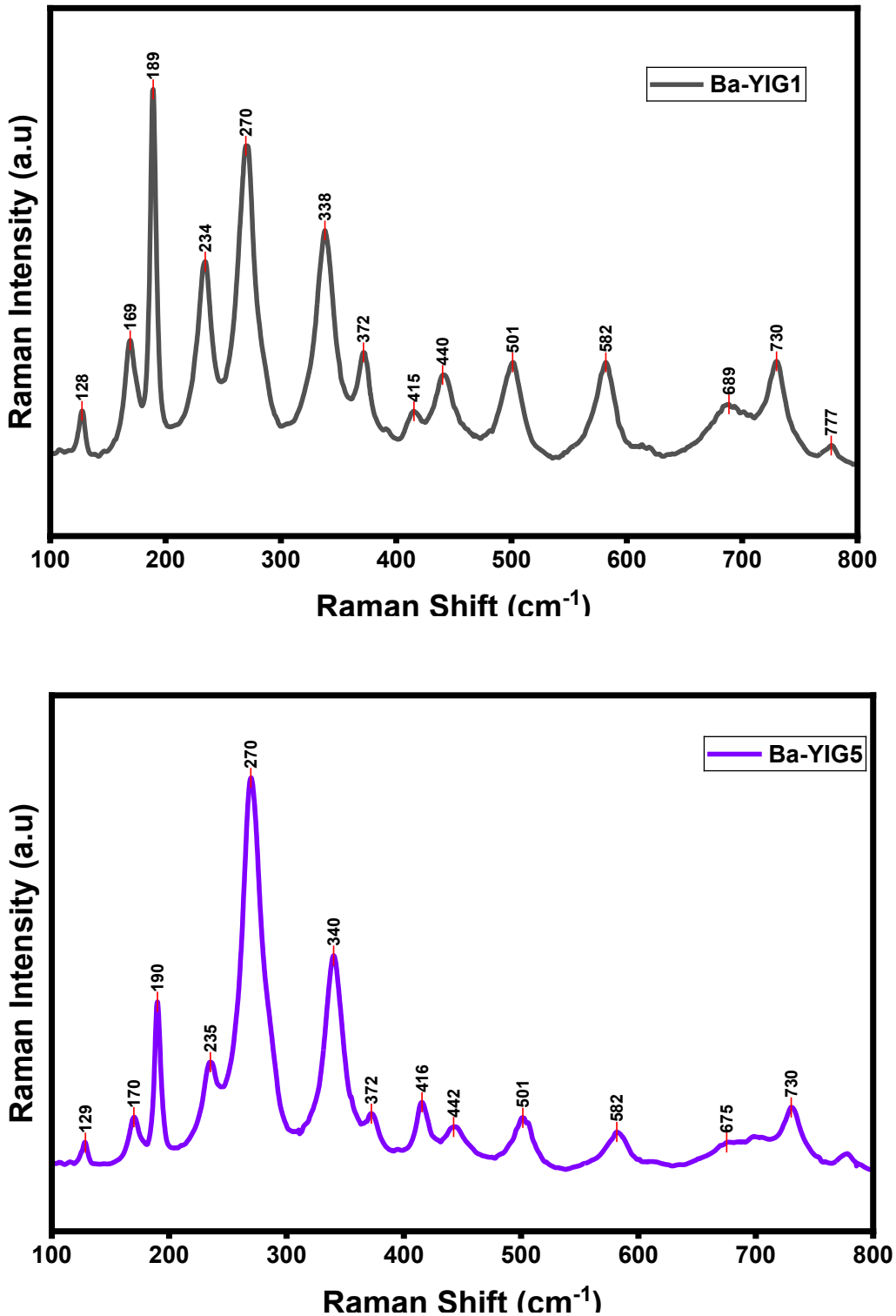

Figure A5. The assigned Raman-active vibrational modes of YIG (a) Raman spectrum of Ba-YIG1, and **(b)** Raman spectrum of Ba-YIG5.

Appendix II – Bernhard Gross Award

Part of this work was presented at the SBPMat Congress 2025 under the title “Synthesis and Characterization of Yttrium Iron Garnet Crystals in PbO and BaO Based Glass-Ceramics: Effects of Y_2O_3 and Fe_2O_3 Doping on Magneto-Optical Properties”, where it received the Bernhard Gross Student Award 2025 (Symposium F, Oral Presentation), as presented in fig A6.

Figure A6. Bernhard Gross Certificate Awarded at B-MRS Meeting 2025

Appendix III – Periodic Table of Elements